UNIVERSITAT POLITÈCNICA DE CATALUNYA
BARCELONATECH
Department of Physics

Doctoral program in Computational and Applied Physics

Development and interactions of surfzone morphological patterns

PhD thesis presented by

Rinse Leendert de Swart

to apply for the degree of doctor
at the Universitat Politècnica de Catalunya

Directors:

Dr. Francesca Ribas Prats

Dr. Daniel Calvete Manrique

Barcelona, July 2022

Directors:
Dr. Francesca Ribas Prats
Dr. Daniel Calvete Manrique

Committee members:
Prof. dr. Albert Falqués Serra
Universitat Politècnica de Catalunya, Spain

Dr. Àngels Fernández Mora
Coastal Ocean Observing and Forecasting System of the Balearic Islands (SOCIB), Spain

Dr. Bruno Castelle
Le Centre National de la Recherche Scientifique (CNRS), Université de Bordeaux, France

Dr. Ruth Durán Gallego
Institut de Ciències del Mar (ICM-CSIC), Spain

Prof. dr. Giovanni Coco
University of Auckland, New Zealand

Typeset using XeLaTeX

Chapter covers: Google Earth (Chapters 1, 3-5) and Rinse L. de Swart (other chapters)

This research was funded by the Spanish government through the research projects CTM2015-66225-C2-1-P and RTI2018-093941-B-C33 (MINECO/ FEDER).

"It is a capital mistake to theorize before one has data."
Arthur Conan Doyle

Contents

Summary

A variety of morphodynamic patterns are typically present in the nearshore zone of sandy beaches that develop due to the interactions between waves, currents and the morphology. The most common are one or several nearshore sandbars that vary in configuration from shore-parallel to crescentic, the latter consisting of alongshore-rhythmic (i.e., undulating) bars (also called rip-channel systems). Crescentic bars are often coupled to similar undulations in the shoreline called megacusps. Understanding the evolution of nearshore sandbars and their coupling to the shoreline is important as they significantly affect the nearshore morphology and hydrodynamics. Alongshore sandbar variability has been studied extensively, but mostly at beaches with substantial tidal range and medium-high energetic waves. Furthermore, the dynamics of megacusps and their coupling with crescentic bars are much less understood.

This thesis uses nearly 8 years of hourly time-exposure video images to study the development and interactions of crescentic bars and megacusps at the open, low-energetic, tideless beach of Castelldefels (northwestern Mediterranean Sea, Spain). This requires accurate directional wave conditions at shallow water which can be obtained in various ways. Here, the accuracy of two available large-scale wave models and propagating measured wave conditions (integrated wave parameters and 2D frequency-direction spectra) using wave ray theory or the SWAN wave model was assessed. Comparing the results of the different methods to a short-term dataset of in-situ measurements showed that propagating measured 2D frequency-direction spectra using SWAN yielded the most accurate predictions for all wave parameters. The other methods resulted in increased errors in wave direction, particularly for shore-oblique and bimodal wave climates due to underestimation of refraction.

The video images together with the hourly wave conditions at shallow water in front of Castelldefels beach (obtained with the optimal propagation method) were subsequently used to investigate the dynamics of crescentic bars and megacusps as well as the corresponding coupling. Crescentic bars were present during 48% of the study period, but only when the bar-shoreline distance exceeded 10 m. They showed a wide range in wavelengths (100–700 m), alongshore migration speeds (0–50 m/day) and cross-shore amplitudes (5–20 m). Low-medium energetic waves with limited obliquity ($\theta \lesssim 20^\circ$ at 10-m depth) dominated during crescentic bar formation, whereas medium-high energetic waves with strong obliquity ($\theta \gtrsim 15^\circ$) prevailed during their straightening. These observed angle ranges contradict the results of existing models. Megacusps were present during 24% of the study period and crescentic bars were present during 91% of all days with megacusps, whilst megacusps only occurred during 50% of all days with crescentic bars. Megacusp and crescentic bar wavelengths were similar (100–700 m), but the cross-shore amplitudes (3–8 m) and alongshore migration speeds (0–15 m/day) of the former were significantly smaller. Megacusp dynamics were not strongly linked to wave conditions and they mostly developed a few days after the formation of a crescentic bar, confirming that the presence of the latter induces mega-

cusp formation. Significant sandbar-shoreline coupling was observed during 74% of the time when megacusps and crescentic bars occurred simultaneously. The type of coupling pattern was variable and depended on the wave height and angle, as they probably determine the flow pattern over the inner crescentic bar (single or double rip cell circulations versus meandering currents). Overall, this thesis shows that crescentic bar dynamics strongly depend on the wave direction and initial bathymetric configuration, highlights the strong dependence of megacusp development on crescentic bar presence and provides some ideas regarding the underlying coupling mechanisms.

Resumen

En la zona sumergida de las playas arenosas aparecen típicamente patrones morfológicos resultantes de las interacciones entre el oleaje, las corrientes y el fondo marino. Los más frecuentes son barras de arena, paralelas a la costa o crescénticas (con ondulaciones longitudinales). Las barras crescénticas a menudo se acoplan a patrones similares en la orilla conocidos como megacúspides. La evolución de estos patrones afecta significativamente la morfología y la hidrodinámica próxima de la orilla. Las barras crescénticas se han estudiado ampliamente, principalmente en playas con mareas importantes y oleaje de energía media-alta. Sin embargo, existe un gran desconocimiento sobre la dinámica de las megacúspides y su acoplamiento con las barras crescénticas.

Esta tesis utiliza casi 8 años de imágenes horarias de video para estudiar el desarrollo y las interacciones de barras crescénticas y megacúspides en Castelldefels (noroeste del mar Mediterráneo, España), una playa abierta de baja energía y sin mareas. El estudio requiere de datos precisos de oleaje direccional en aguas someras que se pueden obtener con varias metodológías. Aquí se evaluó la precisión de dos modelos de oleaje a gran escala y la propagación de oleaje medido (parámetros de oleaje y espectros 2D en dirección y frecuencia) utilizando la teoría de rayos o el modelo SWAN. La comparación de los diferentes métodos con un conjunto de datos a corto plazo de medidas in situ mostró que la propagación de espectros 2D con SWAN produce las predicciones más precisas. Los otros métodos dieron como resultado errores mayores en la dirección, debido a la subestimación de la refracción durante climas de oleaje bimodal y oblicuo a la costa.

Las imágenes de vídeo junto con los datos de oleaje en aguas someras frente a la playa de Castelldefels (obtenidos con el método óptimo) se utilizaron para investigar la dinámica de barras crescénticas y megacúspides, así como el acoplamiento correspondiente. Las barras crescénticas estuvieron presentes un 48% del período de estudio, pero solo cuando la distancia entre la orilla y la barra excedía los 10 m. Mostraron una gran variabilidad en longitudes de onda (100–700 m), velocidades de migración longitudinal (0–50 m/día) y amplitudes transversales (5–20 m). Durante la formación de las barras crescénticas, dominó el oleaje de energía media-baja con oblicuidad limitada ($\theta \lesssim 20^\circ$ a 10 m de profundidad), mientras que el oleaje de energía media-alta con oblicuidad fuerte ($\theta \gtrsim 15^\circ$) prevaleció durante su desaparición. Estos rangos de ángulos observados contradicen los resultados de los modelos existentes. Las megacúspides ocurrieron durante un 24% del período de estudio y las barras crescénticas estaban presentes durante un 91% de los días con megacúspides, mientras que las megacúspides solo se observaron durante un 50% de los días con barras crescénticas. Las longitudes de onda de las megacúspides y las barras crescénticas fueron similares (100–700 m), pero las amplitudes (3–8 m) y las velocidades de migración (0–15 m/día) de las primeras fueron más pequeñas. La dinámica de las megacúspides no estuvo fuertemente relacionada con el oleaje y se desarrollaron principalmente unos días después de la formación de una barra crescéntica, confirmando que su presencia genera las megacúspides. Se observó

un acoplamiento significativo entre la orilla y la barra durante un 74% del tiempo en que ocurrieron simultáneamente megacúspides y barras crescénticas. El tipo de acoplamiento fue variable y dependió de la altura y el ángulo del oleaje, ya que probablemente determinan el patrón de corriente sobre la barra crescéntica. En general, esta tesis muestra que la dinámica de las barras crescénticas depende mucho de la dirección de oleaje y la configuración inicial de la batimetría, destaca la fuerte relación entre el desarrollo de las megacúspides y la presencia de una barra crescéntica y proporciona ideas sobre los mecanismos físicos de acoplamiento.

Resum

A la zona submergida de les platges de sorra apareixen típicament una varietat de patrons morfològics que resulten de les interaccions entre les onades, els corrents i el fons marí. Els més comuns són barres de sorra que poden ser paral·leles a la costa o crescèntiques (amb ondulacions longitudinals). Les barres crescèntiques sovint s'acoblen a patrons similars a la riba (megacúspides). L'evolució d'aquests patrons afecta significativament la morfologia i la hidrodinàmica a prop de la costa. Les barres crescèntiques s'han estudiat àmpliament, però principalment a platges amb marees importants i onatge d'energia mitjana-alta. La dinàmica de les megacúspides i el seu acoblament amb les barres crescèntiques es coneixen molt menys.

Aquesta tesi utilitza gairebé 8 anys d'imatges horàries de vídeo per estudiar el desenvolupament i les interaccions de barres crescèntiques i megacúspides a Castelldefels (nord-oest del mar Mediterrani, Espanya), una platja oberta de baixa energia i sense marees. Això requereix dades precises d'onatge direccional en aigües poc profundes que es poden obtenir de diverses maneres. Aquí es va avaluar la precisió de dos models d'onatge a gran escala i la propagació d'onatge mesurat (paràmetres d'onatge i espectres 2D en direcció i freqüència) utilitzant la teoria de rajos o el model SWAN. La comparació dels diferents mètodes amb un conjunt de dades a curt termini de mesures in situ va mostrar que la propagació d'espectres 2D amb SWAN produeix les prediccions més precises. Els altres mètodes van donar com a resultat errors més grans en la direcció, a causa de la subestimació de la refracció durant climes d'onatge bimodal i oblic a la costa.

Les imatges de vídeo juntament amb les dades d'onatge en aigües poc profundes davant de la platja de Castelldefels (obtingudes amb el mètode òptim) es van utilitzar per investigar la dinàmica de barres crescèntiques i megacúspides, així com l'acoblament corresponent. Les barres crescèntiques van estar presents un 48% del període d'estudi, però només quan la distància entre la riba i la barra excedia els 10 m. Van mostrar una gran variabilitat en longituds d'ona (100–700 m), velocitats de migració longitudinal (0–50 m/dia) i amplituds transversals (5–20 m). Durant la formació de les barres crescèntiques, va dominar l'onatge d'energia mitjana-baixa amb obliqüitat limitada ($\theta \lesssim 20°$ a 10 m de profunditat), mentre que l'onatge d'energia mitjana-alta amb obliqüitat forta ($\theta \gtrsim 15°$) va prevaldre durant la desaparició. Aquests rangs d'angles observats contradiuen els resultats dels models existents. Les megacúspides van ocórrer durant un 24% del període d'estudi i les barres crescèntiques estaven presents durant un 91% dels dies amb megacúspides, mentre que les megacúspides només es van observar durant un 50% dels dies amb barres crescèntiques. Les longituds d'ona de les megacúspides i les barres crescèntiques eren semblants (100–700 m), però les amplituds (3–8 m) i les velocitats de migració (0–15 m/dia) de les primeres eren més petites. La dinàmica de les megacúspides no va estar fortament relacionada amb l'onatge i es van desenvolupar principalment uns dies després de la formació d'una barra crescèntica, confirmant que la seva presència genera les megacúspides. Es va observar un acoblament significatiu entre la riba i la barra durant un 74% del temps en què van ocórrer simultàniament megacúspi-

des i barres crescèntiques. El tipus d'acoblament era variable i depenia de l'alçada i l'angle de l'onatge, ja que probablement determinen el patró de corrent sobre la barra crescèntica. En general, aquesta tesi mostra que la dinàmica de les barres crescèntiques depèn molt de la direcció d'onatge i la configuració inicial de la batimetria, destaca la forta relació entre el desenvolupament de les megacúspides i la presència d'una barra crescèntica i proporciona idees sobre els mecanismes físics d'acoblament.

Samenvatting

De ondiepe (< 10 m) wateren van zandige kusten worden meestal gekenmerkt door een grote verscheidenheid aan morfologische patronen, welke ontstaan als gevolg van de interacties tussen golven, stromingen en de morfologie. Veelvoorkomende patronen zijn een of meerdere kustnabije zandbanken die qua configuratie variëren van parallel langs de kust tot crescentisch, waarbij de laatste gekenmerkt worden door een kustlangse ritmische (golvende) periodiciteit. Crescentische zandbanken zijn vaak morfologisch gekoppeld aan soortgelijke ritmische patronen in de kustlijn die megacusps worden genoemd. Het begrijpen van de evolutie van kustnabije zandbanken en hun koppeling met de kustlijn is belangrijk aangezien ze de morfologie en hydrodynamica in ondiep water aanzienlijk beïnvloeden. De kustlangse variabiliteit van zandbanken is in het verleden al uitgebreid bestudeerd, maar vooral op stranden met aanzienlijke getijden en gemiddeld tot hoog-energetische golven. Daarnaast zijn er nog veel open vragen omtrent de dynamica van megacusps en hun koppeling met crescentische zandbanken.

Dit proefschrift maakt gebruik van bijna 8 jaar aan uurlijkse videobeelden om de ontwikkeling en interacties van crescentische zandbanken en megacusps te bestuderen op het open, laag-energetische strand met verwaarloosbaar getij van Castelldefels (noordwestelijke Middellandse Zee, Spanje). Om dit te doen zijn nauwkeurige golfcondities op ondiep water noodzakelijk die op verschillende manieren kunnen worden verkregen. Voor Castelldefels werd de nauwkeurigheid bepaald van twee beschikbare grootschalige golfmodellen en het propageren van gemeten golfcondities (geïntegreerde golfparameters en 2D spectra in frequentie en richting) met behulp van golfstraaltheorie of het SWAN-golfmodel. Door de resultaten van de verschillende methoden te vergelijken met een korte-termijn dataset van metingen ter plaatse bleek dat het propageren van gemeten 2D spectra in richting en frequentie met behulp van SWAN de meest nauwkeurige voorspellingen opleverde voor alle golfparameters. De andere methodes resulteerden in grotere fouten in golfrichting, doordat refractie tijdens bimodale golfklimaten en schuin-invallende golven werd onderschat.

De videobeelden en de golfcondities per uur in ondiep water voor het strand van Castelldefels (verkregen met de optimale propagatiemethode) werden vervolgens gebruikt om de dynamica van crescentische zandbanken en megacusps en de gerelateerde morfologische koppeling te onderzoeken. Crescentische zandbanken kwamen vaak voor tijdens de studieperiode (48% van de tijd), maar alleen wanneer de gemiddelde kustlangse afstand tussen de zandbank en de kustlijn groter was dan 10 m. Ze vertoonden een grote variatie in golflengtes (100–700 m), kustlangse migratiesnelheden (0–50 m/dag) en kustdwarse amplitudes (5–20 m). Laag tot gemiddeld-energetische golven met een relatief kleine invalshoek ($\theta \lesssim 20°$ op 10 m diepte) domineerden tijdens de vorming van crescentische zandbanken, terwijl gemiddeld tot hoog-energetische golven met een grote invalshoek ($\theta \gtrsim 15°$) dominant waren bij het rechttrekken van crescentische zandbanken. Deze waargenomen reikwijdtes in golfhoek zijn in tegenspraak met de resultaten van bestaande morfologische modellen. Megacusps waren

aanwezig gedurende 24% van de studieperiode en crescentische zandbanken waren aanwezig gedurende 91% van alle dagen met megacusps, terwijl megacusps slechts gedurende 50% van alle dagen met crescentische zandbanken voorkwamen. De golflengtes van de megacusps en de crescentische zandbanken waren vergelijkbaar (100–700 m), maar de kustdwarse amplitudes (3–8 m) en de kustlangse migratiesnelheden (0–15 m/dag) van de megacusps waren aanzienlijk kleiner. De dynamica van de megacusps was niet sterk gerelateerd aan de golfcondities en ze ontstonden meestal een paar dagen na de vorming van een crescentische zandbank, wat aangeeft dat megacusps afhankelijk zijn van de aanwezigheid van een crescentische zandbank. Significante morfologische koppeling tussen zandbank en kustlijn was aanwezig gedurende 74% van de tijd waarin megacusps en crescentische zandbanken gelijktijdig voorkwamen. Het koppelingstype was variabel en hing af van de golfhoogte en golfhoek, aangezien deze vermoedelijk het stromingspatroon over de binnenste crescentische zandbank bepalen. Alles overziend toont dit proefschrift aan dat de dynamica van crescentische zandbanken sterk afhangt van de golfrichting en de initiële bathymetrische configuratie, benadrukt het dat de ontwikkeling van megacusps sterk afhangt van de aanwezigheid van een crescentische zandbank en geeft het enkele ideeën betreffende de onderliggende fysische mechanismen die van invloed kunnen zijn op het ontstaan van de verschillende koppelingstypes.

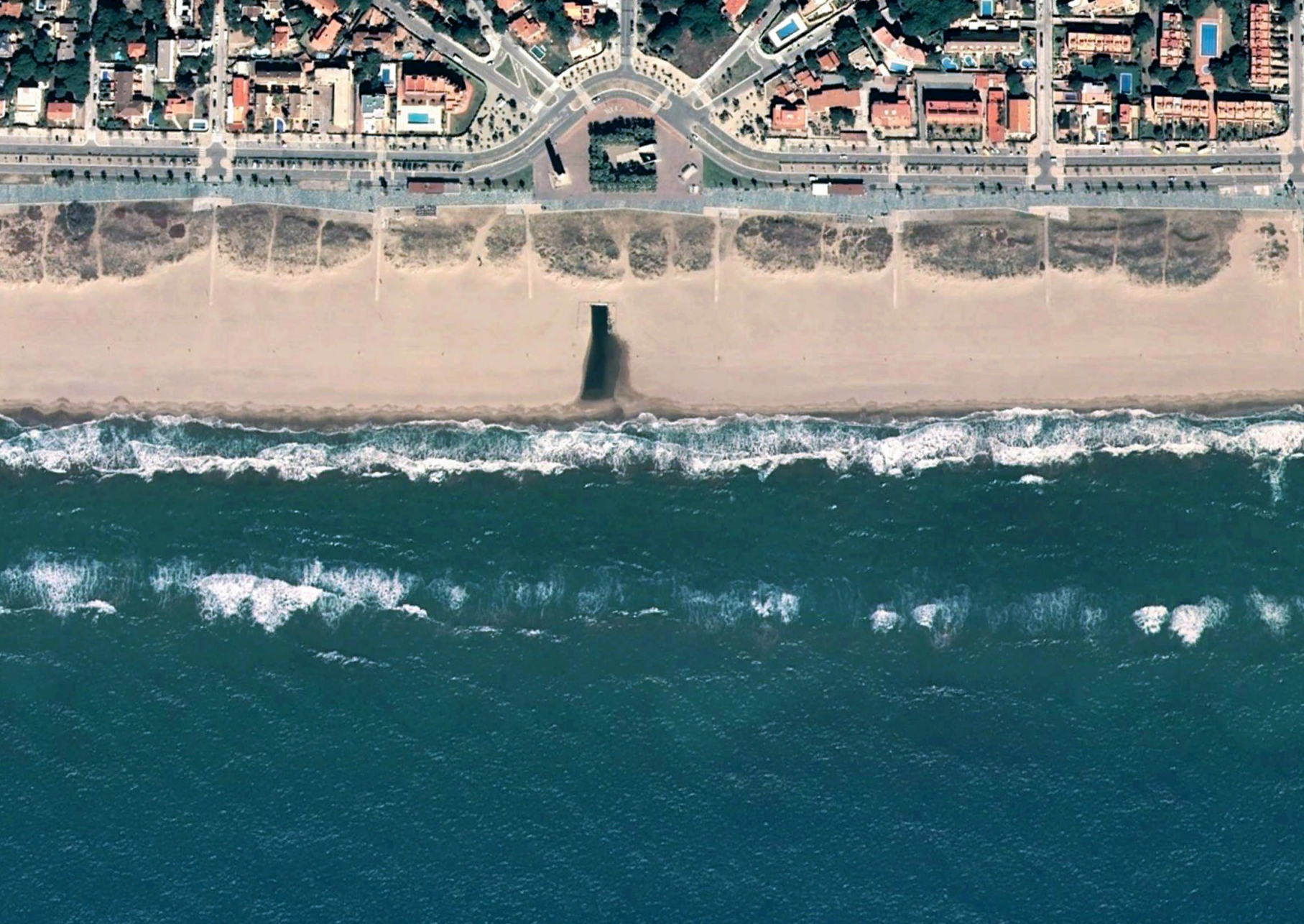

Chapter 1 | Introduction

1.1 The coastal system

Around 31% of the coastlines around the world are bordered by beaches composed of non-consolidated sediments like sand and gravel (Luijendijk et al., 2018). They are affected by various types of hydrodynamic forces that occur in the nearshore zone, such as waves, currents and sea level variations. Beaches form a first line of coastal protection as they dissipate a significant portion of incoming wave energy by moving sediment and adopting various morphological configurations in response to the prevailing wave conditions. Coastal morphology evolves as sediment is transported both by currents (often generated by waves) and the waves themselves (mostly due to wave asymmetry and skewness), with the current-driven transport typically being much larger than that by the waves alone. Generally, the water depth in the nearshore increases in the offshore direction and in the longshore direction it can be either constant (alongshore-uniform) or fluctuating (alongshore-variable). Waves breaking over alongshore-variable bathymetry generate strong cross-shore and longshore currents that dominate the sediment transport and thus the morphological evolution. Climate conditions directly affect the nearshore by modifying hydrodynamic forces (sea level, waves and currents), which leads to changes in the nearshore morphology. Moreover, the changing morphology modifies the hydrodynamics, which results in a complex feedback between the morphology and the hydrodynamic forces (Ribas et al., 2015, and references therein). As a result, sandy coasts are highly dynamic environments where many nonlinear processes interact at different spatial and temporal scales (e.g., sediment/waves/currents, waves/currents/bottom, etc.), which vary from seconds-centimetres for wave and sediment motion to years-kilometres for large scale morphological patterns (Blondeaux, 2001; Ribas et al., 2015).

Many beaches around the world are nowadays experiencing chronic erosion due to extreme events (storms) and human-induced (e.g., harbour dredging and river damming) shortages in sand supply (Vitousek et al., 2017). Unfortunately, accelerated sea level rise and potential increased storm activity as a result of climate change will imply that many coastal zones become even more prone to coastal flooding and erosion (Nicholls and Cazenave, 2010; Oppenheimer et al., 2019; Vousdoukas et al., 2020). This can lead to significant human and economic losses as many coastal areas are densely populated and hold high socio-economic, ecological and cultural values.

Although a lot of research has already been done on the coastal system, several challenges remain. For example, the sediment transport processes are still not yet fully understood and hard to predict (Amoudry and Souza, 2011). Also, there is no consensus yet on how sandy beaches will respond to climate change (Vousdoukas et al., 2020; Cooper et al., 2020). Apart from that, the continuously changing boundary conditions like bathymetry and shoreline add additional complexity. Moreover, human interventions (e.g., sand mining, harbour construction, dredging) result in additional interference with the complex dynamics of the

coastal system, meaning that such activities are risky without a good knowledge of the involved processes. As a result, human actions can be ineffective or excessively expensive, but also solve problems at one particular beach and simultaneously cause undesired side effects at neighbouring beaches. Thus, understanding the physical processes on sandy coasts in response to hydrodynamic forcings is not only a scientific challenge but also important from a societal and economical point of view.

1.2 Nearshore morphodynamic patterns

Shallow submerged sandbars are a common long-lasting morphological feature in the nearshore zone of sandy beaches (e.g., Wright and Short, 1984; Ruessink and Kroon, 1994; Aleman et al., 2017). They constitute a sediment buffer within the nearshore zone that moves onshore (offshore) during mild (stormy) wave conditions. As a result, sandbars play an important role in the overall behaviour of beaches, forming a first line of coastal protection by dissipating a significant portion of wave energy before it reaches the shore. Apart from shore-parallel sandbars, more complex morphodynamic patterns are often observed in the nearshore that are characterised by a striking alongshore periodicity. Examples are shoreline sand waves, crescentic bars (or rip channel systems), transverse bars, megacusps and beach cusps (Figure 1.1). Each of these patterns is characterised by its own distinct length and time scales, which range from metres and hours to kilometres and years. Understanding the dynamics of these patterns is important to advance our general knowledge about nearshore processes and sediment transport. Earlier studies in the past explained the development of these patterns using hydrodynamical templates (e.g., Bowen and Inman, 1971; Guza and Inman, 1975; Holman and Bowen, 1982), but nowadays the formation of these patterns is explained by the principle of self-organisation (Sonu, 1972; Hino, 1974; Coco and Murray, 2007), in which patterns develop as a result of the coupling between the hydrodynamics and the morphology (Falqués et al., 1996; Falqués et al., 2000; Coco and Murray, 2007; Ribas et al., 2015). A brief description of the different patterns and the current state of knowledge is given in the next paragraphs.

The different types of rhythmic patterns are characteristic of various regions in the nearshore zone. Shoreline sand waves are large-scale undulations in the shoreline with typical wavelengths of several kilometres (Figure 1.1a) that are affected by processes in the shoaling zone (the region where waves start to feel the bottom; Figure 1.2). They develop due to a feedback between the wave-driven longshore current, bathymetric variations in the surf and shoaling zones, and wave shoaling and refraction experienced by oblique waves (Van den Berg et al., 2012; Kaergaard and Fredsoe, 2013). Beach cusps are small-scale alongshore rhythmic features found in the swash zone (the region where waves runup the beach; Figure 1.2) that typically have spacings of 1–50 m (Figure 1.1f; Ribas et al., 2015). Nowadays, it is widely accepted that they develop as a result of self-organisation (Dodd et al., 2008). The focus of this thesis is on nearshore sandbars, common morphodynamic patterns that occur in the surf zone (the region where waves break; Figure 1.2). They are typically located from the shoreline up to several hundreds of metres offshore and they come in a variety of shapes, from alongshore-uniform (shore-parallel; Figure 1.1b) to alongshore-variable (e.g., Wright and Short, 1984; Lippmann and Holman, 1990; Van Enckevort et al., 2004). This large variability in sandbar appearance continues to fascinate nearshore researchers in a

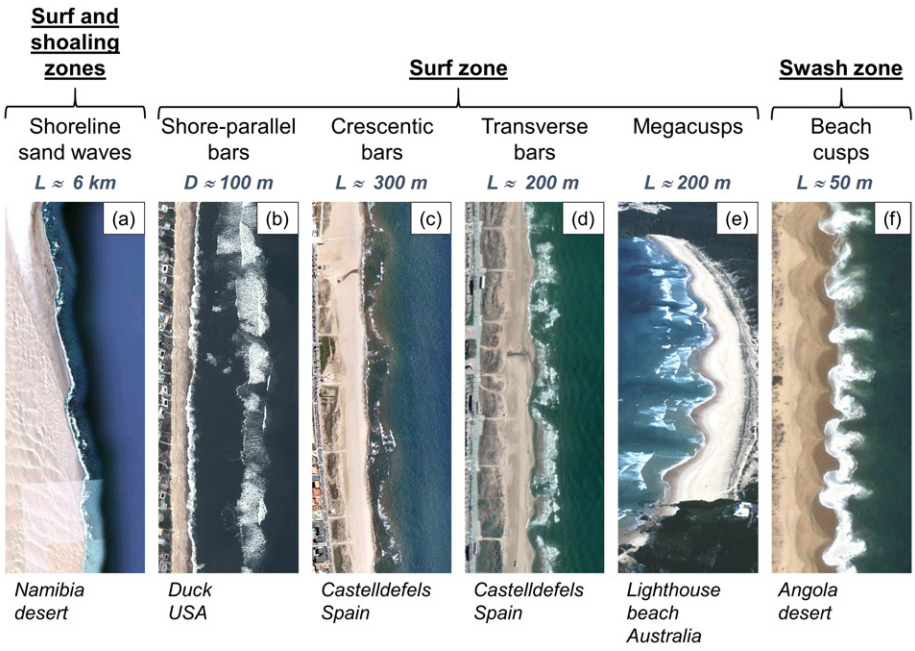

Figure 1.1 Examples of different types of morphological patterns that occur in the nearshore zone. Estimates of the wavelength L or distance from shore D are also given. Images are courtesy of Google Earth (panels a/b/d/f), Institut Cartogràfic i Geològic de Catalunya (panel c) and A.D. Short (panel e).

way similar to the past decades (e.g., King and Williams, 1949; Sonu, 1973; Bowman and Goldsmith, 1983; Nafaa and Frihy, 1993).

Crescentic bars (also called rip-channel systems) are one example of alongshore-variable sandbars (Figure 1.1c). They are characterized by an alongshore sequence of shallower (horns) and deeper (bays) sections alternating shoreward and seaward (respectively; Van Enckevort et al., 2004). Their wavelengths can vary from tens of metres to several kilometres and they are characterised by strong seaward rip currents in the deeper sections (Dalrymple et al., 2011; Castelle et al., 2016). It is generally accepted nowadays that crescentic bars develop due to a positive feedback ('bed-surf' mechanism) between the incipient morphology and the rip current circulation, with waves breaking more on the shallower shoals than in the deeper channels, causing onshore currents on the shoals and offshore currents at the channels (e.g., Calvete et al., 2005; Garnier et al., 2008; Castelle and Ruessink, 2011). However, there has been less agreement regarding the physical mechanisms resulting in crescentic bar straightening. For a long time, this was associated to high-energetic waves (e.g., Wright and Short, 1984; Van Enckevort et al., 2004), whilst more recent observations have indicated that obliquely incident medium-energy waves can also result in crescentic bar straightening when the alongshore current overwhelms the rip current circulation (e.g., Price and Ruessink, 2011; Garnier et al., 2013; Contardo and Symonds, 2015). Furthermore, the important role of cross-shore processes on crescentic bar development (Michallet et al., 2013) is not yet well understood. Transverse bars are another example of alongshore-variable sandbars that often develop when a crescentic bar welds to the beach (Figure 1.1d; Holman

et al., 2006), although there are other types of transverse bars (finger bars) that are unrelated to crescentic bars (Ribas et al., 2015). They can extend perpendicularly to the coast or with an oblique orientation. Megacusps are shoreline undulations consisting of horns (seaward protusions) and embayments (landward perturbations) that have alongshore wavelengths larger than that of beach cusps and smaller than those of shoreline sand waves (Figure 1.1e). They are mostly directly linked to transverse or crescentic bars, with megacusps often forming when transverse bars attach to the shoreline. In case megacusps and crescentic bars are simultaneously present they are often morphologically coupled (e.g., Sonu, 1973; Coco et al., 2005; Orzech et al., 2011; Van de Lageweg et al., 2013), either in phase (megacusp embayments in front of crescentic bar horns) or out of phase (megacusp embayments in front of crescentic bar bays). Understanding the evolution of nearshore sandbars is of interest for coastal management as they induce wave breaking and influence sediment transport patterns, but also because the morphological coupling between sandbar and beach/shoreline can lead to changes in beach width and alongshore variability in dune erosion (Thornton et al., 2007; Castelle et al., 2015). Furthermore, the rip currents that accompany crescentic bars are relevant for ecology (redistribution and offshore transport of nutrients and biota), cross-shore mixing of particles (sediments or pollutants) and also pose a significant safety risk for swimmers (e.g., Castelle and Coco, 2013; Castelle et al., 2016).

Traditionally, the different morphodynamic patterns that occur in the nearshore have been studied separately and under idealized conditions. As a result, only a few recent studies (Castelle et al., 2010; Van de Lageweg et al., 2013; Rutten et al., 2018) cover the possible interactions between them and many questions remain unanswered (Michallet et al., 2013). In particular, the processes leading to different types of coupling patterns are still not understood, even though a number of studies focused on this (Orzech et al., 2011; Van de Lageweg et al., 2013; Coco et al., 2020). Apart from that, there is a lack of suitable field observations that cover the emergence, evolution and disappearance of the various patterns that can be used to validate results of process-based modelling studies. To close this gap, there is a need for coastal observational studies at large time and spatial scales with good time and space resolution that focus on studying the development and interactions between different surf-zone morphological patterns. Furthermore, they should take into account the longshore and cross-shore processes that occur at different temporal and spatial scales. Finally, the observations should be correlated to local wave conditions to study the mechanisms leading to the observed morphodynamic evolution. Such studies demand constant monitoring of the nearshore zone.

Traditionally, topobathymetric surveys (GPS, sonar, multi-beam) were used to monitor the nearshore zone. Although these techniques provide very detailed measurements, they are also very expensive, time-consuming and limited to calm seas. Furthermore, the data is mostly discontinuous in space and time. These drawbacks do not apply to video observation techniques, as they are cheap to operate and are able to continuously monitor the nearshore zone (Lippmann and Holman, 1989; Holman and Stanley, 2007). This technique is nowadays often used to study nearshore morphodynamic patterns (both at the sandbars and at the shorelines; e.g., Van Enckevort et al., 2004; Price and Ruessink, 2011; Van de Lageweg et al., 2013; Segura et al., 2018) and this thesis also makes extensive use of this methodology.

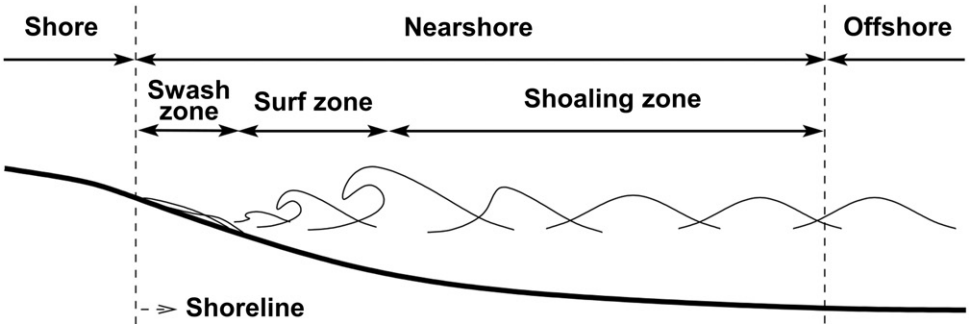

Figure 1.2 Overview of the coastal system (taken from Garnier, 2006).

1.3 Nearshore hydrodynamics

The most important external hydrodynamic forces in the coastal system are sea surface waves. They are normally separated in short waves (waves with periods below 20 seconds) and long waves (periods between 20 seconds and 40 minutes). Short waves can be subdivided in wind waves (generated by the local wind field) and swell (waves generated by wind fields far away that have travelled long distances over deep water), whereas examples of long waves include infragravity waves, harbour resonance and tsunamis. Waves with periods or recurrence intervals that exceed 1 hour, such as storm surges and the astronomical tide are usually referred to as sea level variations. Nearshore currents can be generated by tides, winds and storm surges. However, the focus of this thesis is on short waves, as they are the most important hydrodynamic forcing in the nearshore zone and the most relevant nearshore currents are induced by short waves. Therefore, this thesis simply refers to 'short waves' as 'waves'.

Wave conditions at different sites show a lot of variation, as a result of the prevailing wind climate and the local geographical setting. Properties of the wave field mainly depend on the characteristics of the wind field (speed, direction and duration), fetch of the wind field and the water depth in the area where waves are generated. Due to the constantly changing winds, waves show a large variability in heights, periods and directions. This means that the wave field in seas and oceans is the sum of a large number of harmonic waves generated by wind at various locations and times. As a result, describing waves in the time domain is complicated and they are often described using spectra in frequency and/or direction of the sea-surface elevation variance E. The 1D frequency spectrum $E(f)$, also called the variance density spectrum, can be obtained fairly easily (using Fourier transformation) from in-situ measurements of sea surface elevation. Obtaining the 2D frequency-direction spectrum $E(f, \theta)$ is more complicated as it requires instruments that measure directional properties of waves and typically also demands the use of data-adaptive methods or parametric models. Based on the variance density spectrum, various integrated wave parameters can be computed. Frequently used parameters (see Table 3.1 for more detailed definitions) are the significant wave height (H_{m0}), mean wave period (T_{m01}) as well as the mean zero-crossing period (T_{m02}). Furthermore, the peak period T_p is the inverse of the frequency corresponding to the peak in $E(f)$. Directional parameters like the mean wave direction θ_{mean} and directional spreading σ_θ can be obtained from instruments that measure directional properties of waves or from the 2D frequency-direction spectrum. General information about the theory behind

wave spectra can be found in Holthuijsen (2007) and additional details regarding measuring 2D frequency-direction spectra and directional parameters are provided in Appendix A.

When waves reach the nearshore zone, they are subjected to various types of transformation that are described in detail in Holthuijsen (2007) and summarised in the remainder of this paragraph. When waves approach at an angle with respect to the depth contours, the waves will slowly change direction so that they line up with the depth contours. This process is called refraction and is a result of waves propagating faster in deeper water compared to shallower water. When the water depth becomes less than approximately half the wavelength, the waves decelerate due to the decreasing water depth. This results in wave shoaling, in which the waves experience an increase in height due to energy conservation. When waves encounter a headland or breakwater, they will propagate into the shadow zone of the obstacle, leading to circular patterns of wave crests that quickly diminish in wave height. This process is called diffraction. Individual waves will start breaking when the wave height of the individual waves exceeds a certain percentage (~75%) of the local water depth (Holthuijsen, 2007). In large areas with shallow water, the wave height can also reduce when waves dissipate their energy due to bottom friction. Wave breaking can also occur in deep water, in which case it is referred to as whitecapping. This process is not well-understood, but it is partly related to the steepness of individual waves and probably also to the degree of randomness or short-crestedness of the individual waves (Holthuijsen, 2007).

Waves transport momentum through the so called radiation stresses (Longuet-Higgins and Stewart, 1964). They can be divided in cross-shore transport of cross-shore momentum (S_{xx}), alongshore transport of cross-shore momentum (S_{xy}) and alongshore transport of alongshore momentum (S_{yy}). The radiation stresses are not relevant in deep water, but in the nearshore they can induce significant changes in mean sea level (Longuet-Higgins and Stewart, 1962) and strong currents (Longuet-Higgins, 1970). When waves break in the surf zone, there are cross-shore gradients in S_{xx} that cause a local increase in water level. This is called the wave set-up and is related to the wave height at breaking. In the shoaling zone, cross-shore gradients in S_{xx} cause a local decrease in water level called set-down, which is typically much smaller than set-up. Cross-shore gradients in S_{xy} cause important longshore currents. In case of alongshore variability, alongshore gradients in S_{xy} and S_{yy} can also generate surfzone currents. All these currents, combined with the waves, create strong sediment transport patterns that modify the nearshore morphology.

The important role of waves in the nearshore zone means that accurate wave conditions are needed to study nearshore morphodynamic patterns. In particular, the angle of wave incidence is crucial in the evolution of nearshore sand bars, such as crescentic or transverse bars (e.g., Price and Ruessink, 2011; Ribas et al., 2012; Garnier et al., 2013; Contardo and Symonds, 2015). Preferably, measured wave conditions are used as they are the most accurate. Various types of wave measurement systems exist (Allender et al., 1989; O'Reilly et al., 1996; Pettersson et al., 2003), but the most commonly used instruments are wave buoys. These provide detailed data on wave height and period, and often also provide directional information (mean wave angle, directional spreading) as well as estimates of the 2D frequency-direction spectrum. However, their deployment is costly, meaning that they are mostly only located close to harbours or populated coastlines. This can be far from the region of interest, which is why large-scale wave models are often also used to obtain wave conditions. Such global hindcast models are typically based on codes such as WAM (The WADMI Group, 1988) and WAVEWATCH III (Tolman, 2009) and are forced using large-

scale wind fields obtained from atmospheric models. They have the advantage that they do not suffer from breakdowns and that wave conditions can be obtained relatively easy for any location on earth. However, the problem with using such models is that they mostly do not account for shallow-water processes and therefore may be less accurate in shallow water close to shore (Cavaleri et al., 2018). Furthermore, they rely on the accuracy of atmospheric models, which sometimes fail to reproduce wind fields in complex geographical settings (Bertotti et al., 2014). To obtain wave conditions in the nearshore, measured or modelled deep-water wave conditions are often transformed to shallow water using wave propagation models. A simple approach that is sometimes followed is to use linear wave theory based on ray approximation (e.g., Holthuijsen, 2007), although advanced models that include more physical processes like SWAN (Booij et al., 1999) are also often used. It is important to verify propagated wave conditions before using them in morphological studies so that potential errors in both the deep water wave source and the propagation method can be detected.

1.4 Research objectives and thesis outline

The main aim of this thesis is to understand the evolution and interactions of crescentic bars and megacusps, with a particular emphasis on the role of wave conditions and the nearshore bathymetry. For this, long-term observational data is used from the open, low-energetic, tideless beach of Castelldefels (20 km southwest of Barcelona, northwestern Mediterranean Sea). Available morphological data mainly consists of a long-term (October 2010–August 2018) dataset of hourly video images, which are complemented by irregular topobathymetric surveys at the study site. Furthermore, several datasets of measured and modelled wave conditions as well as measured tidal elevation and wind data are used to study the observed morphological evolution. Four research questions are defined. The first research question, which is methodological, focuses on obtaining optimal long-term wave conditions for Castelldefels beach out of the available long-term wave datasets. The subsequent three research questions are related with the sandbar and shoreline characteristics and the evolution of crescentic bars and megacusps. The final research question focuses on the interaction between crescentic bars and megacusps. The research questions are:

1. **Which method provides optimal directional wave conditions for nearshore field studies?**

2. **What are the geomorphological characteristics of the nearshore sandbars and the shoreline at Castelldefels beach?**

3. **What is the role of directional wave conditions on the formation, development and straightening of crescentic bars and megacusps?**

4. **How important is the shape of the cross-shore beach profile on the evolution of crescentic bars and megacusps?**

5. **How important is the morphological coupling between crescentic bars and megacusps and what are the underlying mechanisms?**

This thesis consists of 6 chapters. *Chapter 2* gives an overview of the Castelldefels field site and the various datasets used in this thesis. Apart from a detailed description of the geographical setting of the study site (including the prevailing wind and wave climate), extensive information is also given regarding the different morphological, hydrodynamic and meteorological datasets. This includes information on the instrument or model properties, as well as practical information about the contents, duration and locations of the different datasets.

Chapter 3 assesses the accuracy of the long-term wave models and propagation of the long-term measured wave conditions using linear wave theory or the SWAN wave model (forced using different boundary conditions) to obtain optimal directional wave conditions at shallow water in front of Castelldefels beach. A short-term dataset of measured wave conditions in front of the study site is used as ground truth and results are analysed for wave height, wave period and wave direction as well as different wave climates (shore-normal, shore-oblique and bimodal) using several statistical error parameters. This chapter ends with some recommendations to obtain accurate directional wave conditions for coastal studies in semi-enclosed and coastal seas.

Chapter 4 investigates crescentic bar dynamics at the study site using the long-term dataset of video images as well as propagated wave conditions obtained following the findings in *Chapter 3*. Using the video images, crescentic bar events are quantified and correlated to the wave and morphological conditions, paying special attention to the formation and straightening moments. The role of directional wave conditions and the cross-shore bathymetric configuration on crescentic bar development and straightening is analysed in detail. Finally, the findings of this chapter are compared to previous observations and used to validate or invalidate existing model studies.

Chapter 5 utilises the long-term dataset of video images and propagated wave conditions that are already used in *Chapter 4* to characterise megacusp events and the coupling between megacusps and crescentic bars at Castelldefels beach. Special attention is given to the role of directional wave conditions and the bathymetric configuration on megacusp formation/disappearance and the emergence of different coupling patterns. The outcomes of this analysis are compared to several previous observations and model studies that allow to formulate hypotheses as to why different coupling patterns arise.

Chapter 6 synthesises the most important conclusions of this thesis and provides an outlook to future research.


Barceloneta

Chapter 2 | Study site and datasets

2.1 Introduction

This thesis uses long-term field observations to study the development and interactions of crescentic bars and megacusps at the fetch-limited beach of Castelldefels (northwestern Mediterranean Sea). Several datasets are used that comprise hydrodynamic, meteorological and morphological data. Most of the morphological data consists of long-term video data with high spatial and temporal resolution, although sporadic topobathymetric measurements are also available. Together, they provide detailed information on the long-term morphological evolution of Castelldefels beach. The available hydrodynamic data consists of wave data from a variety of sources (measurements or large-scale models) as well as tide data, whereas the meteorological data comprises wind measurements at Barcelona airport. This chapter provides a detailed description of the study site and the datasets, starting with a geographical description of the study site (Section 2.2), followed by a detailed description of the available morphological data (Section 2.3) and ending with an overview of the hydrodynamic and meteorological data (Section 2.4).

2.2 Geographical setting

Castelldefels beach is located on the northwestern Mediterranean Sea along the Spanish Catalan coast, approximately 20 km southwest of Barcelona (Figure 2.1). It is an open, double-barred beach located in the middle of the Llobregat Delta, formed by a continuous stretch of beaches that extend over an alongshore distance of 18 km from the Garraf Mountain chain in the west to the Llobregat river outfall in the east. The study site is a 1 km beach section with an east–west alignment (89° with respect to the north). Castelldefels beach is mainly composed of sand with a median grain size of 270 μm and the nearshore bed slope is approximately 0.014. The bathymetry in the study area (Figure 2.1) shows a relatively wide shelf in front of the study site, whilst more to the east the shelf is narrower and the water depth quickly reaches more than 100 m.

The winds in the study area are strongly influenced by orographic barriers, which leads to a variable wind climate in space and time. The winds generally come from the north and northwest (particularly during December and January), whilst southerly and easterly winds are also important (mainly during February-April and November). The winds are generally not very strong and the maximum wind velocities occur during easterly storms that affect the entire Catalan coastline (Pallares et al., 2014). The wind patterns directly influence the local wave climate, which is characterized by calm wave conditions with sudden high energetic wave events (wave height above 1.5 m; Puertos del Estado, 1994). The long-term average values of the significant wave height H_{m0} and mean zero-crossing period T_{m02} at the Barcelona wave buoy (see Section 2.4) are 0.73 m and 3.8 s, respectively. On average, calm conditions

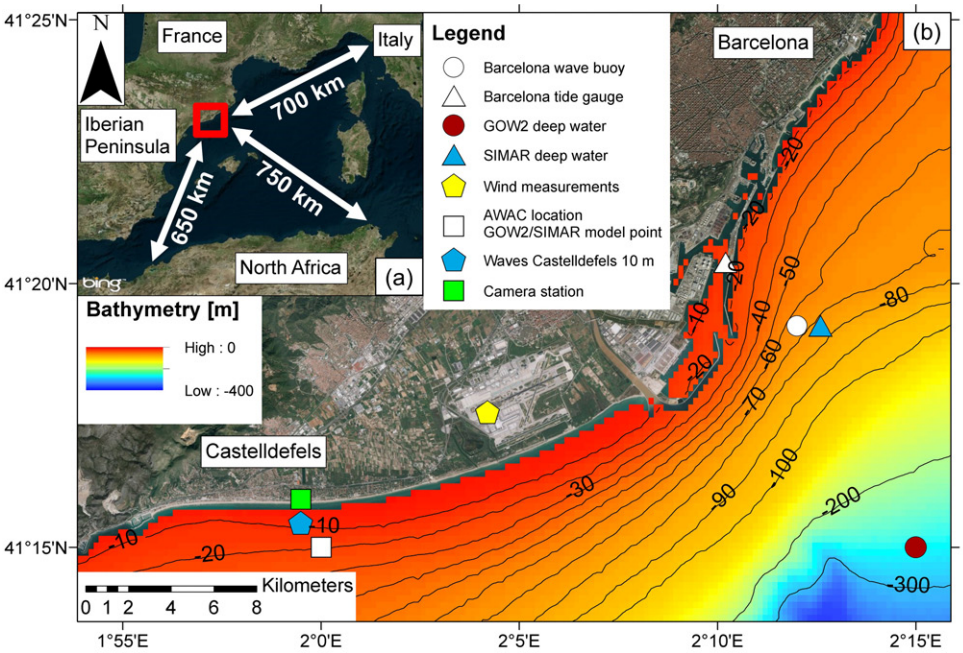

Figure 2.1 Overview map showing the Castelldefels study site. Panel (a) shows the regional setting (including longest available fetches) and panel (b) shows a detailed view of the study site surroundings including the nearshore bathymetry (obtained from the European Marine Observation and Data Network, www.emodnet-bathymetry.eu) and the locations of the different data sources used in this thesis. The aerial photography is part of Microsoft Bing Maps (© 2022 Microsoft Corporation Earthstar Geographics SIO).

prevail during the summer period and energetic conditions occur mostly from October to May (Sánchez-Arcilla et al., 2008). Storm waves along the Catalan coast are limited due to the short fetches (Figure 2.1a) and an average storm duration of less than 24 hours. As a result, mixed sea states composed of wave trains with more than one peak frequency and mean direction occur frequently (Sánchez-Arcilla et al., 2008). Near the study site, the wave climate is characterised by waves from two dominant directions (east-southeast and south-southwest) with average mean wave directions θ_{mean} of 100° and 176° (with respect to north), respectively. The largest waves come from the east, due to the longest available fetches and the stronger winds that generally blow from this direction (Sánchez-Arcilla et al., 2008; Bolaños et al., 2009). Tidal action in this part of the Mediterranean Sea is small, with a range of approximately 20 (10) cm during spring tide (neap tide; Simarro et al., 2015).

2.3 Morphological data

Studying coastal evolution at dynamic beaches like Castelldefels requires long-term datasets with high spatial and temporal resolution. Traditional techniques like GPS surveys and sonar-equipped watercrafts (MacMahan, 2001) provide very detailed measurements, but are time-consuming, expensive and limited to calm seas. These drawbacks do not apply to video

systems, as they are relatively cheap to operate and provide frequent (hourly) high-resolution images of the beach and nearshore zone on large temporal scales (often several km alongshore). Therefore, it is not surprising that many field studies investigating sandbar dynamics during the last decades used video data. The majority of the morphological data used in this thesis also consists of video images from a local video system.

During spring 2010, a video monitoring system was installed at Castelldefels beach at the top of a 30 m-high observation tower (Figure 2.2a). The system consists of five full-colour cameras that cover a 180° overview of the shoreline (Figures 2.2b-c and 2.3). The system uses the SIRENA open source code (Nieto et al., 2010) and operates since 5 October 2010. Each daylight hour, all the cameras produce one snapshot, one time-exposure and one variance image. The time-exposure images are obtained by averaging numerous instantaneous snapshots taken during a 10-min period. Similarly, the variance images are obtained by computing the standard deviation of the same set of snaphots (Holman and Stanley, 2007). The images of all five cameras are georeferenced, rectified and merged into a planview using the ULISES software (Simarro et al., 2017). The conversion from image to real-world coordinates is done by linking a set of clearly visible ground control points with known real-world coordinates to their image coordinates and using the local water level. The planviews used in this thesis (Figure 2.3) span 1000 m in the longshore and 300 m in the cross-shore direction and the pixel resolution is 0.5 m. The origin of the coordinate system (WGS84) in the planviews is the location of the camera system (41°15'54.7"N, 1°59'29.1"E).

This thesis studies the period from 5 October 2010 to 31 August 2018 (2888 days). On some occasions, the planviews did not cover the complete study area due to partial camera failure. These cases were only included in the planview dataset when at least 2 adjacent cameras were functioning. Furthermore, there were periods without any images, the longest being from 27 September 2016 to 30 January 2017 (126 days), due to a renovation of the camera system. During the remainder of the study period (2762 days), there were only 98 days

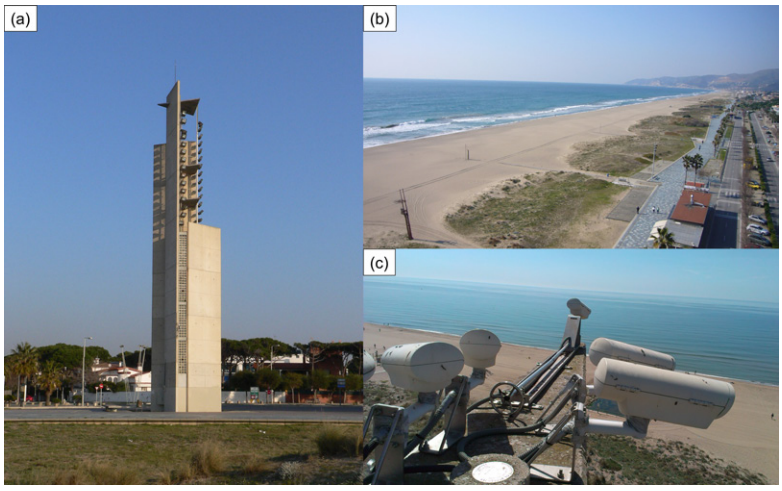

Figure 2.2 Overview of the video monitoring system at Castelldefels, showing (a) the observation tower, (b) the view from the top of the observation tower towards the southwest and (c) the five cameras that monitor the beach.

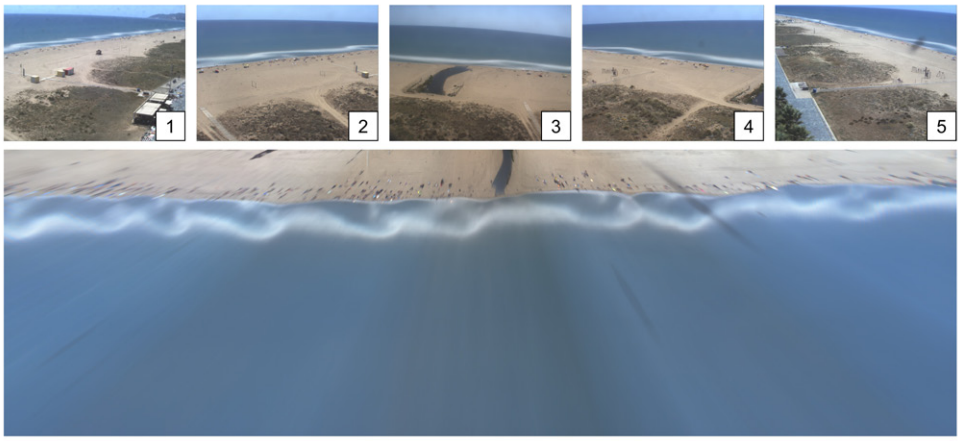

Figure 2.3 Example of time-exposure images obtained by the five cameras (top) and the resulting planview measuring 1000 m alongshore and 300 m cross-shore (bottom). The images were obtained on 9 May 2015 12:00.

without any images (due to camera malfunctions or insufficient image quality), meaning that images were available during 92% of the entire study period (2664 days). The time-exposure images (Figure 2.3) show the areas of dominant wave breaking as clear white stripes (which is a good proxy for the location of submerged sandbars; e.g., Holman and Stanley, 2007) and the shoreline is easy to identify as the border between the blue water and the yellow/brown beach. As a result, the number of images during the study period suited for analysis of sandbar evolution was further limited by insufficient wave breaking over the bars. Fortunately, this is an indication of low-energetic wave conditions that generally do not result in major morphological changes.

The camera images are complemented by a total of 9 topobathymetric surveys (Table 2.1) that were obtained irregularly during the study period and comprise the dry beach and the nearshore bathymetry up to a depth of 20 m (1700 m offshore). All surveys show a clear outer bar (between 100–200 m from the shoreline at a depth of 1.5–2.5 m) and the majority of the surveys indicate the presence of an inner bar or terrace (between 0–50 m from the

Table 2.1 Overview of the available bathymetric surveys during the study period.

Date	Notes
8 December 2011	No data in inner surf zone
1 June 2012	No data in inner surf zone
23 April 2013	No data in inner surf zone
9 October 2013	No data in inner surf zone
3 May 2014	No data in inner surf zone
8 May 2015	No data in inner surf zone
18 November 2015	Data available in inner surf zone (inner bar)
22 February 2017	Data available in inner surf zone (inner terrace)
18 January 2018	Data available in inner surf zone (no inner bar/terrace)

shoreline at a depth of 0.5–1.5 m). Unfortunately, 6 of the surveys lack data in the inner surf zone (depth between 0.5–1.5 m), making it impossible to distinguish between an inner bar, an inner terrace or no inner bar/terrace.

2.4 Hydrodynamic and meteorological data

For studying the evolution of Castelldefels beach, accurate wave conditions are needed in front of the study site at 10 m depth (Figure 2.1). No permanent wave buoy or other instrument is located directly in front of the study area, but waves were measured in front of the study site during a 9-day field campaign in March 2018. Furthermore, several long-term datasets comprising both measurements and large scale models contain hydrodynamic and meteorological data around Castelldefels. All datasets (short and long-term) are described in the following paragraphs.

2.4.1 Short-term wave measurements

A short-term dataset of wave conditions at 21 m depth in front of Castelldefels beach (Figure 2.1) was measured from 13 March tot 22 March 2018 using an Acoustic Waves and Currents (AWAC) sensor. The AWAC is both a current profiler and a directional wave system that is mounted in a stationary frame at the sea bottom.

During the measurement period, the AWAC provided half-hourly values of the spectral wave height H_{m0}, mean zero-crossing period T_{m02}, peak period T_p, mean direction θ_{mean}, peak direction θ_{peak} and mean directional spreading σ_θ, as well as half-hourly 1D variance density and 2D frequency-direction spectra. The AWAC used a frequency range of 0.02-0.49 Hz and a frequency resolution of 0.01 Hz to obtain all wave parameters and spectra. The full 2D frequency-direction spectra was estimated using the Maximum Likelihood Method (MLM; Krogstad et al., 1988). All important AWAC settings are summarized in Table 2.2. The data obtained by the AWAC is used as ground truth when investigating different methods to obtain optimal directional wave conditions at 10 m depth in front of Castelldefels (Figure 2.1) using the available long-term wave datasets (described in the next sections).

2.4.2 Long-term wave measurements

The only permanent instrument providing continuous wave data near the study area is the Barcelona wave buoy. It is located at 68 m depth in front of Barcelona harbour (Figure 2.1), managed by Puertos del Estado (the national Spanish Ports Authority) and operates since March 2004. It is a directional buoy proving hourly integrated wave parameters (wave height, wave period, wave direction, directional spreading) and hourly 2D frequency-direction spectra. The buoy is located relatively close to the study site (the distance between the buoy and the study site is approximately 20 km), but there is a significant change in shoreline orientation and the bathymetric contours (Figure 2.1). As a result, the waves at the Barcelona buoy cannot be used directly for deducing the wave climate at Castelldefels beach.

This Triaxys wave buoy (Miles et al., 2003) obtains the heave, pitch and roll motions by solving the equations of motions using standard Fourier analysis techniques (e.g., Kuik et al., 1988; Benoit et al., 1997). The heave time-series is then processed using both spectral analysis and zero-crossing analysis techniques to determine non-directional wave parameters and 1D variance density spectra for the frequency range 0–0.64 Hz with a resolution of 0.005 Hz. Variance density below 0.03 Hz is removed using a high-pass filter. Finally, the Maximum

Table 2.2 Overview of instrument and deployment settings for the Barcelona buoy and AWAC.

Device	AWAC	Barcelona buoy
Water depth	21 m	68 m
Sensor altitude above bottom	0.5 m	Tide-dependent
Burst interval	0.5 h (start 5 min past every half hour)	1 h (start at top of the hour)
Sampling rate	1 Hz	4 Hz
Length of processed time series	1200 points	5760 points
Start frequency	0.02 Hz	0.03 Hz
End frequency	0.49 Hz	0.64 Hz
Number of frequency bands	48	123
Number of directional bins	90	121
Directional spectrum method	Maximum Likelihood Method	Maximum Entropy Method
Start of deployment	13 March 2018 15:05	8 March 2004
End of deployment	22 March 2018 09:05	–

Entropy Method (MEM; Lygre and Krogstad, 1986) is used to estimate the 2D frequency-direction spectra using the 1D variance density spectra and the available cross-spectra.

For the entire study period, hourly values of the spectral wave height H_{m0}, mean zero-crossing period T_{m02}, peak period T_p, mean direction θ_{mean} and mean directional spreading σ_θ were obtained from the buoy, as well as the hourly 2D frequency-direction spectra. Integrated wave parameters were available during 97% of the study period and 2D spectra were available during 94% of the study period. All important settings of the buoy are summarized in Table 2.2.

2.4.3 Long-term wave data from global hindcast models

Other available wave data in the area is provided by several global hindcast models, two of which are used in this thesis. The first hindcast model is the SIMAR database, which is maintained by Puertos del Estado (Puertos del Estado, 2015b). This database contains wind, sea level and wave parameters for the entire Spanish coast and spans from 01/01/1958 until today. During the study period, the wind fields at 10 m above the sea surface were obtained using the regional HIRLAM model (Undén et al., 2002). These wind fields were then used in both WAM (The WADMI Group, 1988) and WAVEWATCH III (Tolman, 2009) to obtain the wave fields along the Spanish coastline. The HIRLAM model resolution was 9 km during 2010–2012 and improved to 3 km during 2012–2018 (Puertos del Estado, 2015b). The resolution of the wave grids in the Mediterranean Sea was 5 km for the entire study period. Data output is available every 3 hours for the period 2010–2012 and each hour for the period 2012–2018 (Puertos del Estado, 2015b). A detailed description of the SIMAR database can be found in Gómez Lahoz and Carretero Albiach (2005).

The SIMAR database has multiple data points in front of the Barcelona coast. One of these data points is directly in front of the study site (41.25 N, 2.0 E) at a depth of 21 m (see Figure 2.1). However, the SIMAR database assumes deep water in the entire model domain and does not incorporate the effects of bottom friction. As a result, another data point located next to the Barcelona wave buoy (41.32 N, 2.21 E) at a depth of approximately 75 m was also used. For both output points, several wave parameters provided by the SIMAR database (spectral wave height H_{m0}, mean zero-crossing period T_{m02}, peak period T_p and mean direction θ_{mean}) were obtained for the entire study period.

The second hindcast model used in this thesis is the GOW2 database, which is developed and maintained by the hydraulic institute IH Cantabria (Perez et al., 2017). It is based on the numerical model WAVEWATCH III and provides wave data for the period 01/01/1979 until today. During the study period, the GOW2 model was forced by the Climate Forecast System Reanalysis (CFSR, Saha et al., 2010) during 2010 and by the updated CFSv2 database (Saha et al., 2014) for the period 2011–2018. The grid used in GOW2 for coastal continental areas has a resolution of 0.25°× 0.25° which amounts to approximately 21 km × 28 km (lon × lat) in the Barcelona area.

Although GOW2 has a coarser resolution compared to SIMAR, it also has an output point at the same location as the SIMAR database in front of Castelldefels at 21 m depth (Figure 2.1). Analogous to SIMAR, a second data point was selected (at deeper water) located closest to the Barcelona buoy (41.25 N 2.25 E) at a depth of approximately 250 m (Figure 2.1). From both points, hourly time series of significant wave height H_{mo}, mean zero-crossing period T_{mo2}, peak period T_p and mean direction θ_{mean} were obtained for the entire study period.

2.4.4 Other long-term datasets

In addition to the wave datasets described in the previous sections, long-term datasets of tidal elevation and wind measurements are also used in this thesis. Tidal elevation data was obtained from the tide gauge located in the Barcelona harbour (Figure 2.1). This tide gauge provides sea level elevation every 5 min by measuring the sea level during an entire minute using a sampling interval of 0.5 seconds (Puertos del Estado, 2015a). The sea level data was obtained for the entire study period and primarily used for georeferencing the images of the video monitoring system (Section 2.3).

Finally, the last dataset used in this study consists of hourly wind data (mean directions and velocities), that were measured at Barcelona Airport (Figure 2.1) by a weather station of the Spanish State Meteorological Agency (AEMET). No weather station is located in Castelldefels, but the weather station at Barcelona Airport is located close to the study site (7 km away) in an open area close to sea, meaning that the recorded winds will be quite similar to the winds at sea in front of Castelldefels. Another weather station is located slightly closer to the study site (5 km away), but it was decided not to use the data from this weather station as it is located more inland in the vicinity of some buildings (that will affect the wind measurements). The hourly wind data for the entire study period at Barcelona Airport were taken at 4 m above ground and transformed to 10 m above ground using the log wind profile. In the end, this data was only used to investigate whether accounting for wind in the wave propagation model resulted in more accurate directional wave conditions in front of the study site.

Chapter 3 | Optimal estimations of directional wave conditions for nearshore field studies

Abstract

Accurate directional wave conditions at shallow water are crucial for nearshore field studies and necessary as boundary conditions for morphodynamic models. However, obtaining reliable results for all wave parameters can be challenging, particularly regarding wave direction. Here, the accuracy of two global hindcast models and propagation of measured wave conditions using linear wave theory or the SWAN wave model (forced by integrated wave parameters or 2D spectra) is assessed to obtain directional wave conditions at shallow water for Castelldefels beach, northwest Mediterranean Sea. Results are analysed using different statistical error parameters and for different wave climates (shore-normal, shore-oblique and bimodal). The analysis shows that global hindcast models correctly predict the trends in wave height and mean wave period but predictions for mean wave direction are only accurate for shore-normal waves. Linear wave theory provides good results for wave height but underestimates refraction, resulting in significant errors in mean wave direction for shore-oblique waves. Finally, SWAN forced with 2D spectra results in the most accurate predictions for all wave parameters. When using integrated wave parameters as boundary conditions, the results for wave height and mean period stay the same whilst the errors in peak period and mean direction worsen for shore-oblique and bimodal wave climates. The reason is that for these wave conditions the directional spectrum constructed out of integrated wave parameters does not resemble the actual directional spectrum.

Based on:

De Swart, R. L., F. Ribas, D. Calvete, A. Kroon, and A. Orfila (2020). Optimal estimations of directional wave conditions for nearshore field studies. *Continental Shelf Research* 196.104071. doi:10.1016/j.csr.2020.104071.

3.1 Introduction

Many shorelines around the world are highly dynamic and change due to wave action. Understanding this behaviour is important for present day coastal zone management and for estimating the vulnerability to climate change (Vitousek et al., 2017). Incoming waves are the most important forcing for coastal evolution, and wave characteristics in shallow water depend on the local coastal setting (wave climate, bathymetry, shoreline orientation). Unfortunately, obtaining reliable wave conditions in coastal and inner seas is still a difficult task, especially in semi-enclosed seas like the northwestern Mediterranean Sea (Bolaños-Sanchez et al., 2007; Cavaleri et al., 2018). The reason is that this region is characterized by limited fetches, a complex bathymetry with deep canyons, significant changes in shoreline orientation and strong variations in the wind climate (Sánchez-Arcilla et al., 2008).

Wave conditions can be obtained from a variety of sources. The preferred source for wave conditions are devices that provide real-time measurements. Different types of wave measurement instruments exist (e.g., Allender et al., 1989; O'Reilly et al., 1996; Pettersson et al., 2003), but wave buoys are the most common worldwide. However, wave buoys are scarce because they are quite expensive to deploy and maintain. As a result, they are mostly deployed in areas where there is a great need for real-time wave measurements (typically near harbours or populated coastlines). For studying other locations, the measured offshore waves need to be transformed to nearshore study sites using a wave propagation model.

In addition to buoy measurements, wave conditions can also be obtained from global hindcast models, based on codes such as WAM (The WADMI Group, 1988) and WAVEWATCH III (Tolman, 2009). Hindcast models typically also assimilate observations and have the advantage that they do not suffer from breakdowns. Furthermore, results can theoretically be acquired for any worldwide location, including those where no other data is available. However, these models may not be accurate in shallow waters (Cavaleri et al., 2018), and proper wave propagation might also be needed.

There are different ways to propagate wave conditions to shallow waters. The simplest method is to use linear wave theory based on ray approximation (e.g., Holthuijsen, 2007). Despite its crude assumptions, this method is often applied in nearshore studies to quickly obtain reasonable estimates of the wave conditions. A more thorough method is to use more advanced wave models like SWAN (Booij et al., 1999). Such models include more physical processes and have been extensively used in the past in nearshore regions with gradually variable bathymetry (e.g., Ris et al., 1999). The SWAN model has the additional advantage that it is a spectral model, meaning that it solves the spectral action balance equation without any a priori restrictions on the spectrum for the evolution of wave growth. Spectral models can either be forced by integrated wave parameters or using full 2D spectra.

Good predictions of wave height and wave period are important for, e.g., management of harbours, navigation or fisheries. However, wave direction is crucial in coastal engineering because even small variations in wave direction can already substantially affect estimates of longshore sediment transport (e.g., Soomere and Viška, 2014), along with the related dynamics of embayed beaches (Harley et al., 2015) and beach nourishments (Arriaga et al., 2017). On the other hand, nearshore studies in the past typically focused on relating beach morphodynamics to wave height and wave period only (e.g., Van Enckevort et al., 2004; Gómez-Pujol et al., 2007), whereas wave direction was often neglected. However, more recent studies indicated that wave direction plays a major role in the evolution of morphodynamic patterns,

such as crescentic bars (Calvete et al., 2005; Price and Ruessink, 2011), transverse finger bars (Ribas and Kroon, 2007; Ribas et al., 2012), high angle wave instability and km-scale shoreline sand waves (Ashton et al., 2001; Arriaga et al., 2018).

Wave conditions used in nearshore studies are typically obtained by propagation of offshore buoy measurements or hindcast model results. This can lead to errors, so that verification of the propagated wave conditions against local measurements is essential. However, many previous nearshore studies showed only limited or no verification of wave conditions (e.g., Splinter et al., 2011; Arriaga et al., 2018). On the other hand, studies that focused on modelling wave fields in coastal regions with large-scale hindcast models (sometimes coupled to SWAN to increase resolution in the nearshore) mostly verified wave height and period with typical errors of 0.25 m and 1.5 s in both wind-sea and swell conditions (e.g., Pallares et al., 2014; Amrutha et al., 2016), whilst wave direction was often not included (e.g., Bolaños-Sanchez et al., 2007; Perez et al., 2017). In the few studies with hindcast models where wave direction was also validated (e.g., Pallares et al., 2014; Amrutha et al., 2016), the corresponding errors were large (> 40°). The errors in wave direction can be substantially reduced by propagating measured wave conditions (Gorrell et al., 2011). Unfortunately, there is a lack of studies that compare the reliability of different methods to obtain directional wave conditions for nearshore studies, especially in semi-enclosed and coastal seas.

The aim of this study is to establish the accuracy of different methods to obtain wave conditions in shallow water for nearshore studies, with a special focus on the wave direction. This is done for the field site of Castelldefels beach, which is located on a limited-fetch, complex-geometry sea (northwest Mediterranean Sea) and has already been described in detail in Chapter 2 (Section 2.2). Three long-term sources of wave conditions are available near this site: a buoy and output points of two hindcast models (see Sections 2.4.2 and 2.4.3). An instrument was deployed to measure wave conditions in front of the field site at 21 m depth during a 9-day experiment (more details in Section 2.4.1). This allows to compare five different methods to obtain wave conditions at the field site from the long-term sources (Section 3.2). Three methods consist of propagating measured wave conditions from the offshore buoy using models with different degrees of complexity: the simple wave ray model, SWAN forced by integrated wave parameters and SWAN forced by 2D spectra. The two last methods use the results of the two hindcast models directly. Despite the short duration of the field campaign, distinct wave climates occurred, which allowed to characterize the accuracy of each method under different wave conditions (Section 3.3). The significance of the findings

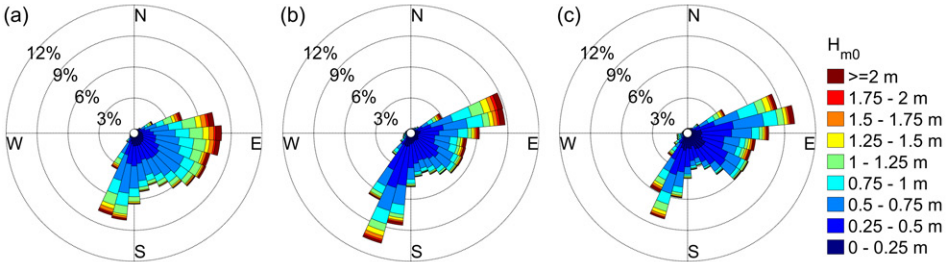

Figure 3.1 Wave roses of (a) the long-term wave climate at the Barcelona buoy, (b) the SIMAR output point next to the Barcelona buoy and (c) the GOW2 output point nearest to the Barcelona buoy for the period September 2012–May 2018 in terms of spectral wave height H_{mo} and mean direction θ_{mean}.

of this study and the advantages and disadvantages of the different methods are discussed in Section 3.4, and the conclusions are listed in Section 3.5.

3.2 Methods

3.2.1 Data comparison

In this study, three long-term sources of wave conditions were used (a wave buoy and two global hindcast models), which have already been extensively described in Chapter 2 (Sections 2.4.2 and 2.4.3). Furthermore, that chapter also includes the description of the AWAC sensor that was deployed to measure waves at 21 m depth in front of Castelldefels beach during a 9-day field campaign (Section 2.4.1). This allowed to validate five different methods to obtain wave conditions at the field site from the long-term wave datasets. The AWAC data was used as ground truth and the errors of the different methods with respect to the ground truth were evaluated using the root mean square error (*RMSE*), *BIAS* and normalised root mean square error (*NRMSE*), defined as

$$RMSE = \sqrt{\frac{\sum_{i=1}^{N}(S_i - A_i)^2}{N}} \quad , \tag{3.1}$$

$$BIAS = \frac{\sum_{i=1}^{N}(S_i - A_i)}{N} \quad , \tag{3.2}$$

$$NRMSE = \frac{RMSE}{\sigma_A} \quad , \tag{3.3}$$

in which S denotes the simulated data from the various propagation methods and A denotes the measured data from the AWAC (ground truth). The number of data points is denoted by N, whilst σ_A denotes the standard deviation of the AWAC measurements. Angles with respect to North were used as input when computing these quantities for angular values. This was appropriate, because wave directions in the study area were such that no jumps from 360 to 0 degrees occurred.

3.2.2 Definition of wave parameters

The 2D frequency-direction spectrum, $E(f,\theta)$, represents the frequency-direction density spectrum of the sea-surface elevation variance E, defined as $E = \int_{f_{low}}^{f_{high}} \int_0^{2\pi} E(f,\theta) df d\theta$. The 1D frequency spectrum $E(f)$ is related to $E(f,\theta)$ by the expression $E(f) = \int_0^{2\pi} E(f,\theta) d\theta$ and in a similar way it is possible to define a 1D direction spectrum as

$$E(\theta) = \int_{f_{low}}^{f_{high}} E(f,\theta) df \quad . \tag{3.4}$$

Here, the symbol E denotes the sea surface elevation variance regardless of the unit. The units are m²/Hz for $E(f)$, m²/deg for $E(\theta)$ and m²/Hz/deg for $E(f,\theta)$. Notice that the surface elevation variance multiplied by $\frac{1}{2}\rho g$ is equal to the total energy E_{tot} of the waves per unit surface area. Lastly, by changing f_{low} and f_{high}, it is possible to apply high- and low-pass filters, respectively. Various integrated wave parameters can be computed from the obtained spectra (Table 3.1). Additional information about obtaining 2D spectra and computing directional wave parameters is given in Appendix A.

It is important to note that the peak frequency f_p and thus the peak period T_p obtained from buoy measurements can have a large variability. This is especially true for multi-modal spectra, where the observed maximum can easily switch between multiple frequency peaks. The mean period generally does not have this problem, which is why it is common to define a synthetic peak period, T_p^*, as a function of the mean zero-crossing period T_{m02} (Rogers and Wang, 2007). The relation used here is $T_p^* = 1.33T_{m02}$, which is the average of the relations between T_p and T_{m02} given for the Pierson-Moskowitz and JONSWAP spectral shapes (see Soulsby, 1998). In this study, the synthetic peak period was used as input in both the simple wave ray propagation model (Section 3.2.3) and for the SWAN model forced with integrated wave parameters (Section 3.2.4). The randomness in f_p also directly affects the measurements of θ_{peak}, meaning that mean direction θ_{mean} is a more stable parameter.

To force the simple wave ray and SWAN models, all integrated wave parameters (except T_p^*) were obtained directly from the buoy. For the hours that no buoy data was available, the integrated wave parameters were computed from the available 1D and 2D spectra using the expressions in Table 3.1.

3.2.3 Simple wave propagation model

The first model that was used to propagate waves from deep water to the study site is a simple wave propagation model that is based on ray approximation (linear wave theory) and assumes monochromatic waves and parallel depth contours. First, the dispersion relationship is applied

$$\omega_r^2 = gk\tanh(kD), \tag{3.5}$$

where $\omega_r = 2\pi/T$ is the relative radian frequency (with T being the wave period), g is the gravity acceleration, $k = 2\pi/\lambda$ is the wave number (λ being the wavelength) and D is the water depth (m). Note that in this case the current contribution (Doppler shift) is neglected because at the AWAC it was smaller than 1% for 96% of the time (maximum contribution was 1.8%). The absence of an ambient current means that in our case ω_r was equal to the

Table 3.1 Definitions of integrated wave parameters computed from 1D frequency and 2D frequency-direction spectra, where the Fourier coefficient $a_1^*(f)$, $b_1^*(f)$, a_1 and b_1 are given in Appendix A or computed from the buoy measurements.

Parameter	Definition
n^{th} moment of 1D frequency spectrum	$m_n = \int_0^\infty f^n E(f)df$
Spectral wave height	$H_{m0} = 4\sqrt{m_0}$
Root-mean square wave height	$H_{rms} = \frac{H_{m0}}{\sqrt{2}}$
Mean wave period	$T_{m01} = \frac{m_0}{m_1}$
Mean zero-crossing period	$T_{m02} = \sqrt{\frac{m_0}{m_2}}$
Wave period at peak of spectrum	$T_p = \frac{1}{f_p}, \quad E(f_p) = \max E(f)$
Mean wave direction per frequency	$\theta_{mean}^*(f) = \tan^{-1}\left[\frac{b_1^*(f)}{a_1^*(f)}\right]$
Mean direction for entire spectrum	$\theta_{mean} = \tan^{-1}\left[\frac{b_1}{a_1}\right]$
Mean directional spreading for full spectrum	$\sigma_\theta = \sqrt{2[1-r_1]}, \quad r_1 = \sqrt{a_1^2 + b_1^2}$
Peak wave direction	$\theta_{peak} = \theta_{mean}^*(f_p)$

absolute radian frequency ω ($\omega = \omega_r + \vec{k} \cdot \vec{u}$ with $\vec{k}$ and $\vec{u}$ being the wave number and ambient current velocity vectors, respectively). Knowing T, D_0 and D_1 (the subscripts denote the conditions at deep and shallow water respectively), a Newton's numerical scheme is used to solve equation 3.5 (T and thus ω are assumed to be constant), which gives k_0 and k_1. Second, the model applies Snell's law,

$$k_1 \sin\theta_1 = k_0 \sin\theta_0, \tag{3.6}$$

where θ is the angle of incidence with respect to the shore normal. Finally, the model applies wave energy conservation, i.e. importing a constant cross-shore wave energy flux F_x (assuming alongshore uniformity),

$$H^2_{rms_1} c_{g_1} \cos\theta_1 = H^2_{rms_0} c_{g_0} \cos\theta_0, \tag{3.7}$$

where H_{rms} is the root-mean-square wave height and c_g the wave group velocity. The wave group velocity is computed using standard linear wave theory. Knowing H_{rms_0}, equation 3.7 provides H_{rms_1}. The model inputs were H_{rms} for the wave height (characteristic wave height for wave energy), synthetic peak period T_p^* for the wave period and θ_{mean} for the angle of incidence (see section 3.2.2).

3.2.4 SWAN wave propagation model

3.2.4.1 Model description

SWAN (Simulating Waves Nearshore) is a third-generation spectral wave model that describes the evolution of the 2D frequency-direction spectrum in coastal regions and inland waters by accounting for many relevant physical processes (Booij et al., 1999). The SWAN model, as WAM and WAVEWATCH III, is based on the spectral action balance equation with sources and sinks, but SWAN is specifically designed for coastal areas. Usually, wave models use the action density N (defined as $N = E/\omega_r$ where ω_r is the relative radian frequency), because it is conserved when propagating in the presence of an ambient current (Whitham, 1974). Note that in our case ω_r is equal to the absolute radian frequency ω because ambient currents were negligible (as explained in Section 3.2.3). The action balance equation in Cartesian coordinates reads (e.g., Komen et al., 1994)

$$\frac{\partial N}{\partial t} + \frac{\partial c_x N}{\partial x} + \frac{\partial c_y N}{\partial y} + \frac{\partial c_{\omega_r} N}{\partial \omega_r} + \frac{\partial c_\theta N}{\partial \theta} = \frac{S_{tot}}{\omega_r} \quad , \tag{3.8}$$

where c_x, c_y, c_{ω_r} and c_θ are the group velocities in x, y, ω_r and θ space. The right hand side of equation (3.8) contains S_{tot}, which is the source/sink term and includes six physical processes that are important in generating, dissipating, or redistributing wave energy: the wave growth by wind, the nonlinear transfer of wave energy through three-wave (triad) and four-wave (quadruplets) interactions, the wave decay due to whitecapping, bottom friction and depth-induced wave breaking. More information about these terms can be found in the SWAN Scientific and technical documentation (SWAN Team, 2018a).

3.2.4.2 Model setup

The SWAN model Cycle III version 41.20A was used in this study with spherical coordinates and nautical convention. The model domain consists of a curvilinear grid that stretches approximately 60 km alongshore and follows the coastline and the bathymetric line of the Barcelona buoy (68 m; Figure 3.2). The spatial resolution varies throughout the grid and is

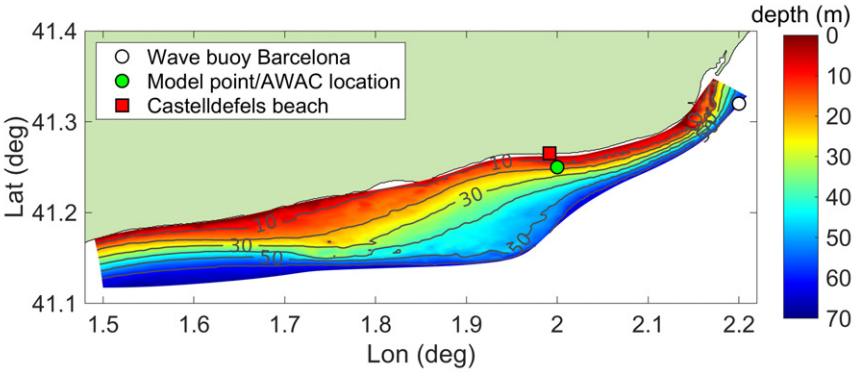

Figure 3.2 SWAN domain including detailed bathymetry that is used to propagate the waves to the study site.

approximately 200 m around the AWAC location. The grid bathymetry was obtained from the EMODnet database and has a resolution of 120 m (Figure 3.2). The landward boundary of the SWAN model is set at approximately 10 m depth, because the EMODnet database becomes unreliable for shallower depths. The output point in front of Castelldefels beach (the AWAC location and the GOW2/SIMAR output point) is located at 21 m depth.

In this study, SWAN was used in 2D non-stationary mode, and stationary computations (recommended for domains smaller than 1 deg) with a maximum of 15 iterations per computation. The frequency grid contained 38 logarithmically spaced values in the range 0.03–1 Hz, with the recommended frequency resolution of $df/f = 0.1$ (SWAN Team, 2018b) and the directional resolution used was 5°. The default JONSWAP formulation for bottom friction was used with a coefficient value of 0.038 m^2s^{-3}. Many different sensitivity tests were conducted to determine the default settings (Section 3.3.4.2). Following the results of these sensitivity tests, the default third-generation physics formulation of Komen et al. (1984) was used, whilst whitecapping, quadruplets, depth-induced breaking, triad wave-wave interactions and wind growth were switched off. The integrated wave parameters obtained with SWAN at the AWAC location were integrated over the frequency range of the AWAC (0.02–0.49 Hz), following the recommendations of Pallares et al. (2014).

Two types of offshore wave conditions were used in this study to force SWAN. Firstly, a single set of integrated wave parameters (the most commonly used SWAN forcing) was used from which SWAN computed an artificial single-component JONSWAP spectrum with a default peak enhancement factor $\gamma = 3.3$. The integrated wave parameters used were H_{mo}, synthetic T_p^*, θ_{mean} and σ_θ (see also Section 3.2.2). The SWAN manual (SWAN Team, 2018b) states that the wave direction θ_{peak} should be used for forcing but in this study the mean direction θ_{mean} was used instead. This choice was made because θ_{peak} directly depends on f_p, which is not a reliable parameter in buoys (see Section 3.2.2). Secondly, SWAN was forced with the full 2D frequency-directional spectra, which are the most detailed measurements of the wave climate that can be obtained from the buoy. Note that when SWAN was forced with 2D frequency-direction spectra only the energy that propagated into the domain was taken into account. Furthermore, the Barcelona buoy has a fine linear frequency resolution of 0.005 Hz and a directional resolution of 3°, whilst in SWAN the frequency resolution was

coarser and logarithmic and the directional resolution was 5°. Thus, the buoy spectra were interpolated to the frequencies and directions used by SWAN.

The boundary conditions were imposed along the entire south boundary of the grid but not in the lateral boundaries. However, since the region of interest is in the centre of the domain and the domain is sufficiently wide, the absence of lateral boundaries did not influence the results. The offshore waves were assumed to be alongshore uniform and equal to those at the Barcelona buoy.

3.3 Results

After a description of the wave conditions during the field campaign, the performance of the different methods is validated using the hourly AWAC data. A total of 211 values are available for the SIMAR and GOW2 hindcast models, 188 for the simple wave ray model and 207 for the SWAN simulations. It is stressed that the results for T_p shown in this section refer to the actual measured or modelled peak period and not the previously mentioned synthetic T_p^*.

3.3.1 Wave conditions during field campaign

The wave climate during the 9-day field campaign was dominated by south-southeasterly waves during the first 6 days, after which east-southeasterly waves were present (Figure 3.3a and 3.4). During the majority of the campaign, the wave conditions were quite energetic (H_{mo} > 0.5 m). Only on 14 March, H_{mo} dropped below 0.5 m, whilst the largest H_{mo} was registered on 18 March (1.8 m at the buoy and 1.9 m at the AWAC).

The various datasets of the campaign were separated into three different wave climates: southerly, easterly and bimodal. This separation was made based on the measured 2D frequency-direction spectra at the Barcelona wave buoy. The criteria for classifying a wave climate as easterly or southerly were that at least 70% of the wave energy came from that direction. If this was not the case, the wave climate was classified as bimodal. The threshold angle (147°) to discriminate between easterly and southerly wave energy was set by computing the average mean direction for both the easterly and southerly wave conditions and subsequently taking the mean. As a result, southerly wave climates were

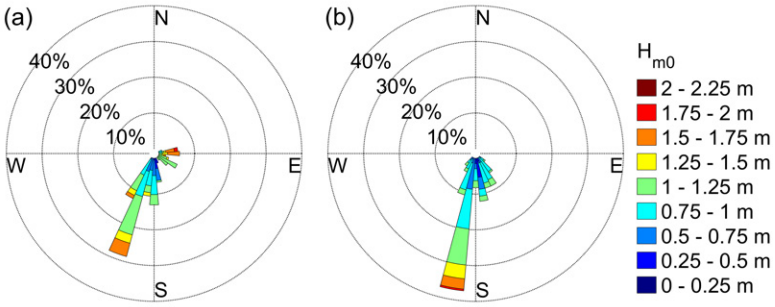

Figure 3.3 Wave roses showing the wave climate during the field campaign at (a) the Barcelona buoy and (b) the AWAC in terms of spectral wave height H_{mo} and mean direction θ_{mean}.

Table 3.2 Statistical values (mean, standard deviation, minimum and maximum) of integrated wave parameters measured at the Barcelona buoy and AWAC during the field campaign for the entire period and the different wave climates.

Wave climate	Method	H_{m0} [m] Mean, stdev, min, max	T_{m02} [s] Mean, stdev, min, max	T_p [s] Mean, stdev, min, max
Full period	Buoy	1.0, 0.32, 0.40, 1.8	4.8, 0.84, 2.9, 7.7	7.0, 1.4, 3.9, 10
	AWAC	0.88, 0.26, 0.34, 1.8	5.0, 0.82, 3.4, 7.7	7.2, 1.9, 3.2, 11
Southerly	Buoy	0.97, 0.27, 0.40, 1.7	4.7, 0.88, 2.9, 7.7	6.6, 1.3, 3.9, 10
	AWAC	0.91, 0.27, 0.34, 1.8	4.8, 0.83, 3.4, 7.7	6.5, 1.6, 3.2, 10
Easterly	Buoy	1.5, 0.26, 0.80, 1.8	5.6, 0.49, 4.9, 6.6	8.2, 1.2, 6.3, 10
	AWAC	0.91, 0.14, 0.55, 1.1	5.6, 0.64, 4.1, 6.7	9.6, 0.81, 6.8, 11
Bimodal	Buoy	0.94, 0.31, 0.40, 1.3	4.8, 0.58, 3.3, 6.1	7.4, 1.3, 5.4, 10
	AWAC	0.77, 0.25, 0.34, 1.1	5.1, 0.68, 3.4, 6.4	7.7, 1.8, 4.4, 10
		θ_{mean} [deg] Mean, stdev, min, max	θ_{peak} [deg] Mean, stdev, min, max	
Full period	Buoy	169, 43, 74, 213	– – – –	
	AWAC	180, 20, 130, 225	180, 24, 32, 244	
Southerly	Buoy	196, 11, 171, 213	– – – –	
	AWAC	191, 11, 164, 225	191, 20, 32, 244	
Easterly	Buoy	86, 7, 74, 99	– – – –	
	AWAC	145, 11, 130, 174	150, 9, 135, 175	
Bimodal	Buoy	128, 27, 75, 173	– – – –	
	AWAC	162, 11, 131, 199	161, 16, 130, 197	

present during 68% of the field campaign, easterly wave climates occurred during 11% of the time and bimodal wave climates were present during 21% of the time (Figure 3.4).

Table 3.2 shows the statistics of 5 integrated wave parameters during the complete field campaign and for the different wave climates. The average wave height during southerly and bimodal wave climates was quite similar, but it increased during easterly wave climates. During easterly and bimodal wave conditions, the wave direction at the AWAC changed with respect to the Barcelona buoy due to refraction and the average wave height decreased.

As shown in Figure 3.1a, easterly waves are important in the overall wave climate of the Barcelona buoy, which is why the easterly waves that occurred during the end of the field campaign were analysed in detail. Moreover, propagating these easterly waves was more challenging because they experienced strong refraction before reaching Castelldefels due to the change in shoreline orientation, whilst southerly waves only experienced limited changes (see data at AWAC in Figure 3.3b and Figure 3.4).

3.3.2 Results of large-scale hindcast models

Results of the SIMAR and GOW2 database during the field campaign at the AWAC location are shown in Figure 3.5, in yellow and purple colours, respectively. The modelled trends in H_{m0} and T_{m02} agree quite well with the measurements. This is also clear from Table 3.3, which contains the statistical errors for the various wave parameters and the different wave climates. On average, both models underpredict T_{m02} but the general pattern in the mea-

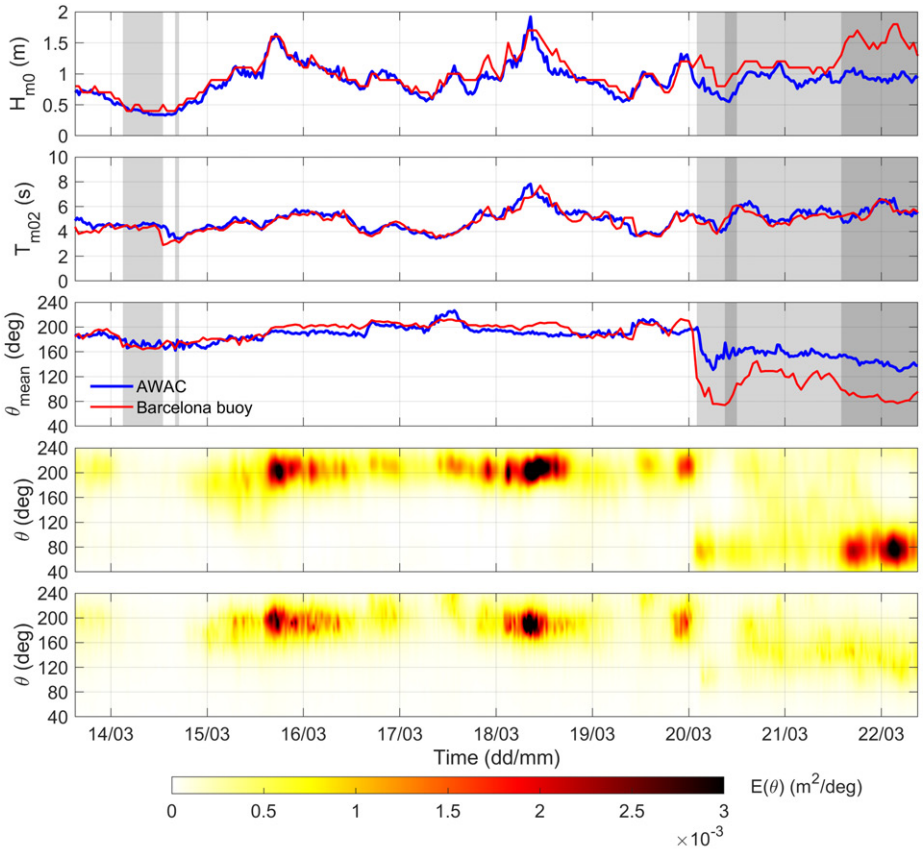

Figure 3.4 Time series of integrated wave parameters and 1D directional spectra during the field campaign. The three top plots show, respectively, the spectral wave height H_{m0}, mean zero-crossing period T_{m02} and mean direction θ_{mean} both for the Barcelona buoy and the AWAC. The last two plots shows the 1D directional spectrum $E(\theta)$ measured by the Barcelona buoy and the AWAC respectively. The background shading in the three tops plots indicates the different wave climates; white for southerly, light-grey for bimodal and dark-grey areas for easterly wave climates.

sured data is still captured. Regarding θ_{mean}, both models show large deviations. During southerly waves, the errors in direction are moderate (they can be as much as 40°), but they increase significantly for easterly waves (up to 80° or even more). Both models predict waves at Castelldefels coming from the east, whilst in reality these waves had refracted substantially and came more from the south-southeast.

3.3.3 Results of simple wave ray model

The results of the simple wave ray model are also shown in Figure 3.5 (in green) and in Table 3.3. Please note again that the wave period remains unchanged when using this model. The modelled H_{m0} and T_{m02} agree quite well with the measurements, although errors in modelled H_{m0} are significant during easterly wave conditions. Regarding T_p and θ_{mean}, the model shows good agreement for southerly waves. For easterly waves, θ_{mean} improves compared

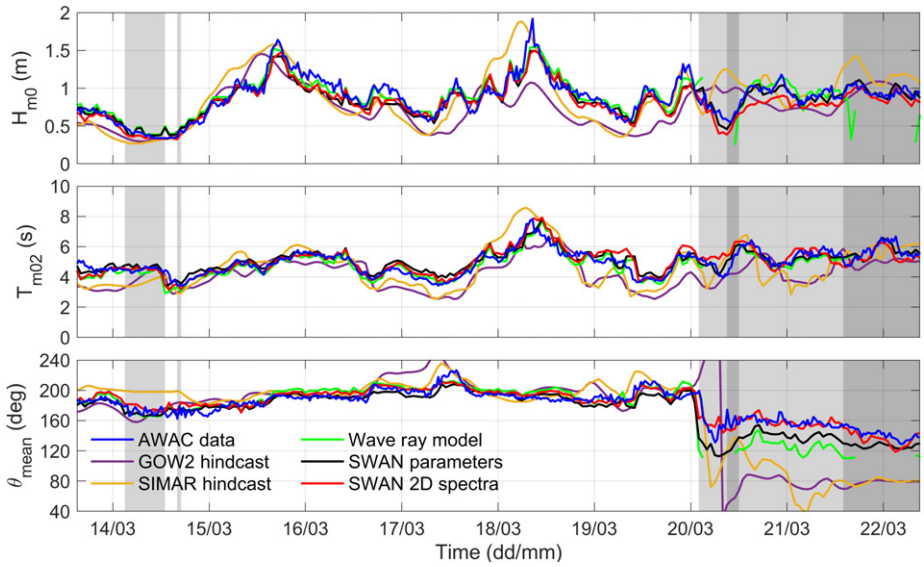

Figure 3.5 Time series of integrated wave parameters during the field campaign at the AWAC location. From top to bottom, the spectral wave height H_{m0}, mean zero-crossing period T_{m02} and mean direction θ_{mean} are shown for different data sources (AWAC measurements or one of the models). The background shading indicates the different wave climates; white for southerly, light-grey for bimodal and dark-grey areas for easterly wave climates.

with those of the GOW2 and SIMAR databases, but errors are quite high (up to 40°). The performance of θ_{mean} for the different wave climates is shown in Figure 3.6a. The gaps in the time series of the simple wave ray model during easterly wave conditions are a result of the model only being able to propagate waves in Barcelona buoy that have a direction ±90° with respect to the shore-normal at Castelldefels beach.

3.3.4 Results of SWAN model

3.3.4.1 SWAN default settings

The results of the default SWAN simulation forced with integrated wave parameters are shown in Figure 3.5 and in Table 3.3. The modelled results of H_{m0} and T_{m02} agree well with the measurements for all wave climates, but T_p, θ_{mean} and θ_{peak} are only reproduced well for southerly waves. The modelled θ_{mean} shows an improved performance for easterly and bimodal wave climates when compared to the results of the simple wave ray model, but the error in modelled θ_{mean} is still substantial (Figure 3.6b). Moreover, although not shown in previous comparisons, notice that the results of θ_{peak} worsen compared to θ_{mean} (particularly the *RMSE*).

When forcing SWAN with 2D spectra, H_{m0} and T_{m02} are again well reproduced, but also T_p shows much more similarity with the measurements (Figure 3.5 and Table 3.3). Most importantly, θ_{mean} shows good agreement with the measurements for all wave climates (Figure 3.6c). Finally, the *RMSE* in θ_{peak} increases compared to the default SWAN simulation forced with integrated wave parameters (although the *RMSE* was already large), but the *BIAS* improves.

Table 3.3 Statistical errors of the different wave parameters for the various methods during the full period and for the three wave climates. Entries in italics indicate the cases for which *NRMSE* > 1.

Wave climate	Method	H_{m0} [m] *RMSE, BIAS, NRMSE*	T_{m02} [s] *RMSE, BIAS, NRMSE*	T_p [s] *RMSE, BIAS, NRMSE*
Full period	GOW2	0.26, −0.14, 0.98	*1.0, −0.77, 1.2*	1.7, 0.28, 0.94
	SIMAR	0.24, 0.004, 0.92	*0.95, −0.32, 1.2*	1.6, 0.64, 0.86
	Wave ray model	0.14, −0.001, 0.53	0.42, −0.13, 0.51	1.4, −0.57, 0.74
	SWAN parameters*	0.11, −0.036, 0.41	0.41, 0.11, 0.50	1.5, −0.82, 0.82
	SWAN 2D spectra*	0.12, −0.07, 0.47	0.46, 0.08, 0.56	0.82, 0.006, 0.44
Southerly	GOW2	0.28, −0.18, 1.0	*0.96, −0.74, 1.2*	*1.7, 0.41, 1.1*
	SIMAR	0.24, −0.041, 0.87	*0.88, −0.22, 1.1*	1.6, 0.59, 1.0
	Wave ray model	0.10, 0.009, 0.38	0.43, −0.12, 0.51	1.0, −0.31, 0.67
	SWAN parameters*	0.12, −0.047, 0.44	0.43, 0.18, 0.52	1.1, −0.39, 0.69
	SWAN 2D spectra*	0.12, −0.056, 0.44	0.43, 0.13, 0.52	0.69, −0.002, 0.44
Easterly	GOW2	*0.18, 0.06, 1.3*	*0.92, −0.67, 1.4*	*0.9, −0.42, 1.1*
	SIMAR	*0.31, 0.28, 2.3*	*0.68, 0.22, 1.1*	*1.4, 0.59, 1.7*
	Wave ray model**	*0.46, −0.14, 3.4*	0.34, 0.089, 0.52	*2.5, −0.80, 3.0*
	SWAN parameters*	0.06, −0.005, 0.44	0.47, 0.053, 0.73	*2.5, −2.3, 3.0*
	SWAN 2D spectra*	0.094, −0.076, 0.70	0.62, −0.18, 0.96	*1.0, −0.18, 1.3*
Bimodal	GOW2	0.21, −0.083, 0.85	*1.2, −0.94, 1.8*	*2.1, 0.22, 1.1*
	SIMAR	0.20, −0.070, 0.81	*1.2, −0.92, 1.8*	1.8, 0.84, 0.97
	Wave ray model	0.096, 0.040, 0.39	0.39, −0.27, 0.57	*2.0, −1.3, 1.1*
	SWAN parameters*	0.076, −0.015, 0.31	0.31, −0.069, 0.46	*2.0, −1.4, 1.1*
	SWAN 2D spectra*	0.14, −0.11, 0.57	0.46, 0.047, 0.67	1.0, 0.13, 0.57
		θ_{mean} [deg] *RMSE, BIAS, NRMSE*	θ_{peak} [deg] *RMSE, BIAS, NRMSE*	
Full period	GOW2	*44, −11, 2.2*	– – –	
	SIMAR	*37, −9.7, 1.8*	– – –	
	Wave ray model	18, −3.9, 0.87	– – –	
	SWAN parameters*	14, −7.3, 0.66	22, −6.6, 0.90	
	SWAN 2D spectra*	8.1, 0.94, 0.40	*26, 0.92, 1.1*	
Southerly	GOW2	*13, 6.7, 1.2*	– – –	
	SIMAR	*12, 8.5, 1.1*	– – –	
	Wave ray model	8.3, 3.7, 0.74	– – –	
	SWAN parameters*	7.5, −2.5, 0.67	17, 2.4, 0.83	
	SWAN 2D spectra*	7.2, 2.3, 0.65	18, 8.2, 0.93	
Easterly	GOW2	*72, −70, 6.8*	– – –	
	SIMAR	*60, −59, 5.7*	– – –	
	Wave ray model**	*38, −13, 3.6*	– – –	
	SWAN parameters*	*21, −19, 2.0*	*31, −29, 3.5*	
	SWAN 2D spectra*	10, −7.5, 0.95	*43, −40, 4.9*	
Bimodal	GOW2	*77, −37, 7.1*	– – –	
	SIMAR	*65, −44, 5.9*	– – –	
	Wave ray model	*31, −24, 2.8*	– – –	
	SWAN parameters*	*21, −17, 1.9*	*29, −24, 1.9*	
	SWAN 2D spectra*	9.6, 0.95, 0.88	*32, −0.80, 2.1*	

*Results are shown for default SWAN settings

**Only 8 datapoints available due to most wave directions < 90° with respect to North

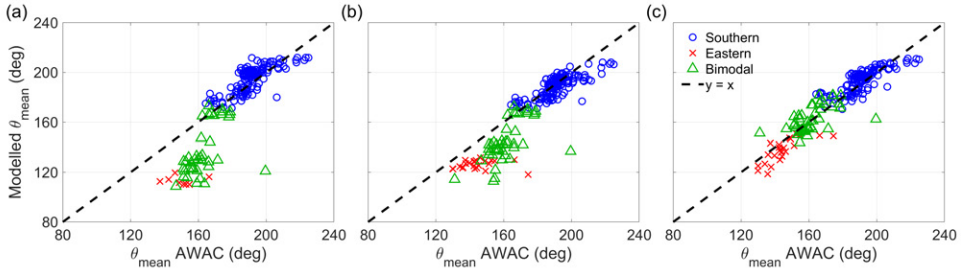

Figure 3.6 Scatterplots showing θ_{mean} modelled using (a) the simple wave ray model, (b) SWAN forced with integrated wave parameters and (c) SWAN forced with 2D spectra versus AWAC measurements. The colours denote the different wave climates.

3.3.4.2 Sensitivity to changing SWAN settings

Several sensitivity tests were conducted to find the default SWAN settings (see Section 3.2.4) for both forcing types. These tests can be separated into numerical tests (grid refinement and increasing frequency resolution), tests of physical processes (including quadruplets and whitecapping with and without wind) and methodological tests (default integration range, choice of SWAN input parameters, changing spectral shape and directional spreading value). Refining the grid by a factor 3 or increasing the frequency resolution by a factor 2 did not improve the results. This proves that the chosen numerical resolution is sufficient. The results also remained the same when including quadruplets and whitecapping as physical processes, although Battjes (1994) states that these processes are important in coastal waters. The probable reason is that the domain used in this study is fairly small (less than 10 km cross-shore) and measured wave conditions were imposed at the boundary instead of using wind data for wave generation. When wind was also included in the computations (using measurements from Barcelona Airport; see Section 2.4.4), the results for θ_{mean} worsened when forcing with 2D spectra (*RMSE* increased from 8 to 10° and *BIAS* from 1 to 3.5°). On the contrary, the results for θ_{mean} improved slightly when forcing with integrated wave parameters (*RMSE* decreased from 14 to 13° and *BIAS* improved from −7 to −5°). The rest of the parameters stayed approximately the same. It is also possible to change the frequency range that is used in SWAN to compute the integrated wave parameters. When applying no cutoff frequency (as done in SWAN default settings) instead of using the frequency range of the AWAC (Section 3.2.4.2), the results for T_{m02} slightly worsened (*RMSE* increased by at most 0.1 s whilst the *BIAS* could worsen 0.2–0.3 s). Again, the rest of the parameters did not display any changes.

A choice had to be made regarding the input wave period (T_{m01} or T_p) and wave angle (θ_{mean} or θ_{peak}) when forcing SWAN with integrated wave parameters. As explained in Section 3.2.2, a synthetic peak period was used in this study that was computed from the T_{m02} measured by the buoy. When using T_{m01} instead (computed from the buoy 1D frequency spectra), no changes were observed in the results. When using θ_{peak} instead of θ_{mean}, the results for H_{m0} and T_{m02} were similar, but errors increased substantially for T_p, θ_{mean} and θ_{peak}. The results remained the same when changing the spectral shape from JONSWAP for fetch-limited seas (Hasselmann et al., 1973) to Pierson-Moskowitz for fully developed seas (Pierson and Moskowitz, 1964). Finally, when forcing with integrated wave parameters the directional spreading σ_θ can be set to a constant value instead of using the time-variable mea-

sured data. Tests were done for constant σ_θ ranging from 10° to 60° with a step size of 10°. The SWAN user manual advises a σ_θ of 30° and the results indicate that this value gives the best results. For smaller values of σ_θ, the errors in θ_{mean} and θ_{peak} increased substantially (*RMSE* increases from 14 to 18–21° and from 22 to 24–26° respectively), whilst the errors remained the same for higher values of σ_θ. Changing σ_θ did not lead to changes in the rest of the parameters.

3.4 Discussion

3.4.1 Performance of wave propagation methods

In this work, the results of different wave modelling approaches with measured data are analysed. Despite the short duration of the field campaign, the different wave climates that occurred allow to distinguish some clear characteristics of the different methods. The assessment is done based on the statistical errors defined in Section 3.2.1 and this section provides a discussion of the results for the three different wave climates: southerly (~5° from shore-normal at 21 m depth), easterly (~30° from shore-normal at 21 m depth) and bimodal wave climates. An error is deemed acceptable when $NRMSE \leq 1$, i.e., when the *RMSE* < standard deviation. The cases that do not meet this requirement are marked in italics in Table 3.3. The confidence limit of θ_{mean} was estimated by Kuik et al. (1988) to be 5–10° in terms of *RMSE*.

For southerly waves, the three propagation methods give good results for all wave parameters (Table 3.3). The main reason for this is that propagating the (nearly shore-normal) southerly waves is straightforward. As a result, the simplifications of the simple wave ray model (monochromatic waves and parallel depth contours) do not affect the propagation of these waves. When forcing SWAN with 2D spectra, the only clear improvement is obtained for T_p. This is a result of differences in the 2D spectra between the simulations. Figure 3.7 shows the measured 2D spectra in the buoy and in the AWAC together with the modelled spectra for SWAN forced with a single set of integrated wave parameters (used to build a single-component JONSWAP spectrum) and SWAN forced with the measured 2D spectrum. Using 2D spectra as forcing leads to modelled 2D spectra at the buoy and AWAC locations that are very similar to the measured 2D spectra. When forcing with integrated wave parameters, the modelled 2D spectra are slightly wider in direction and the frequency peak is smaller. However, the energy distribution is generally correct in the latter case indicating that the single-component JONSWAP spectrum generally works well in southerly wave climates.

For easterly waves, the simple wave ray model performs badly ($NRMSE > 1$ for all parameters except T_{m02}, see Table 3.3), and in particular refraction is strongly underestimated. Using SWAN forced with integrated wave parameters improves the results for H_{m0} and θ_{mean}, although the errors in T_p and θ_{mean} are large and refraction is still underestimated. Forcing SWAN with 2D spectra leads to a big improvement in T_p and θ_{mean} and most parameters show a $NRMSE < 1$. In particular, refraction is well captured and the *RMSE* of θ_{mean} is only 10°. The reason is that forcing SWAN with 2D spectra results in modelled 2D spectra similar to the observed ones (Figure 3.8), also at the AWAC. When forcing SWAN with integrated wave parameters, the modelled spectrum at the Barcelona buoy is much wider in direction compared to the observed spectrum and only displays one peak in frequency (in reality there were several). At the AWAC, the energy in the modelled spectrum is much more concentrated in direction (hence the higher energy values), whilst in reality there is

much more spread in direction. For these easterly waves, the single-component JONSWAP spectrum does not work well because it can not represent multiple frequency peaks and it is too wide in direction. The performance of the wave ray model is worse than that of SWAN with integrated wave parameters. This is a result of the crude simplifications, in particular the assumption of an alongshore-uniform bathymetry. As a result, the refraction of easterly waves over the alongshore-variable bathymetry is not correctly reproduced. Furthermore, as mentioned before, the waves that arrive at the Barcelona buoy with a direction < 90° with respect to North can not be considered with the simple wave ray model (hence the gaps in Figure 3.5).

For bimodal wave climates, the only tested method to accurately propagate waves is forcing SWAN with 2D spectra ($NRMSE < 1$ for all wave parameters except θ_{peak}). SWAN forced with integrated wave parameters leads to modelled spectra that differ greatly from the measurements (Figure 3.9). The single-component JONSWAP spectrum is not valid for bimodal wave climates because the directional distribution used only allows for one directional peak in the 2D spectrum and the distribution on both sides of the directional peak is symmetrical. The result is that the directional peak is located in an area where in reality no energy is present (the mean of the two wave fields). Consequently, the resulting errors in T_p and θ_{mean} are large, although H_{m0} and T_{m02} are still relatively well reproduced. The simple wave ray model also performs well for H_{m0} and T_{m02} but the errors in T_p and θ_{mean} are large. The causes for these errors are twofold. First, the simple wave ray model assumes monochromatic waves, meaning that all wave energy is concentrated in a single set of integrated wave parameters, which is not sufficient to accurately describe bimodal wave climates. Second, the

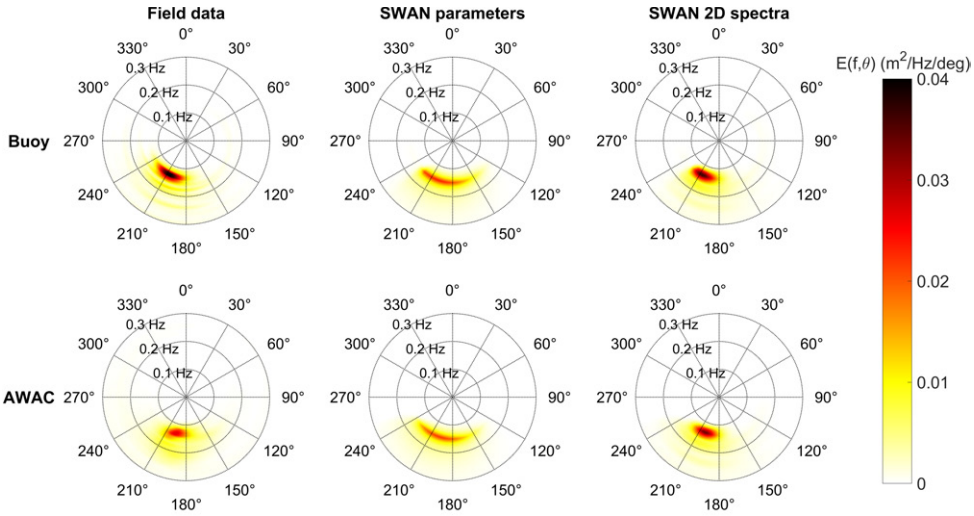

Figure 3.7 Measured and modelled 2D frequency-direction spectra $E(f, \theta)$ for a southerly wave climate (15 March 2018 20:00 UTC). From left to right the results are shown for the measured data, SWAN forced with integrated wave parameters and SWAN forced with 2D frequency-direction spectra (data in both cases taken from the Barcelona buoy). The top row shows the results for the Barcelona buoy location and the bottom row the results for the AWAC location at Castelldefels. Wave conditions at the Barcelona buoy/AWAC: H_{m0} = 1.3/1.3 m, T_{m02} = 5.0/5.1 s, θ_{mean} = 202/193°.

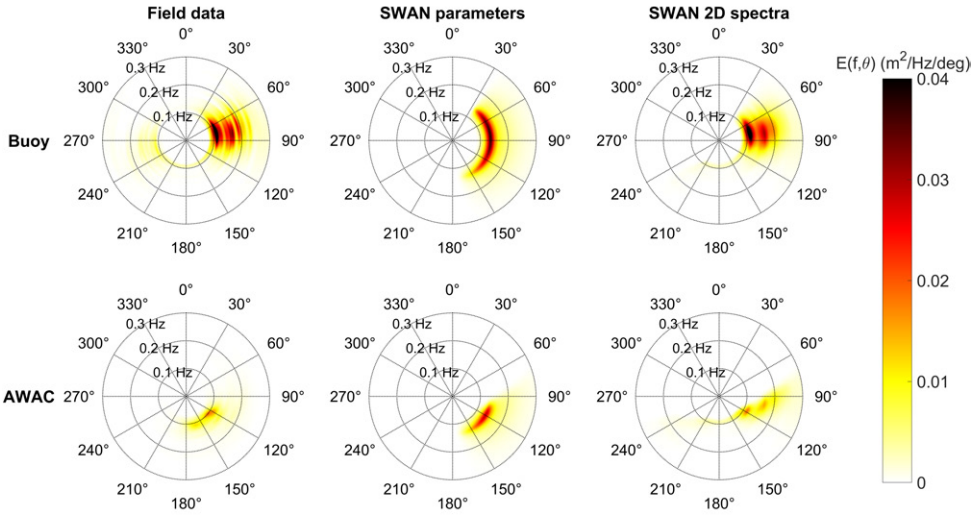

Figure 3.8 Identical to Figure 3.7, but now for an easterly wave climate (22 March 2018 03:00 UTC). Wave conditions at the Barcelona buoy/AWAC: H_{m0} = 1.8/1.0 m, T_{m02} = 5.6/6.7 s, θ_{mean} = 80/136°.

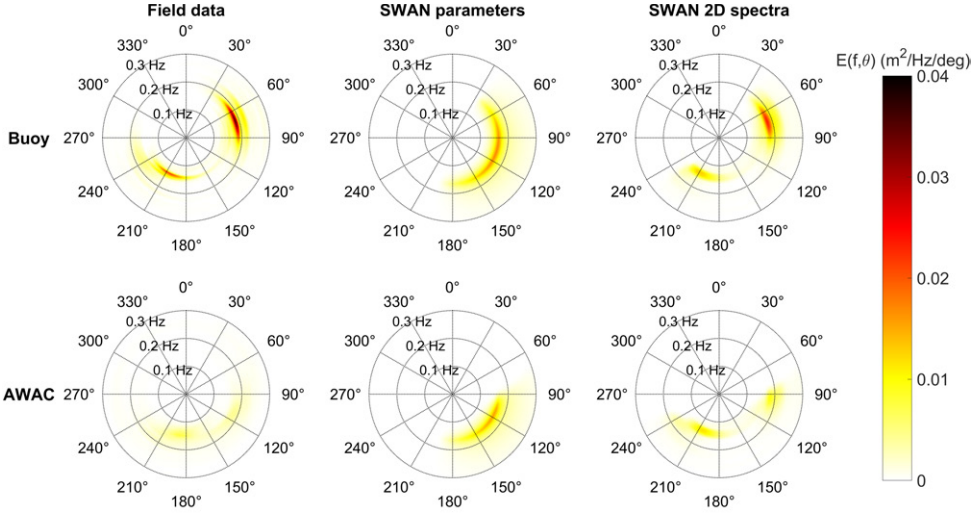

Figure 3.9 Identical to Figures 3.7 and 3.8, but now for a bimodal wave climate (20 March 2018 03:00 UTC). Wave conditions at the Barcelona buoy/AWAC: H_{m0} = 1.3/0.9 m, T_{m02} = 4.6/5.0 s, θ_{mean} = 107/164°.

model assumption of alongshore uniform bathymetry leads to an inaccurate reproduction of wave refraction (as explained before).

The above discussion highlights the importance of using high quality boundary conditions when propagating waves over alongshore-variable bathymetries. The simple wave ray model used straightforward boundary conditions (wave height, wave period and wave direction), that work well for shore-normal waves but are not accurate enough for shore-oblique

waves and bimodal wave climates. When applying a spectral wave model like SWAN, the boundary conditions are more detailed because either integrated wave parameters (including directional spreading) were used to build the 2D spectra or the measured 2D spectra were applied explicitly. However, a 2D spectrum constructed out of a single set of integrated wave parameters can be significantly different from measured spectrum because a certain combination of H_{m0}, T_p^*, θ_{mean} and σ_θ can fit to many different spectral shapes. As noted by Portilla-Yandún et al. (2015) and Cavaleri et al. (2018), a lot of detailed information that is available in the full 2D spectrum is blurred or lost when only using the integrated wave parameters. The present study underlines that, in the Catalan coast, this is critical for easterly and bimodal wave climates, where a single set of integrated wave parameters is unable to accurately describe the complex wave spectrum. This mostly affected the results of T_p and θ_{mean}, whilst for H_{m0} and T_{m02} no changes were noticed. When using the full 2D spectrum as boundary conditions, it was possible to obtain accurate results for T_p and θ_{mean} in all wave climates, which is in agreement with previous research on the western American coast (Gorrell et al., 2011). Furthermore, notice that for both forcing types the errors in θ_{peak} are much larger compared to θ_{mean} (for the three wave climates). The results using integrated wave parameters might improve in case the 2D spectrum is reconstructed out of multiple sets of wave parameters (e.g., Portilla-Yandún et al., 2015) instead of using a single set.

3.4.2 Performance of hindcast models

The two hindcast models (SIMAR and GOW2) correctly predicted the trends in wave height and wave period (Table 3.3) for all wave climates, whilst the errors for θ_{mean} were very large for shore-oblique waves and bimodal wave climates. There are several reasons for these mismatches. Global hindcast models typically have coarse spatial resolution (5 km for SIMAR and 0.25° for GOW2), which is not sufficient to take into account the necessary details in changes in the orientation of the shoreline, bathymetry and orography (Cavaleri et al., 2018). Apart from that, global hindcast models are often used without shallow water physics and without incorporating the effects of bottom friction. Furthermore, the output points of the two hindcast models in front of the study site are located at a shallow depth of 21 m. Using data from an output point at deeper water and propagating this data with SWAN might yield better results. To test this, data from SIMAR and GOW2 output points located closest to the Barcelona buoy at deeper water (75 m and 250 m respectively; Figure 2.1) were compared to the measured data from the Barcelona buoy (at 68 m depth). Again substantial differences are seen between the modelled and measured wave data (Figure 3.1). The results for H_{m0} (*RMSE* of 0.2 m for both models), T_{m02} (*RMSE* of 1.0 and 0.6 s respectively) and T_p (*RMSE* of 1.5 and 1.4 s respectively) are good for both models, but the errors in θ_{mean} (*RMSE* of 37° for both models) remain large. The match between the modelled and measured wave climates at deeper water is not deemed sufficient (particularly for wave direction) to use deep water hindcast data as input for the wave propagation models. Furthermore, propagating this data with SWAN would lead to the same problems that occurred when forcing SWAN with integrated wave parameters from the buoy.

Another reason that hindcast models display large errors in wave direction is that they are forced by wind fields from atmospheric models that can contain important errors (Bolaños-Sanchez et al., 2007). Unfortunately, it is difficult to obtain reliable wind fields in coastal and semi-enclosed seas (like the Mediterranean Sea), due to the strong spatial and temporal gradients in wind speed and direction (Cavaleri et al., 2018). Various studies (e.g., Ardhuin

et al., 2007; Mentaschi et al., 2015) demonstrated that choosing a different wind model or changing the resolution of the wind model can strongly affect the results of wave models in the Western Mediterranean Sea. Specifically for the Catalan coast, Bertotti et al. (2014) tested four different atmospheric models as input for the same wave model. The results showed that during non-extreme but complicated wave conditions (consisting of multiple wave systems), none of the atmospheric models was able to correctly reproduce all the observed wind patterns (each model missed at least one of the wind systems), which in turn led to an incorrect representation of the wave field.

Other studies that used large-scale wave models forced by wind fields and focused on the Catalan coast (e.g., Bolaños-Sanchez et al., 2007; Alomar et al., 2014; Pallares et al., 2014) also indicated that errors in the modelled wave fields were mainly related to inaccuracies in the wind fields. Although typically only wave height and wave period were validated, Bolaños-Sanchez et al. (2007) also compared measured and modelled 1D frequency spectra in which they found large differences, particularly for cases with multiple frequency peaks. Pallares et al. (2014) obtained good results for wave height and wave period but large errors in mean direction (*RMSE* above 40–60° depending on the study period). Amrutha et al. (2016), a similar study in the Eastern Arabian Sea that also used a large-scale wave model forced by wind, found good agreement for mean direction during monsoon periods (*RMSE* of 13°), but errors increased substantially outside this period because the wind patterns were not correctly simulated. Finally, the study by Rogers and Wang (2007) focused on modelling directional wave properties in Lake Michigan using SWAN forced by wind measurements from two buoys. They found better results for θ_{mean}, with an *RMSE* of 17°.

3.4.3 Recommendations

Based on the results discussed above, the following recommendations can be given to obtain directional wave conditions for coastal studies in semi-enclosed and coastal seas that are surrounded by a relevant orography. Coarse-resolution hindcast models (or fine-resolution models forced by coarse atmospheric models) usually reproduce the trends in wave height and mean period correctly, meaning that in most cases they can be safely used after applying some simple calibration methods (e.g., bias correction). In particular, both SIMAR and GOW2 results are nowadays used extensively to evaluate global changes in wave energy (e.g., Rodriguez-Delgado et al., 2018) and can be very useful for engineering applications such as predicting beach inundation and harbour management or for ecological studies (e.g., De la Hoz et al., 2018). However, the large errors in wave direction make global hindcast models not suited for nearshore morphodynamic studies in semi-enclosed and coastal seas.

In such environments, the alternative is to propagate measured offshore wave conditions. In case the wave parameters of interest are wave height and mean period (but not direction), any of the tested propagation methods can be safely used. However, the propagation method must be chosen carefully if accurate results for wave direction are needed, especially when the bathymetry is alongshore-variable. The most reliable way to propagate the wave conditions is by forcing a spectral model (such as SWAN) with measured 2D spectra as boundary conditions. Although it can be complicated to obtain and handle the 2D spectra, this is the only method in which the errors were below 10° for all wave climates. This accuracy in wave direction can be of crucial importance to determine if a site is prone to suffer from high angle wave instability and the formation of shoreline sand waves (Ashton et al., 2001; Arriaga et al., 2018) or whether crescentic or transverse bars will develop or straighten (Calvete et al., 2005;

Price and Ruessink, 2011; Ribas et al., 2012). The peak direction θ_{peak} is the only parameter that was not well reproduced (by any method), so it is discouraged to use this parameter in nearshore studies.

When 2D spectra are not available, the most ideal situation would be to construct a 2D spectrum out of multiple sets of integrated wave parameters (e.g., separate wind-sea and swell components). Unfortunately, this is often not possible because integrated wave parameters are typically only provided for the entire spectrum. The next option is to force a spectral wave model with 2D spectra constructed out of a single set of integrated wave parameters or use the integrated wave parameters directly in a simple wave ray model. Compared with forcing with the full 2D spectra, these methods yielded the same accuracy for wave height and mean period, but wave direction was only well-reproduced for cases characterized by limited refraction and parallel depth contours. As soon as the wave climate was bimodal or the waves refracted strongly, the errors in θ_{mean} increased substantially. Although these two methods have the advantage to be much easier to use, the errors in wave angle can be too large to correctly characterize the dominant processes. The underestimation of wave refraction is stronger in the simple wave ray model, which sometimes can not even account for all waves (in case of changes in the orientation of the shoreline). In general, it is highly recommended to validate the propagation results for wave direction with measurements before using such simpler methods. Nevertheless, it should be pointed out that for the case studied here, the effect of incorporating physical processes (like whitecapping and quadruplets) in spectral models was negligible (see Section 3.3.4.2). This indicates that conditions were favourable for applying the simple wave ray model and its shortcomings compared to spectral models are expected to become even more evident in more complex phenomenological frameworks. Results for wave ray tracing can be improved by using more advanced wave ray models that can be forced with multiple sets of integrated wave parameters, take into account alongshore-variable bathymetry and include some representation of shallow water processes.

Finally, the location of wave buoys can also cause measurement problems. Wave buoys are often deployed near harbour entrances, meaning that they are often located in water depths of less than 30 m. As a result, the measurements are affected by shallow water processes (shoaling, wave breaking and friction), whilst also the close proximity of harbour constructions like breakwaters can render the data useless for accurately describing the offshore wave climate. Furthermore, wave buoys can be sheltered from certain wave directions due to changes in the orientation of the shoreline. For example, the Barcelona wave buoy used in this study is sheltered for the rare waves coming from the west-southwest, whilst they can freely arrive at Castelldefels. In this sense, having information from a second buoy located in the southern part of the domain would be ideal.

3.5 Conclusions

The accuracy of different methodologies to obtain directional wave characteristics for nearshore field studies was tested for various wave climates at a beach located on a limited-fetch, complex-geometry sea. Such verification of wave propagation methods at the location of interest turned out to be crucial regarding wave direction. Global hindcast models with spatial resolutions of 10 km or more cannot be expected to represent the coastal zone and this also showed up in this study, meaning that their results must be interpreted with care. The trends in wave height and mean period were correctly predicted, but the errors in wave

direction for shore-oblique waves were large (*RMSE* above 60°), so that hindcast models are not suited for studies of nearshore processes that depend on wave direction.

Better accuracy can be obtained by propagating wave conditions measured at offshore buoys, although the propagation method must be chosen carefully. A simple wave ray model based on linear wave theory that assumes monochromatic waves as boundary conditions and alongshore-uniform bathymetry provided good results regarding wave height and period. However, the crude model assumptions caused the model to underestimate refraction of oblique waves over an alongshore-variable bathymetry, which led to large errors in wave direction (*RMSE* above 30°) for easterly and bimodal wave climates.

The results for these wave climates can be improved by propagating waves using a properly scaled, third-generation wave model like SWAN. As offshore boundary condition, such models require a full 2D spectrum, and one option is to reconstruct it out of a single set of integrated wave parameters. When applying this method, the results for wave direction during shore-oblique waves and bimodal wave climates improved, although the *RMSE* was still above 20°. The other option is to directly prescribe a measured 2D spectrum, which gave the best results for wave direction and reduced the *RMSE* to values below 10° for all wave climates. Such accuracy in wave direction is essential in many nearshore studies, particularly when studying the evolution of crescentic bars, transverse bars and shoreline sand waves.

During the short sampling period of this study, the SWAN results were robust to changes in model settings. Using simple settings was sufficient and including physical processes like wind, quadruplets or whitecapping did not improve the results. This confirms that wave refraction was the dominant process modifying the offshore waves over the alongshore-variable bathymetry to the nearshore study site. Under such circumstances, the use of spectral boundary conditions is highly important and observed offshore 2D wave spectra can be extremely useful to obtain accurate results of the nearshore wave field using wave propagation models.

Chapter 4 | The role of bathymetric configuration and directional wave conditions on observed crescentic bar dynamics

Abstract

Nearshore sandbars are important features in the surf zone of many beaches because they strongly influence the mean circulation and the evolving morphology. Due to variations in wave conditions, sandbars can experience cross-shore migration and vary in shape from alongshore-uniform (shore-parallel) to alongshore rhythmic (crescentic). Sandbar dynamics have been studied extensively, but existing observational studies usually do not quantify the processes leading to crescentic bar formation and straightening. This study analyses the dynamics of crescentic bar events at the fetch-limited beach of Castelldefels (northwestern Mediterranean Sea, Spain) using 7.5 years of hourly time-exposure video images and detailed wave conditions. The results show that, despite the generally calm wave conditions, the sandbars were very dynamic in the cross-shore and longshore directions. They often migrated rapidly offshore during storms (up to 70 m in one day) and more slowly onshore during post-storm conditions. Crescentic bars were often present at the study site (48% of the time), but only when the sandbar was at least 10 m from the shoreline. They displayed a large variability in wavelengths (100–700 m), alongshore migration speeds (0–50 m/day) and cross-shore amplitudes (5–20 m). Wavelengths increased for larger bar-shoreline distances and the alongshore migration speeds were strongly correlated to the alongshore transport of cross-shore momentum (radiation stress S_{xy}). Crescentic patterns typically developed during low-medium energetic waves with limited obliquity ($\theta \lesssim 20°$ at 10-m depth), whilst bar straightening occurred during medium-high energetic waves with strong oblique angles of incidence ($\theta \gtrsim 15°$). Overall, this study provides further proof for the important role of wave direction in crescentic bar dynamics and highlights the strong dependence of crescentic bar development on the initial bathymetric configuration.

Based on:

De Swart, R. L., F. Ribas, G. Simarro, J. Guillén, and D. Calvete (2021). The role of bathymetry and directional wave conditions on observed crescentic bar dynamics. *Earth Surface Processes and Landforms* 46.15, pp. 3252–3270. doi:10.1002/esp.5233.

4.1 Introduction

The nearshore zone of sandy dissipative beaches commonly features one or more shallow submerged sandbars. These sandbars are typically dynamic and display a variety of complex morphological patterns in response to variations in hydrodynamics and sediment transport. Two common patterns are shore-parallel and crescentic sandbars (sometimes called rip-channel systems), the latter consisting of an alongshore rhythmic pattern of undulations with shoreward horns (shallow areas) and seaward bays (deeper regions; e.g., Van Enckevort et al., 2004; Ribas et al., 2015, and references therein). Such alongshore rhythmic patterns can cause significant beach erosion and accretion (e.g., Castelle et al., 2015) and the currents related to these patterns (e.g., rip currents) are highly relevant for beach safety and pollutant dispersion (Dalrymple et al., 2011; Castelle et al., 2016).

Sandbar variability has attracted the attention from nearshore scientists for decades. The development of a method to track the location of sandbars based on the wave breaking pattern in time-exposure video images (Lippmann and Holman, 1989; Holman and Stanley, 2007) resulted in a large number of studies investigating their dynamics (e.g., Lippmann and Holman, 1990; Van Enckevort et al., 2004; Price and Ruessink, 2011; Bouvier et al., 2017; Rutten et al., 2018), whilst other studies continued using long-term bathymetric datasets (e.g., Castelle et al., 2007; Arifin and Kennedy, 2011; Aleman et al., 2015; Gijsman et al., 2021). This resulted in relatively good knowledge regarding the processes behind onshore and offshore sandbar migration (e.g., Gallagher et al., 1998; Ruessink et al., 2009; Aleman et al., 2017), and the discovery of monthly-annual sandbar cycles of formation near the shore, net offshore migration and seaward degeneration (NOM pattern; Ruessink and Kroon, 1994; Shand et al., 1999). The alongshore variability of sandbars was investigated by many other studies (e.g., Wright and Short, 1984; Van Enckevort et al., 2004; Almar et al., 2010; Price and Ruessink, 2011), which generally observed crescentic bars to develop during post-storm wave conditions with angles close to shore-normal and to disappear during higher energetic wave conditions (e.g., Wright and Short, 1984) or more oblique angles of incidence driving a strong alongshore current (Price and Ruessink, 2011; Contardo and Symonds, 2015). The different stages of the sandbar evolution at weekly time scales were summarized in a widely accepted beach state classification scheme (Wright and Short, 1984; Lippmann and Holman, 1990), which was later on extended to double-barred beaches (Short and Aagaard, 1993; Price and Ruessink, 2011). Previous studies also found a large variety in crescentic bar characteristics, with average wavelengths varying from 100 m to several km and average cross-shore amplitudes (defined as half the cross-shore distance between successive horns and bays) varying from 5 to 50 m (e.g., Van Enckevort et al., 2004; Arifin and Kennedy, 2011; Athanasiou et al., 2018). Furthermore, crescentic bar patterns were found to migrate alongshore at rates up to 100 m/day, presumably due to strong alongshore currents (Ruessink et al., 2000; Van Enckevort et al., 2004; Holman et al., 2006; Orzech et al., 2010).

Crescentic bars were also studied extensively using morphodynamic models, which were able to successfully reproduce some of the characteristics of crescentic bars observed in the field. For example, crescentic bar formation for shore-normal waves (e.g., Deigaard et al., 1999; Reniers et al., 2004; Calvete et al., 2005; Garnier et al., 2008; Smit et al., 2008; Castelle and Ruessink, 2011) as well as bar straightening during obliquely incident waves (Garnier et al., 2013) were successfully simulated. Models also predict that crescentic bar formation is strongly related to the underlying bathymetry (Calvete et al., 2007; Tiessen et al., 2011; Smit

et al., 2012). However, model predictions are not always in line with field observations and model validation is in general difficult due to lack of suitable field data.

The roles of wave direction and bathymetric configuration in crescentic bar formation/straightening are not yet clear, mainly because the available observation studies do not usually quantify the formation/straightening moments. Apart from that, existing observational studies on crescentic bars are often limited in duration (e.g., Van Enckevort et al., 2004) or temporal resolution (e.g., Athanasiou et al., 2018). Moreover, they generally focus on beaches that are either characterized by significant tidal range (> 1 m) and highly-energetic (H_{mo} > 1 m) waves (Van Enckevort et al., 2004; Holman et al., 2006; Price and Ruessink, 2011) or a long fetch (e.g., Contardo and Symonds, 2015). Furthermore, crescentic bar studies in low-energetic environments with almost no tides and small fetches (such as the Mediterranean Sea) are scarce. Mediterranean studies include Israel (Goldsmith et al., 1982), Italy (Armaroli and Ciavola, 2011; Parlagreco et al., 2019), Spain (Ojeda et al., 2011) and France (King and Williams, 1949; Gervais et al., 2012; Bouvier et al., 2017), with Ribas et al. (2017) providing an overview of sandbar studies in the Western Mediterranean. Unfortunately, most of these studies examine relatively short time spans and do not study the crescentic bar dynamics in detail.

The main objective of the present study is to quantify the role of directional wave conditions and the bathymetric configuration on crescentic bar development and straightening. This will be done using a dataset of nearly 8 years of hourly video images and optimal hourly wave conditions at the open, low-energetic, tideless beach of Castelldefels (northwestern Mediterranean Sea, Catalunya, Spain). The study site and datasets have already been extensively described in Chapter 2. The data analysis methods are described in Section 4.2. Subsequently, the results of quantifying the crescentic bar events and correlating them to the wave and morphological conditions are presented (Section 4.3), paying special attention to the formation and straightening moments. The main findings of this study are compared in the discussion with previous observations and model studies (Section 4.4). Lastly, the most important outcomes are listed in the conclusions (Section 4.5).

4.2 Methods

4.2.1 Visual analysis and data collection

This study uses a dataset of nearly 8-years (5 October 2010 to 31 August 2018) of time-exposure planview images. An extensive description of this dataset can be found in Section 2.3 of Chapter 2.

A visual analysis of daily planview images (at 12:00 midday) was first carried out separately by two experienced researchers in order to reduce subjectivity. The occurrence of crescentic bar events in the sandbars was tracked, including dates of formation and straightening. Subsequently, both analyses were compared and the inconsistencies in crescentic bar presence (only 4% of the time) were cross-checked in order to increase accuracy and obtain the final visual analysis. Normally, a crescentic bar event was defined when at least three clear undulations with a certain rhythmicity occupied at least half of the planview images for at least two days. Crescentic patterns with two undulations were also considered if the wavelength was too large for more undulations to fit in the planview domain. One-day events were considered in case a clear rhythmic pattern occurred in the entire planview domain. An event was

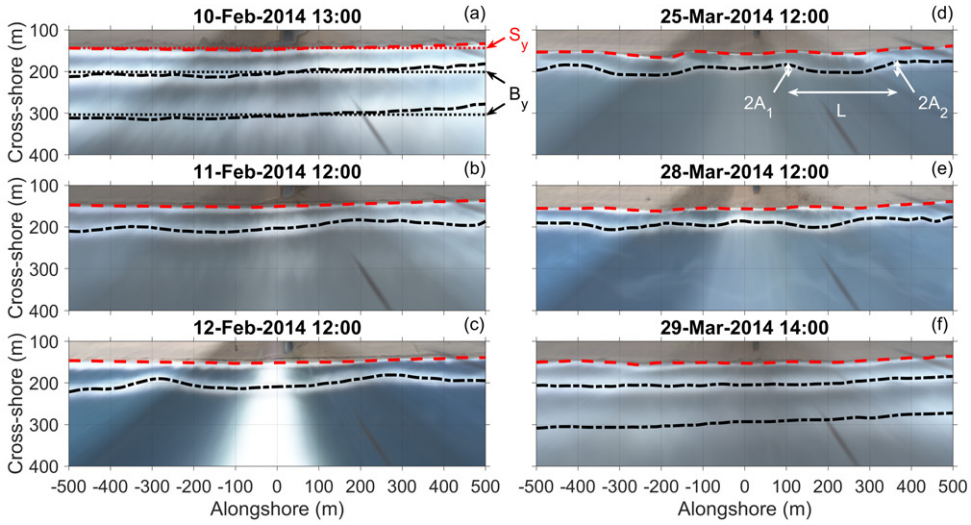

Figure 4.1 Planview images of Castelldefels beach showing the formation (a-c), development (d) and straightening (e-f) of a crescentic bar event. The tracked barlines $B(y)$ and shorelines $S(y)$ are plotted in all planviews. Furthermore, (a) also shows the alongshore-averaged bar- and shoreline positions B_y and S_y, whereas (c) shows an example of sun glare in the planview and (d) shows examples of wavelength L and the double amplitudes $2A_1$ and $2A_2$ (the amplitude A is defined as $A = \frac{A_1+A_2}{2}$).

assumed to continue during an image gap when the crescentic bar pattern in the first image after the gap was similar to that in the last image before the gap. Special attention was paid to detecting the formation and straightening moments of the crescentic bar events (Figure 4.1). A formation moment (Figure 4.1b) was defined as the first day where, following a period with alongshore-uniformity, a crescentic pattern occurred in the planview images. Planview images in which the bar rhythmicity was strengthened (e.g., a clear increase in amplitude) were classified as reinforcement moments and included in the dataset with formation moments. A straightening moment (Figure 4.1f) was the first day where, following a period with crescentic bars, the bar was again alongshore-uniform. Planview images in which the bar rhythmicity was weakened (e.g., a clear decrease in amplitude) but the crescentic pattern persisted (same rip locations, identical wavelengths) were classified as partial straightening moments and included in the dataset with straightening moments. A separation was made between unclear formation/straightening moments (e.g., no images available) and clear formation/straightening moments.

Hourly shorelines were extracted from all planview images using the uShore software (Ribas et al., 2020). This methodology combines the shorelines detected with four standard procedures to produce an accurate shoreline, with cross-shore errors below 2.5 m at this site. The default settings recommended in Ribas et al. (2020) were used, except for those related with the space-time filtering of the final shoreline. Here, no time filtering was applied and a 20 m window was used for the moving average in space. Subsequently, a visual evaluation of the shorelines was conducted to pick the best shoreline per day. For the 145 days on which the uShore software did not provide a shoreline of sufficient quality, the shoreline was man-

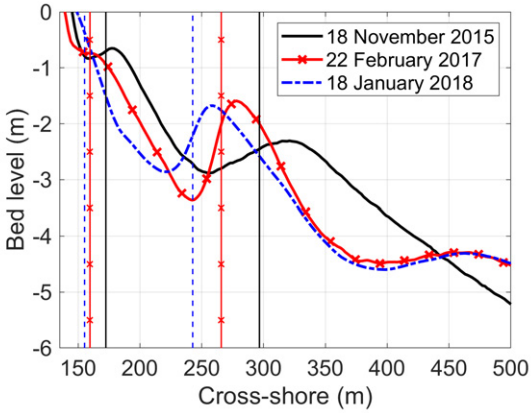

Figure 4.2 Measured alongshore-averaged cross-shore profiles at Castelldefels beach on 18 November 2015 (inner bar), 22 February 2017 (inner terrace) and 18 January 2018 (no inner bar/terrace). The vertical lines indicate the alongshore-averaged barline positions derived from the time-exposure images closest to the bathymetry dates.

ually digitized using the best-quality planview image. In total, shorelines were obtained for all days with camera images (2664 images in total, see examples in Figure 4.1).

The BarLine Intensity Mapper (BLIM; Pape, 2008) was used to track the breaker lines (from now on called barlines) in the planview images. This algorithm (Van Enckevort and Ruessink, 2001) detects the cross-shore location of the maximum breaker intensity value for each alongshore location. However, the barlines obtained from BLIM and the real bar crest locations are normally not identical, due to changes in water level, offshore wave height and the underlying sandbar geometry (Van Enckevort and Ruessink, 2001; Ribas et al., 2010). At the study site, the cross-shore distance between real and videoed alongshore-averaged barlines for the outer bar (using the 9 topo-bathymetric surveys) was on average 16 m, with the videoed barlines located shoreward of the real barlines (see examples in Figure 4.2). Comparable results were obtained at two nearby single-barred beaches by Ribas et al. (2010). For the inner bar, the difference between real and videoed alongshore-averaged barlines (computed for the only 2 topo-bathymetric surveys with measured inner bar or terrace) was much smaller (5 and 6 m, respectively; Figure 4.2), presumably because the outer bar filters out the larger waves before they reach the inner bar (tidal action is negligible at the study site). Prior to tracking the barlines, a visual quality assessment of all planview images was performed to select, for each day, the image with better quality (foam presence, minimum sun glare, good contrast). Generally, the images around midday were selected because the sun is highest in the sky (minimising sun glare). One image per day was usually enough for tracking the barlines, but up to three images per day were used when fast changes in the wave breaking pattern occurred within one day. Days without a clear wave breaking pattern in the images or that only contained low-quality images were removed from the analysis. In total, barlines were extracted from 2279 images (2208 days) using BLIM (see examples in Figure 4.1).

4.2.2 Bar and shoreline characterization

For each BLIM image, the cross-shore bar crest positions B at time t and alongshore position y were stored in a matrix $B(t, y)$ and the corresponding shoreline positions S were stored in a matrix denoted $S(t, y)$. Time series of the alongshore-averaged bar crest positions $B_y(t)$ and alongshore-averaged shoreline positions $S_y(t)$ were also obtained (Figure 4.1a). The alongshore-averaged distance between the sandbars and shorelines $D_y(t)$ was computed by subtracting $S_y(t)$ from $B_y(t)$. Finally, the sinuosity $Sin_B(t)$ of the bar crest positions was also computed (total bar length divided by the distance between first and last point; Ojeda et al., 2011). In the barlines corresponding to a crescentic bar, all bays and horns were detected under the conditions that the cross-shore distance between a successive bay and horn was at least 6 m and the alongshore distance did not exceed 500 m. These constraints were enforced to prevent the detection of small (typically short-lived) wobbles as crescentic bars and to ensure that at least one complete undulation (consisting of two horns and one bay) was present in the planview domain. Following Van Enckevort et al. (2004), the wavelength L was computed for each undulation as the alongshore distance between the horns and the amplitude A was computed as half the average cross-shore distance between the bay and the two adjacent horns (Figure 4.1d). Within the same barline, the variation in A was mostly small (average standard deviation of 2 m), whilst L typically showed more variation (average standard deviation of 65 m). For each barline, L and A were averaged over all undulations to obtain the alongshore-averaged wavelengths and amplitudes L_y and A_y.

Finally, alongshore migration rates were obtained during crescentic bar presence by comparing barlines using cross-correlation. For each barline that is part of a crescentic bar event, the shifted barlines (see example in Figure 4.3) dating between 2 and 4 days after the original barline were identified (under the condition that the original and shifted barlines belonged to the same crescentic bar event). Subsequently, all shifted barlines were separately cross-

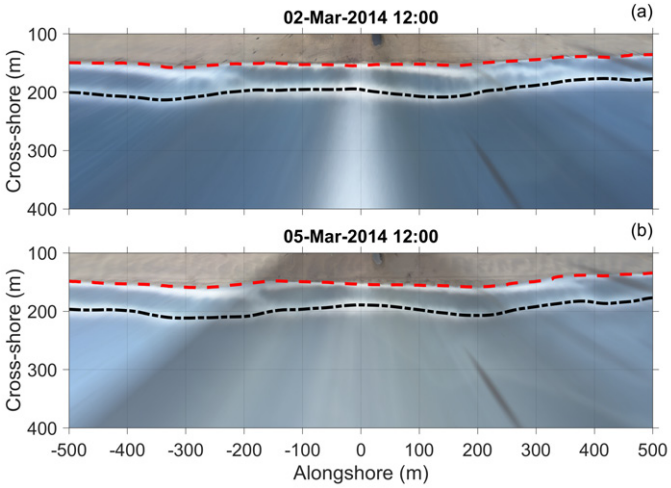

Figure 4.3 Planview images of Castelldefels beach at (a) 2 March 2014 12:00 and (b) 5 March 2014 12:00 (3 days apart), with the tracked inner barline and shoreline plotted in both images. An alongshore eastward migration of approximately 60 m is visible in the crescentic pattern of the inner barline, amounting to a migration rate of approximately 20 m/day.

correlated to the original barline. The alongshore migrated distance of the crescentic pattern is given by the magnitude of the lag at the positive peak that is located nearest to the origin of the cross-correlogram. The sign of the lag indicates the migration direction (positive for eastward migration). A minimum normalized correlation of 0.7 was imposed. To obtain the migration velocity C_y, the migrated distance is divided by the time difference between the two correlated barlines.

4.2.3 Waves

Hourly wave conditions were obtained from the Barcelona wave buoy (Figure 2.1), which provides full 2D frequency-direction spectra as well as integrated wave parameters (see Section 2.4.2 for more details). Following the findings of Chapter 3, the measured wave conditions were propagated to 10 m depth in front of the study site using SWAN. The SWAN output data includes integrated wave parameters as well as the 2D frequency-direction spectra. Two types of SWAN simulations were done: one used the measured 2D spectra as offshore boundary conditions, whilst the other was forced with the measured integrated wave parameters. Since forcing SWAN with 2D spectra yields the best results at the point of interest (particularly regarding θ_{mean} and the 2D spectra; see Chapter 3), the simulation forced with integrated wave parameters is only used (with illustrative purposes) to complement the simulation forced with 2D spectra at the moments when the latter were not available (2.8% of the time).

Hourly wave conditions were taken from the SWAN output point located at 10-m depth in front of the study site (Figure 2.1). For each barline, the wave conditions in the 24 hours prior to midday on the day of the barline were kept. Barlines for which wave conditions were unavailable more than 75% of the time or $H_{m0} < 0.2$ m were not included in the analysis. Data from the simulation forced with integrated wave parameters was used in presenting the dataset for illustrative purposes (grey data in Figures 4.4a-c and 4.6f) but not included in the analysis of the barlines because the wave angle is unreliable (see Chapter 3). The analysis is thus fully based on SWAN simulations forced by 2D spectra. Wave angles were taken with respect to the shore-normal using a constant coastline orientation of 89° with respect to North. The boundary in wave angle to discriminate between easterly and westerly waves was set at −5° with respect to shore-normal (negative angle indicates east). This adjustment was made because the propagated easterly waves had a negative bias in wave direction of −7.5°, whilst the westerly waves had a positive bias of 2.3° (Chapter 3). The alongshore transport of cross-shore momentum (radiation stress S_{xy}) was computed using the wave conditions as: $S_{xy} = \frac{c_g}{c} \cos\theta \sin\theta \frac{1}{8} \rho g H_{rms}^2$ (Holthuijsen, 2007), where c_g is the group velocity, c is the phase velocity, θ is the wave angle with respect to the shore-normal, ρ is the water density, g is the gravity acceleration and H_{rms} is the root-mean-square wave height ($H_{rms} = \frac{H_{m0}}{\sqrt{2}}$). Storms were detected in the measurements of the Barcelona buoy following the criteria set by Ojeda and Guillén (2008), where a storm was defined as a period of at least 12 hours during which H_{m0} exceeded 1.5 m and the peak H_{m0} exceeded 2.5 m. In case the time between two storms was less than 6 hours, it was considered a single double-peaked storm.

4.3 Results

4.3.1 Alongshore-averaged barline and shoreline positions

A total of 6 sandbars (always two at the same moment in time) were tracked during the study period (Figure 4.4d-e). It was decided to treat the sandbars after the gap without images (October 2016 – January 2017) separately and not link them to the sandbars before the data gap because several storms occurred during this period (Figure 4.4a), meaning that the real amount of studied sandbars might be less than 6. The cross-shore position of the shoreline during the entire period was mostly around 150 m, although it could vary between 130 and 170 m (Figure 4.4d). During the study period, the shoreline retreated on average by approximately 8 m. The cross-shore positions of the sandbars showed much more variability with rapid offshore migration during storms and slower onshore movement during post-storm conditions (Figure 4.4d). The formation of a new sandbar at the shoreline was observed twice (in February 2011 and March 2015) and two episodes of bar disappearance also occurred (in March-April 2011 and March 2015).

Major changes in the average cross-shore sandbar positions were always related to high-energetic wave conditions. Very fast offshore migration (70 m in 1 day) was observed in March 2013 and March 2015. Figure 4.5 shows 8 planview images during the formation of sandbar 3 in March 2015, supporting our interpretation that the inner sandbar 2 migrated 100 m offshore between 19 and 21 March (blue line in the figure below). At first, the sandbar migrated offshore at a relatively small rate of 25 m/day (from 19 to 20 March) and then at a large rate of over 70 m/day (from 20 to 21 March). An important clue is that no outer bar (which would be sandbar 1) is visible on the planview of 20 March (the wave height at this day was such that waves would break on the outer bar if it was present), which supports our interpretation that the outer bar on 21 March is indeed sandbar 2. At the same time, the incipient terrace/bar that formed from 19 to 20 March (black line) migrated offshore from 20 to 21 March and became sandbar 3 by occupying the space left by the previous inner bar. Based on these images, we think that our interpretation of a fast offshore migration of 70 m/day in this event is justified and that it is unlikely that no fast offshore migration occurred (this would imply an unrealistic onshore migration of sandbar 2 from 20 to 21 March during a strong storm). Furthermore, an offshore migration rate of 70 m/day was also observed at this site in March 2013. Finally, several other moments with large migration rates (up to 40 m/day) were detected during the study period of 7.5 years, confirming that the event in March 2015 is not a unique occurrence.

Other cases of fast offshore migration (up to 40 m/day) were observed in November 2010, January 2011, April 2011, November 2011, March 2012, October 2012, December 2013 and January 2016 (Figure 4.4d). In April 2011 and March 2015, the original inner bar migrated offshore and became the new outer bar (sandbar 1 and sandbar 2, respectively). This in turn allowed for a new or recently formed sandbar (sandbar 2 and sandbar 3, respectively) to occupy the location left by the migrated original inner bar. Moreover, the original outer bar (first outer bar and sandbar 1, respectively) moved further offshore (outside the planview domain), so that waves did no longer break on them and they probably slowly diffused (as reported at other coasts by Ruessink and Kroon, 1994; Shand et al., 1999). Note also that the remnants of a previous outer bar are visible at deeper water in two of the profiles in Figure 4.2 (around cross-shore coordinate 480 m).

4.3.2 Crescentic bar occurrence

A total of 98 crescentic bar events were observed in the study period (Table 4.1), of which 96 occurred in the inner bar and 2 in the outer bar. In total, crescentic bars were present during 48% of the time (1389 days). No seasonal signal is present in the occurrence of crescentic bars, but there is a clear uneven distribution in presence over the different years (Figures 4.4f

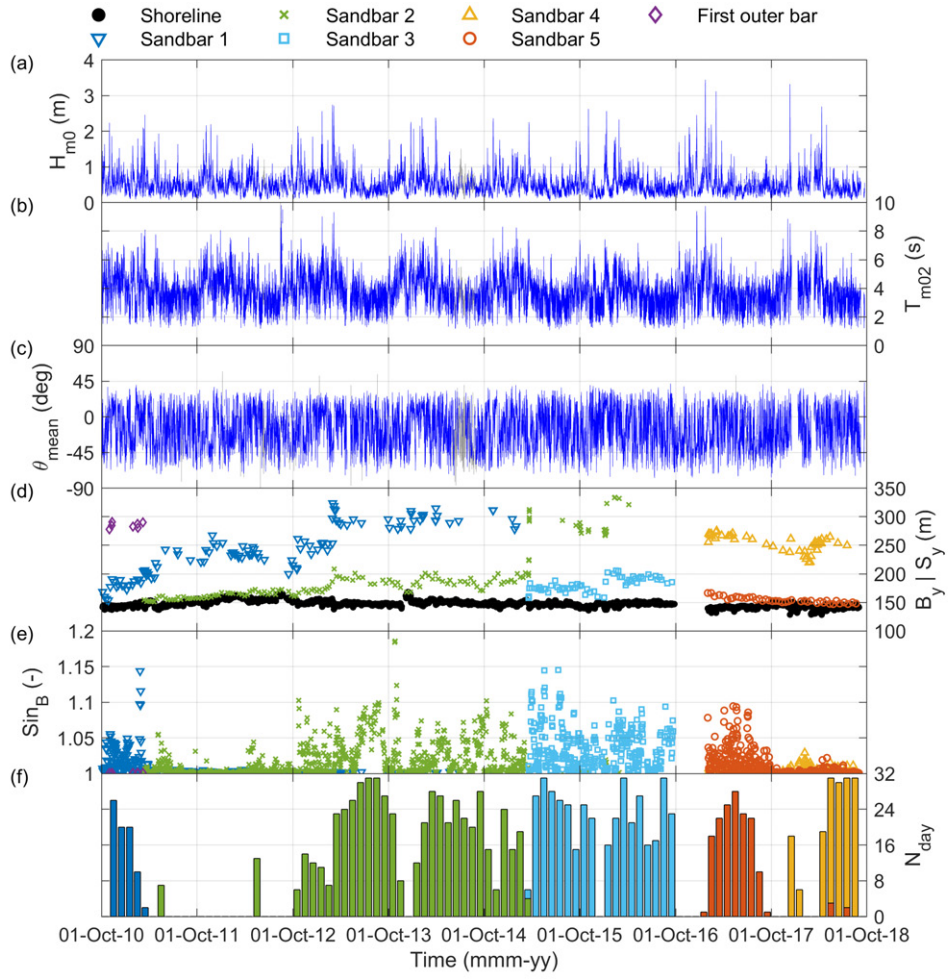

Figure 4.4 The (a) significant wave height H_{mo}, (b) mean period T_{mo2}, (c) mean wave direction θ_{mean} from shore normal (positive for westerly waves), (d) alongshore-averaged bar crest and shoreline positions B_y and S_y, (e) sinuosity of the barlines Sin_B and (f) number of days per month with crescentic bars N_{day} versus time at Castelldefels beach. Panels (a), (b) and (c) display all hourly wave conditions at 10 m depth in front of the study site (no threshold in H_{mo}) and the colours denote the SWAN boundary conditions: 2D spectra (blue) or integrated wave parameters (grey). To increase readability, only a selection of data points of sandbars 1-5 are shown in panel (d). In case crescentic bars occurred in two different sandbars during the same month (e.g., May and July 2018), the bar with the least amount of days with crescentic bars is shown at the front in panel (f).

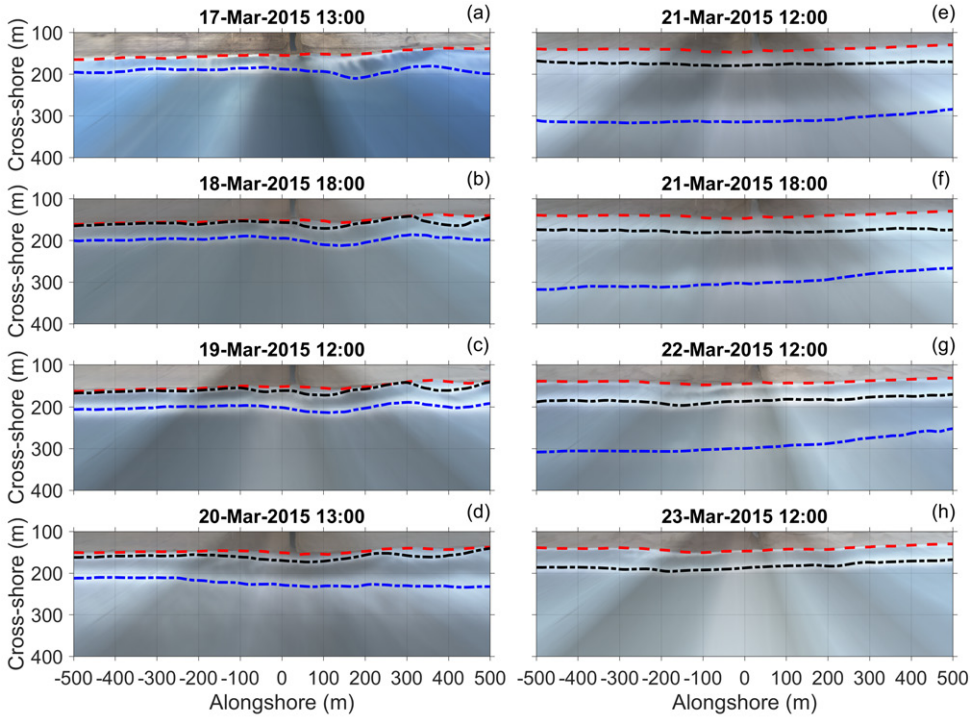

Figure 4.5 Planview images in March 2015 showing the formation of a new inner sandbar (a-d), fast offshore migration (70 m in one day) of the original inner sandbar (d-f) and the subsequent new sandbar situation (g-h). The tracked barlines (blue for the original inner bar, black for the new inner bar) and shoreline (red) are plotted in all images.

and 4.6a). Crescentic bars were often present during 2013–2017, whilst in 2011–2012 there were long periods without any crescentic bar (Table 4.1). There are also significant differences in event duration between the different years (varying from days to months). It is important to bear in mind that crescentic bars at Castelldefels can retain their configuration for a long time during extended periods with low-energetic wave conditions. This leads to freezing of the morphological configuration (bar arrestment; Ojeda et al., 2011) until the wave energy increases. A nice example occurs in summer 2013 (Figure 4.6a).

The uneven distribution of crescentic bars over the different years turns out to be related to changes in the alongshore-averaged sandbar-shoreline distance (Figure 4.4d and 4.4f). Crescentic bars developed frequently when the sandbar was located at least a certain distance from the shoreline (10–15 m). When the sandbar was located too close to shore, it did not become crescentic. Also, nearly all crescentic bar events occurred in the inner bar, meaning that the sandbar should not be located too far from shore either. The reason is that if the bar is at deeper water, morphological changes can only occur during high-energetic wave conditions.

Table 4.1 Yearly statistics of crescentic bar occurrence and mean bar characteristics (mean absolute values for C_y) for each tracked sandbar during the entire study period. Statistics are also given for all inner and outer bar data. A crescentic bar event that occurs within two years is ranked among the year in which the event started. Years without crescentic bars in the respective sandbar are not displayed.

Sandbar	Year	Number of events	Mean duration [days]	Total duration [days]	D_y [m]	L_y [m]	A_y [m]	C_y [m/day]
Sandbar 1	2010[1]	6	11	66	32	233	9	5.6
	2011	1	12	12	64	212	13	9.8
Sandbar 2	2011	2	3.5	7	9	105	5	1.4
	2012	10	4.5	45	12	135	6	3.7
	2013	16	15	241	36	223	11	5.6
	2014	15	17	250	38	241	10	6.0
	2015	5	7.6	38	64	253	8	5.8
Sandbar 3	2015	12	17	205	28	159	8	3.6
	2016[2]	9	23	204	44	173	9	4.9
Sandbar 4	2017[3]	1	24	24	122	527	12	–
	2018[4,5]	1	142	142	110	468	14	–
Sandbar 5	2017[3]	18	8.3	150	14	167	5	1.9
	2018[4]	2	2.5	5	8	159	5	3.7
Inner bar (all)	2010–2018	96	13	1223	33	196	9	4.7
Outer bar (all)	2010–2018	2	83	166	119	475	14	–

[1] Only data for October-December 2010
[2] No data for October-December 2016
[3] No data for January 2017
[4] No data for September-December 2018
[5] Event extends beyond study period

4.3.3 Crescentic bar formation/straightening

A large number of crescentic bar formation/straightening moments occurred during the study period. Examples of planviews during formation and straightening for a characteristic crescentic bar event have already been shown in Figure 4.1. The corresponding time series of the same crescentic bar event are shown in Figure 4.7.

At the study site, crescentic bars developed in periods with relatively calm wave conditions and not very oblique angles of incidence that followed after a short period with medium-high energetic wave conditions (e.g., Figure 4.7 on 10/02/2014). As mentioned in Section 4.3.2, the sandbar should also be located at a sufficient distance from shore. As long as the wave conditions remained calm, the crescentic bars continued to grow and develop more pronounced undulations. When the wave direction became more oblique, this could lead to alongshore migration (e.g., Figure 4.7 between 19/02/2014 and 05/03/2014). The crescentic pattern was typically destroyed during storms with medium-high energetic wave conditions and strong oblique angles of incidence (e.g., Figure 4.7 on 28-29/03/2014), although sometimes bar straightening was caused by the sandbar welding to the shoreline. During really low-energetic wave conditions (hardly any breaking), no morphological changes were observed and bar arrestment occurred (e.g., between 06/03/2014 and 12/03/2014 in Figure 4.7). Crescentic bars were often accompanied by undulations at the shoreline (megacusps), which mostly developed 1–2 days after the formation of a crescentic bar but sometimes developed halfway through a long-lasting crescentic bar event (Figures 4.1d and 4.8). They typically continued to grow as long as low-energetic wave conditions persisted and mostly disappeared with crescentic bars during storms.

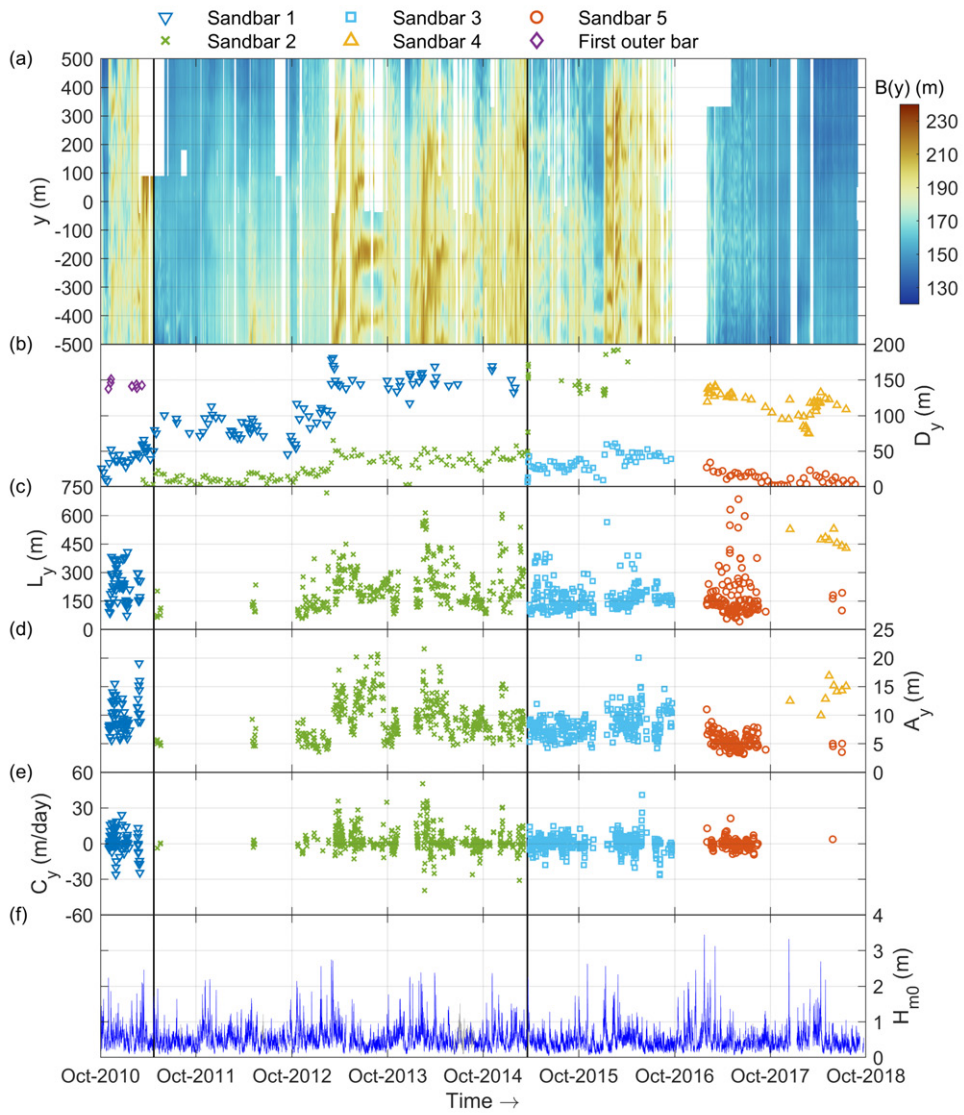

Figure 4.6 The (a) cross-shore bar crest positions (with respect to the camera tower) B at alongshore position y of the bar closest to shore (timestack), (b) alongshore-averaged sandbar-shoreline distance D_y, (c) alongshore-averaged wavelength L_y, (d) alongshore-averaged amplitude A_y, (e) average migration speed C_y (positive for eastward migration) and (f) hourly significant wave height H_{m0} (10 m depth) versus time at Castelldefels beach. The black vertical lines indicate the separation between different sandbars in panel (a). To increase readability, only a selection of data points of sandbars 1-5 are shown in panel (b). Panel (f) displays all hourly wave heights (without threshold) and the colours denote the SWAN boundary conditions: 2D spectra (blue) or integrated wave parameters (grey).

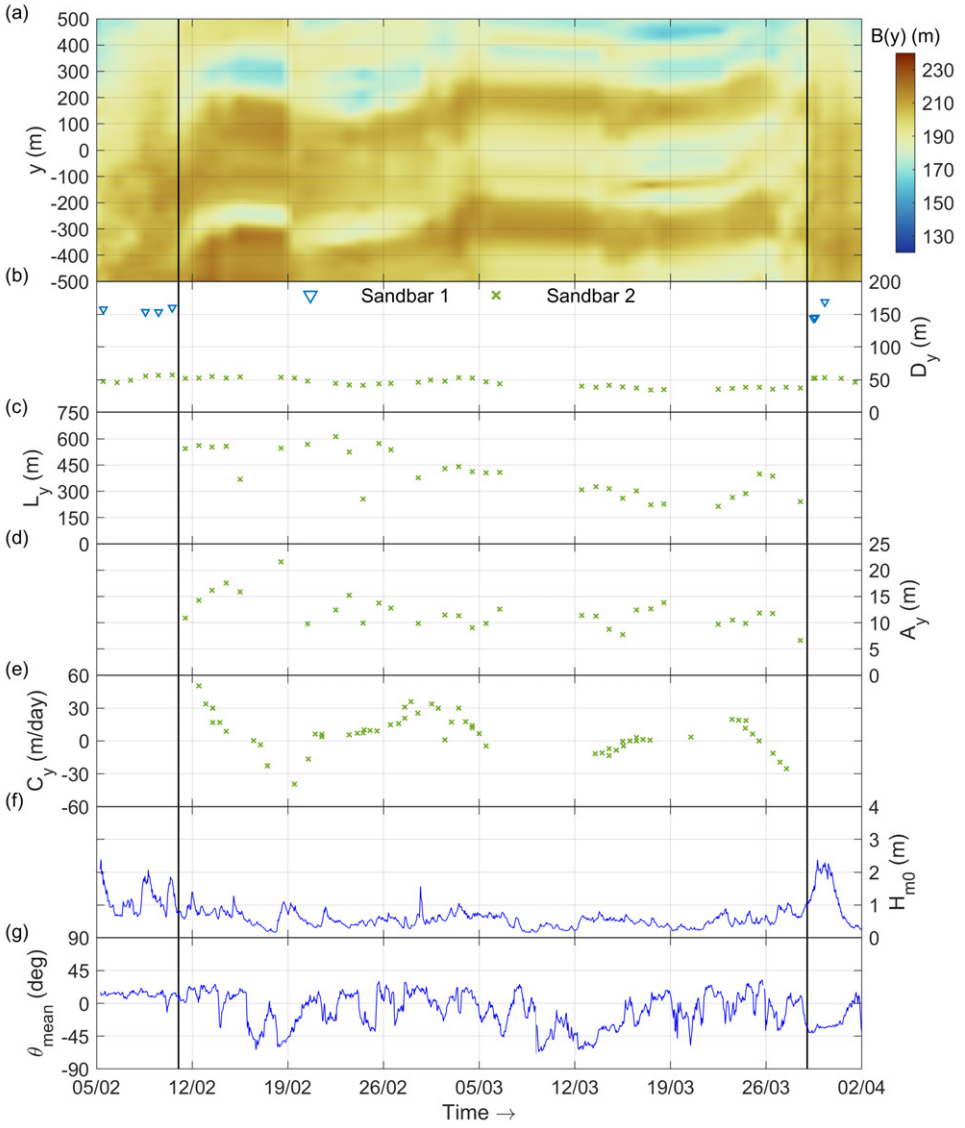

Figure 4.7 Identical to Figure 4.6, but now for one clear crescentic bar event in February-April 2014. Additionally, the mean wave direction θ_{mean} from shore normal (positive for westerly waves) at 10-m depth is added in panel (g). Panels (f) and (g) display all hourly wave conditions (no threshold in H_{mo}) and the black vertical lines indicate the start and end of the crescentic bar event.

Histograms of the wave height and wave direction are shown in Figure 4.9 for six categories: (a) the entire study period, (b) days with crescentic bar presence, (c) formation moments, (f) straightening moments, (d) days without crescentic bars and (e) days without crescentic bars but sufficient bar-shoreline distance. The bar was assumed to be located at a sufficient distance from shore for the formation of crescentic bars if D_y > 10 m, which

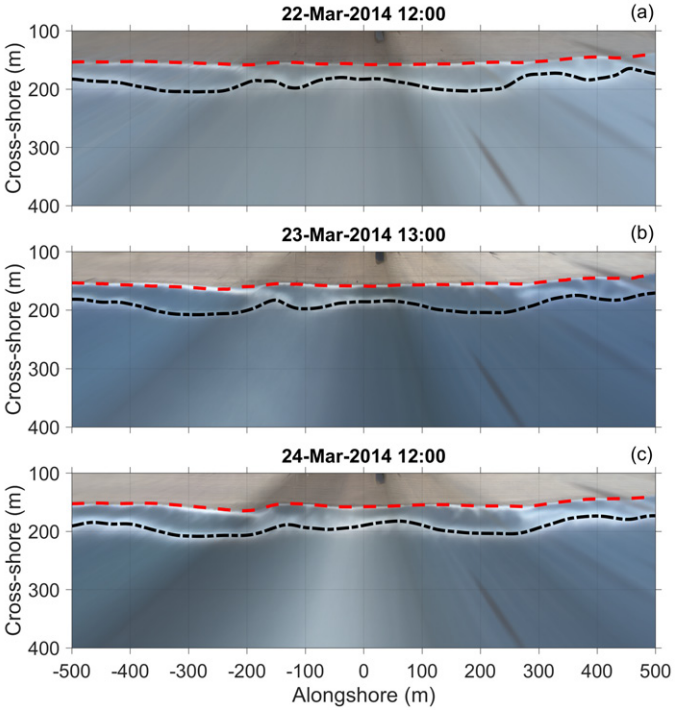

Figure 4.8 Planview images of 3 subsequent days in March 2014 showing the development of the megacusp at the shoreline shown in Figure 4.1d. The tracked inner barline and shoreline are plotted in all images.

was chosen after analysing D_y for all moments with crescentic bars. Standard deviations are indicated in Figure 4.9 with crosses located at the median. Due to the clear bimodal distributions, the statistical parameters of the wave angle in Figure 4.9d-f are computed separately for easterly and westerly waves using a boundary of $-5°$ (as justified in Section 4.2.3). Additional statistics of the wave conditions for all categories are given in Table 4.2.

Figure 4.9a and Table 4.2 again emphasize that low-medium energetic wave conditions with a large variety in wave angle dominated during the study period. Similar wave conditions dominated when no crescentic bars were present (Figure 4.9d). In contrast, high-energetic waves were completely absent during the presence of crescentic bars and the waves were slightly less oblique (Figure 4.9b). During crescentic bar formation (Figure 4.9c and Table 4.2), a little more energetic waves prevailed and the wave angles were less oblique compared to the rest of the categories. Consistently, south-southwesterly and bimodal wave climates were dominant (Figure 4.10) and east-southeasterly wave climates (generally characterised by more oblique wave directions) occurred less frequently. During crescentic bar straightening (Figure 4.9f), oblique waves were clearly dominant and shore-normal waves were rare (south-southwesterly and east-southeasterly wave climates prevailed; Figure 4.10). Furthermore, high-energetic wave conditions occurred quite frequently (particularly for southwesterly waves). Nearly identical wave conditions were seen when the bar-shoreline distance was sufficient but no crescentic bar occurred (Figure 4.9e).

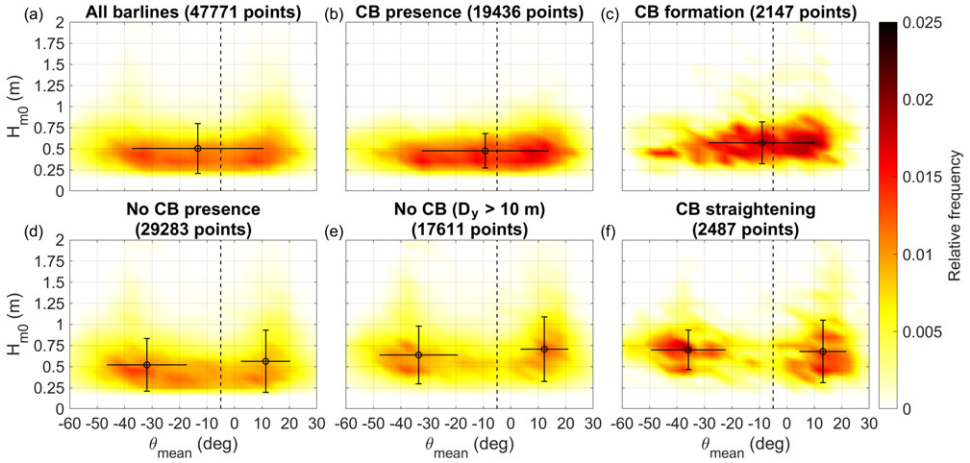

Figure 4.9 2D histograms of hourly significant wave height H_{mo} versus hourly mean wave direction θ_{mean} from shore normal (positive for westerly waves) at 10-m depth for different categories (CB denotes crescentic bar). Only data from the simulation forced with 2D spectra is shown excluding the waves with H_{mo} < 0.2 m. The error bars intersect at the median and indicate the standard deviation of both wave parameters. The dashed vertical line is the separation between easterly and westerly waves for computing the error bars/medians of θ_{mean} in panels (d), (e) and (f).

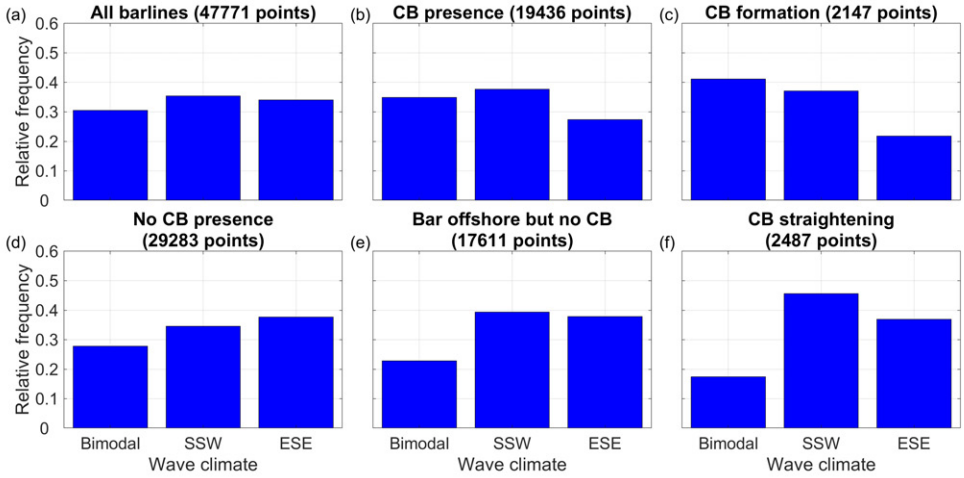

Figure 4.10 Histograms of the distribution of bimodal, south-southwesterly (SSW) and east-southeasterly (ESE) wave climates at 10-m depth in front of Castelldefels beach for different categories (CB denotes crescentic bar). Low-energetic wave conditions (H_{mo} < 0.2 m) are excluded. Wave climates were determined using the propagated 2D spectra at 10-m depth in front of Castelldefels beach, where for east-southeasterly or south-southwesterly wave climates at least 65% of the wave energy had to come from that direction. The threshold angle to discriminate between east-southeasterly and south-southwesterly wave energy was set at 165° with respect to north (mean of all wave directions).

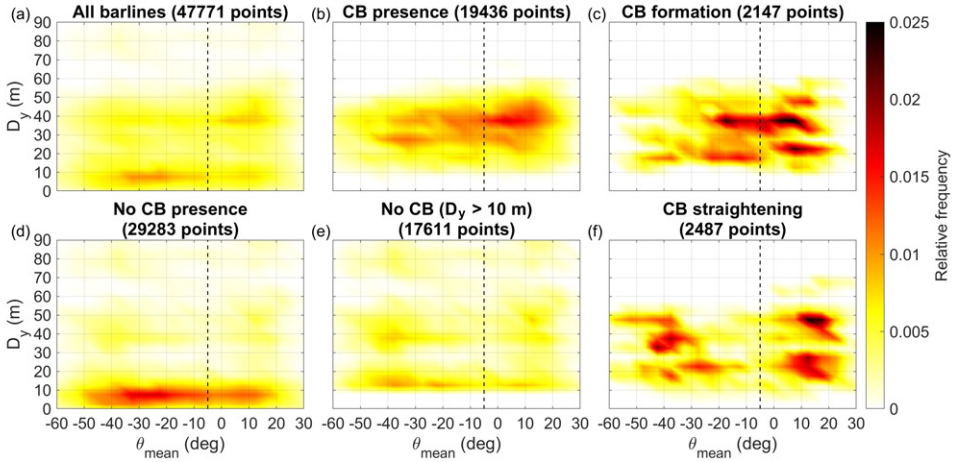

Figure 4.11 2D histograms of the average bar-shoreline distance D_y versus hourly mean wave direction θ_{mean} from shore normal (positive for westerly waves) for the same categories as in Figure 4.9. Only data from the simulation forced with 2D spectra is shown and waves with $H_{m0} < 0.2$ m are excluded.

The relation between crescentic bars occurrence and the bar-shoreline distance is further demonstrated in Figure 4.11. It is clear that crescentic bars were mostly present for bar-shoreline distances between 20 and 50 m (Figure 4.11b), whilst they were absent when the bar was located close to shore ($D_y < 10$ m; Figure 4.11d). Also when the bar was sufficiently offshore ($D_y > 10$ m) but no crescentic bar was present, the bar was generally still fairly close to the shoreline (between 10 and 20 m; Figure 4.11e). Finally, crescentic bar formation and straightening (Figures 4.11c/f) generally occurred when the bar was located between 15 and 50 from the shore (comparable to crescentic bar presence). Compared to Figure 4.11b, Figures 4.11c,f show a certain scattering, which is due to the fewer data points in those last two figures.

Table 4.2 Statistical values (mean, standard deviation) of integrated wave parameters at 10 m depth in front of Castelldefels beach for the categories in Figures 4.9 and 4.11. The final letters in the first column refer to the panels of Figures 4.9 and 4.11. Depending on the distribution in Figure 4.9, the statistics of θ_{mean} (with respect to shore-normal) have either been evaluated separately for easterly and westerly waves (with separation at -5° from shore-normal) or for all waves combined. Statistics are computed using the simulation forced with 2D spectra and excluding waves with $H_{m0} < 0.2$ m.

Category	H_{m0} [m]		T_{m02} [s]		θ_{mean} [deg]		θ_{mean} (east) [deg]		θ_{mean} (west) [deg]	
	Mean	stdev	Mean	stdev	Mean	stdev	Mean	stdev	Mean	stdev
All barlines (a)	0.57	0.29	4.0	1.1	−14	24	–	–	–	–
CB presence (b)	0.51	0.20	3.8	0.96	−12	23	–	–	–	–
CB formation (c)	0.61	0.25	4.4	0.94	−11	19	–	–	–	–
No CB presence (d)	0.62	0.34	4.2	1.2	–	–	−31	15	11	9
No CB ($D_y > 10$ m) (e)	0.74	0.36	4.5	1.2	–	–	−32	14	12	9
CB straightening (f)	0.73	0.31	4.4	1.1	–	–	−34	14	13	9

4.3.4 Crescentic bar characteristics

Crescentic bar characteristics varied a lot during the same event (Figures 4.6c-e and 4.7c-e). Substantial differences in average crescentic bar wavelengths were observed for the same sandbar between different years and also in between the various sandbars (Table 4.1). The early stages of longer-lasting (more than one week) crescentic bar events were often characterized by relatively large wavelengths (L_y above 400 m). As the crescentic bars developed further, the wavelengths often decreased (L_y below 300 m) due to splitting of individual crescents (compare the wavelength on 13/02/2014 with the wavelengths on 05/03/2014 and 18/03/2014; Figure 4.7c). At the end of the event, the wavelengths often increased again as the smaller intermediate undulations disappeared prior to the larger undulations (compare the wavelengths on 18/03/2014 and 26/03/2014; Figure 4.7c). In contrast, the wavelengths of short-term (less than one week) events were mostly quite small (L_y below 300 m) and generally quite constant throughout the entire event. The amplitudes showed a more limited variability. The early stages of a crescentic bar event were often characterized by small amplitudes (A_y in the order of 5 m), which typically increased during longer-lasting events (compare the amplitudes on 11/02/2014 and 18/02/2014; Figure 4.7d) and could reach values of 20 m. Alongshore migration speeds were typically quite small (C_y between -10 and +10 m/day) and larger migration speeds were mostly observed for more pronounced (longer-lasting) crescentic bar events with larger wavelengths and amplitudes (Figures 4.6e and 4.7e).

The large variability in wavelength is partly related to the aforementioned splitting and merging of individual crescents, but the wavelength also tends to increase with the bar-shoreline distance (Figure 4.12). Despite the scatter and the relatively low correlation coefficient, the relation is highly significant at the 99% confidence level. In agreement with the observed trend in the inner bar, constant large wavelengths were observed during the only two crescentic bar events in the outer bar (Table 4.1 and Figure 4.6c). Finally, a clear relation is present between the migration speed magnitudes and the radiation stress S_{xy} (Figure 4.13). The observed trend does not depend very much on the time period over which the migration

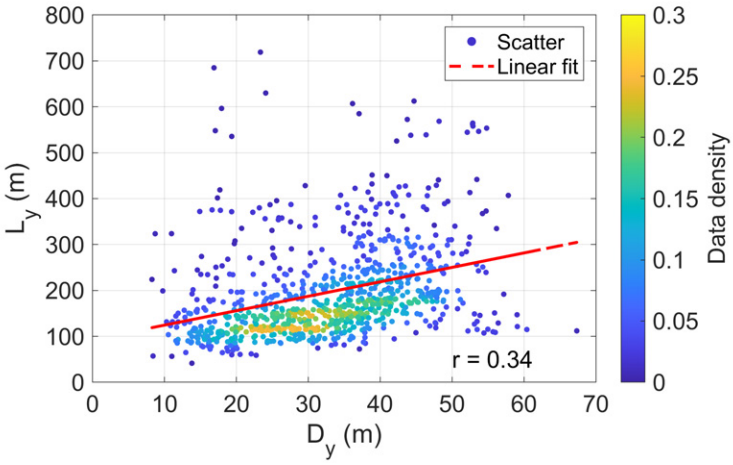

Figure 4.12 Average wavelength L_y versus average bar-shoreline distance D_y for all inner bar data including linear fit and Pearson correlation coefficient. The colours denote the data density.

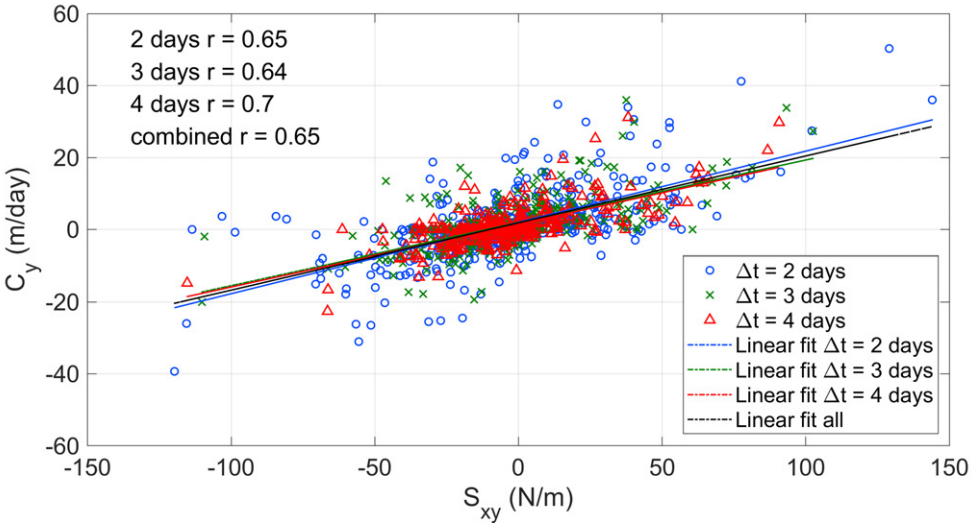

Figure 4.13 Average crescentic bar migration speed C_y (positive for eastward migration) versus radiation stress S_{xy} (positive for waves coming from the west). Linear fits and the corresponding Pearson correlation coefficients are also included. The different colours indicate the time period over which the migration speed was computed. For each migration speed, S_{xy} was averaged over the corresponding time period. When computing S_{xy}, the bias in wave direction was compensated by adding 5° to the wave angles (see Section 4.2.3).

speeds were computed (as explained in Section 4.2.2) since similar linear fits and correlation coefficients were found for the different time periods and all relations are highly significant at the 99% confidence level.

4.4 Discussion

4.4.1 Accuracy of crescentic bar detection

Crescentic bar events and specifically the formation/straightening moments were detected visually in this study (analogous to Holman et al., 2006) by two experienced researchers to prevent bias and increase accuracy. However, previous studies on crescentic bars often employed an automatic algorithm using either the standard deviation of the detrended barline (σ_B, e.g., Price and Ruessink, 2011; Contardo and Symonds, 2015) or the sinuosity of the barline (Sin_B, Ojeda et al., 2011). In order to test the reliability of these two parameters, the values of σ_B and Sin_B at Castelldefels were plotted for the moments with and without visually detected crescentic bars (Figure 4.14). Clearly, Sin_B works better as a proxy for crescentic bar presence (e.g., $Sin_B \gtrsim 1.01$) than σ_B, but there is still a substantial range in Sin_B for which this parameter is inconclusive. In particular, crescentic bars could be present for Sin_B = 1.005–1.01 and not exist for Sin_B = 1.01–1.02. Since Sin_B does not discriminate well enough, it was decided to use the visual analysis to obtain maximum accuracy.

Visual detection of straightening moments was generally quite clear because they mostly occurred within one day. Detecting formation moments was more challenging, since they

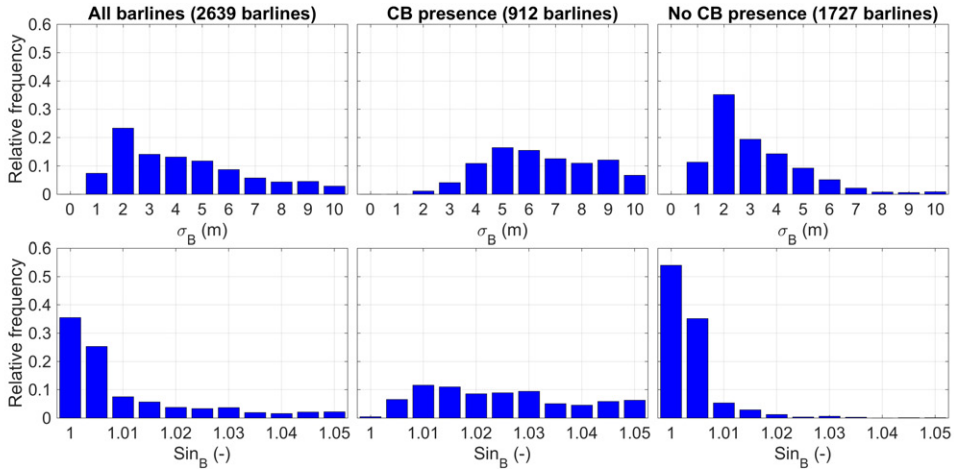

Figure 4.14 Histograms of the standard deviation of the barline σ_B (top) and the sinuosity of the barline Sin_B (bottom) for all barlines (left), all barlines with visually detected crescentic bars (middle) and without visually detected crescentic bars (right).

were generally more subtle and could take longer than one day. An additional complication is the inertia (hysteresis) of the system, meaning that the previous morphological configuration affects the time needed for formation and especially straightening. Other reasons that explain the noise in Figures 4.9 and 4.11 are i) the visual analysis was done with 1 daily image (at 12:00) instead of hourly images, and ii) crescentic patterns were sometimes only present in one half of the planview domain with the bar-shoreline distances differing substantially in the planview, meaning that the alongshore-averaged bar-shoreline distance was not fully representative. Finally, the wave conditions that occurred in the 24 hours before midday were considered for each BLIM image. However, since formation (straightening) could take more (less) than 24 hours, an excess (lack) of wave conditions could be considered regarding formation (straightening). Sensitivity was checked and Figures 4.9 and 4.11 hardly change when decreasing the number of hours to 18 or 12.

4.4.2 Comparison with previous observations

A strong result of this study is that the initial bathymetry plays an important role in the formation of crescentic bars. Crescentic bars were only observed when the bar-shoreline distance exceeded 10–15 m (Figures 4.11b and 4.15) and they were hardly observed when the bar-shoreline distance exceeded 60 m (Figures 4.11b and 4.15). Previous studies (Holman et al., 2006; Contardo and Symonds, 2015) also reported that initial bathymetric conditions strongly influenced crescentic bar dynamics. Other characteristics of the cross-shore inner bar profile at the study site are unfortunately unknown, because the topobathymetry was at most surveyed every 6 months and the inner bar profile was often not measured. The last 3 surveys indicate that an inner terrace instead of an inner bar can occur at the study site (Figure 4.2), meaning that the inner barlines tracked with BLIM might often reflect terrace edges instead of real bars.

At the study site, crescentic bars were only observed in the outer bar during 2017–2018, when a few strong storms caused a change in bar configuration. The bar was arrested in

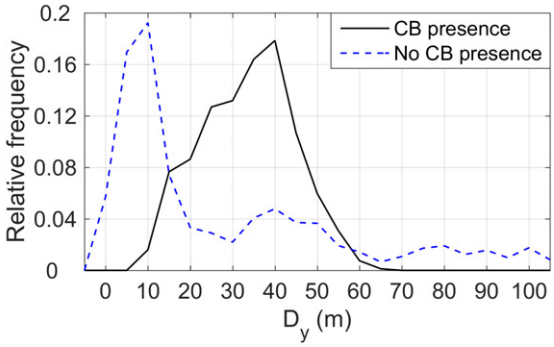

Figure 4.15 Distribution of bar-shoreline distance D_y on days with and without crescentic bar presence.

between the storms, which explains the long crescentic bar events in 2018 (Figure 4.4f and Table 4.1). The inner bar was only arrested during periods with low-energetic wave conditions (H_{mo} < 0.2 m) that were excluded from our data and mostly occurred during summer (e.g., during summer 2013; Figure 4.6). Similar observations were made at other Mediterranean beaches (e.g., Ojeda et al., 2011).

The large number of observed crescentic bar events allowed for a detailed analysis of the wave conditions during crescentic bar presence and formation/straightening moments. From now on, the mentioned wave angles are taken with respect to the boundary of −5° at 10 m depth (see Section 4.2.3). Analysing the wave conditions reveals that during crescentic bar straightening (Figures 4.9f and 4.16a and Table 4.2), oblique waves were dominant (on average $\theta_{mean} \gtrsim 15°$ at 10-m depth) and shore-normal waves were mostly absent. Furthermore, the waves were more energetic than during crescentic bar formation/presence (mean H_{mo} of 0.73 m) and there was more variation in wave height (Figure 4.16b). This indicates that bar straightening occurred during medium and high-energetic oblique wave conditions. Waves were generally low energetic during crescentic bar formation and crescentic bar presence (mean H_{mo} < 0.6 m; Figures 4.9b-c and 4.16b and Table 4.2). Clearly, the wave angles

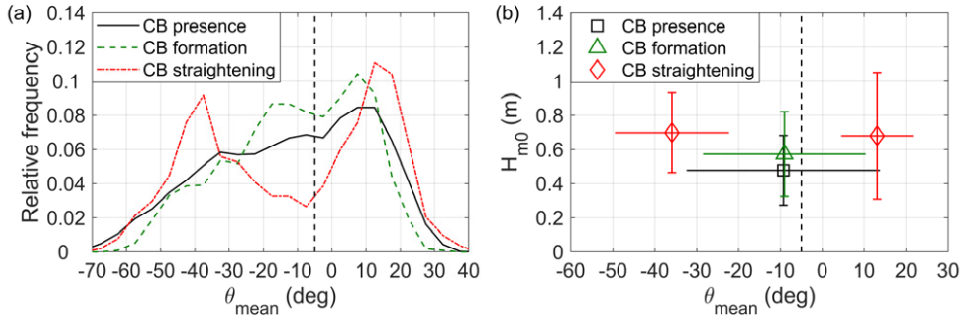

Figure 4.16 Distributions of θ_{mean} at 10-m depth during (a) crescentic bar presence, formation and straightening and (b) the errorbars of the same categories (taken from Figure 4.9b,c,f) collected together to facilitate comparison.

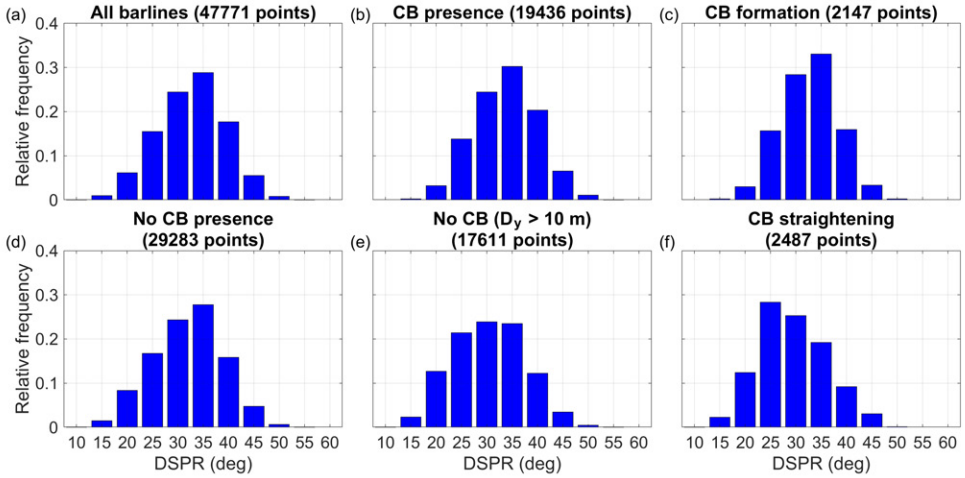

Figure 4.17 Histograms of the distribution of directional spreading at 10-m depth in front of Castelldefels beach for different categories (CB denotes crescentic bar). Only data from the simulation forced with 2D spectra is shown and low-energetic wave conditions (H_{mo} < 0.2 m) are excluded.

during formation were less oblique (mostly $\theta_{mean} \lesssim 20°$) and formation was often observed for shore-normal waves (Figure 4.16a). The wave climates during crescentic bar formation were mostly south-southwesterly and bimodal (since these typically showed smaller angles of incidence), whereas south-southwesterly and east-southeasterly wave climates dominated during crescentic bar straightening (Figure 4.10). Consistent with the lack of bimodal wave climates during crescentic bar straightening, the directional spreading in those moments was relatively small (Figure 4.17).

Crescentic bar formation has been observed to occur in the field both during calm and more energetic wave conditions with relatively small angles of incidence (e.g., Price and Ruessink, 2011; Rutten et al., 2018; Gijsman et al., 2021). At Castelldefels, mostly low-energetic wave conditions were observed during formation (Figure 4.9c) and the angles were 10–20° less oblique compared to the straightening moments (Figure 4.9f). Still, the angles show a wide range (from -30° to +20° at 10 m depth). Previous studies (Contardo and Symonds, 2015; Gijsman et al., 2021) reported crescentic bar development for angles up to 9° (at 10 m depth), whilst Price and Ruessink (2011) observed downstate (accretionary) transitions in the classification scheme of Wright and Short (1984) for angles up to 23° (at 10 m depth). Crescentic bar straightening was previously mainly related to storm conditions (e.g., Ranasinghe et al., 2004; Van Enckevort et al., 2004), whilst later studies (Holman et al., 2006; Price and Ruessink, 2011) related sandbar straightening more to oblique waves. Consistent with several recent studies (Contardo and Symonds, 2015; Rutten et al., 2018; Gijsman et al., 2021), sandbar straightening at Castelldefels predominantly occurred during oblique waves whilst shore-normal waves were almost absent (Figure 4.9f).

At the study site, mean wavelengths varied between 100–700 m (Figure 4.6c) and mean amplitudes between 5–20 m (Figure 4.6d). Yearly averages (Table 4.1) were smaller compared to most previous studies (Table 4.3), which could be related to the small tidal action and low-energetic wave conditions at the study site. However, previous Mediterranean studies

Table 4.3 Overview of several recent crescentic bar and rip-channel observations displaying both site and bar characteristics. All columns show mean values except tides (spring tidal range) and C_y (mean absolute value and absolute range). A comprehensive overview of earlier crescentic bar observations is given in Table 1 of Van Enckevort et al. (2004).

Site	D_{50} [μm]	Slope	Tide [m]	H_{mo} [m]	L_y [m]	A_y [m]	C_y [m/day]	Study period	Reference
Leucate-Plage[1]	600	0.015	0.3	0.8	300	-	- (0.1–0.3)	≈2 years[b]	Certain (2002)
Leucate-Plage[2]	600	0.015	0.3	0.8	600	-	≈0.1 (-)	≈2 years[b]	Certain (2002)
Duck	180	0.013	1.1	0.89	365	24	- (0–60)	2 months[a]	Van Enckevort et al. (2004)
Miyazaki	250	0.013	1.6	1.29	363	34	- (0–50)	2 months[a]	Van Enckevort et al. (2004)
Gold Coast[1]	250	0.02	1.7	1.10	373	15	- (0–45)	3 months[a]	Van Enckevort et al. (2004)
Gold Coast[2]	250	0.02	1.7	1.10	483	24	- (0–35)	3 months[a]	Van Enckevort et al. (2004)
Noordwijk[1]	170	0.007	1.8	1.05	871	36	- (0–60)	10 months[a]	Van Enckevort et al. (2004)
Noordwijk[2]	170	0.007	1.8	1.05	1369	43	- (0–25)	10 months[a]	Van Enckevort et al. (2004)
Palm Beach	300	0.02	1.0	1.5	178	-	2.4 (0–21)	4 years[a]	Holman et al. (2006)
Truc Vert[1]	300	0.02	5.0	1.3	400	-	2.5 (0.5–4.3)	3/13 years[b,c]	Castelle et al. (2007)
Truc Vert[2]	300	0.02	5.0	1.3	700	-	1.0 (-)	3/13 years[b,c]	Castelle et al. (2007)
Monterey Bay	250	0.01	1.5	≈2.0	≈300	-	≈7.0 (0–30)	1–3 years[a]	Orzech et al. (2010)
Gulf of Mexico[1]	-	-	<0.5	0.85	≈500	-	- (-)	1–2 years[b]	Arifin and Kennedy (2011)
Gulf of Mexico[2]	-	-	<0.5	0.85	>1000	-	- (-)	1–2 years[b]	Arifin and Kennedy (2011)
Lido di Dante	215	0.03	0.9	≈0.7	256	-	- (-)	4.5 years[a]	Armaroli and Ciavola (2011)
Sète	200	0.09	0.3	0.7	≈300	≈40	- (-)	4 months[a,b]	Gervais et al. (2011)
Perranporth	350	0.012	6.3	1.5	363	-	- (-)	6 years[a,b]	Scott et al. (2014)
Sète	200	0.09	0.2	0.5	≈400	-	- (0–150)	5 years[a]	Bouvier et al. (2017)
Anmok	400	0.02	0.3	1.1	383	45	- (-)	27 years[c]	Athanasiou et al. (2018)
Zandmotor[3]	280	0.013	1.7	0.97	≈200	-	- (-)	2.4 years[a]	Rutten et al. (2018)
Zandmotor[4]	280	0.013	1.7	0.97	≈450	-	- (-)	2.4 years[a]	Rutten et al. (2018)
Sylt[3]	360	0.033	2.0	≈0.9	670	-	- (-)	40 years[b]	Gijsman et al. (2021)
Sylt[4]	360	0.022	2.0	≈0.9	2240	-	0.2 (-)	40 years[b]	Gijsman et al. (2021)
Castelldefels[1]	270	0.014	0.2	0.57	196	9	4.7 (0–50)	≈8 years[a]	This study
Castelldefels[2]	270	0.014	0.2	0.57	475	14	- (-)	≈8 years[a]	This study

Sandbar detail: [1]Inner bar; [2]Outer bar; [3]Northern part; [4]Western/Southern part
Main dataset: [a]Video data; [b]Bathymetric data; [c]Satellite data

(e.g., Gervais et al., 2011; Bouvier et al., 2017) reported larger wavelengths and amplitudes, which might be related to larger bar-shoreline distances. At Castelldefels, the wavelength increased for larger bar-shoreline distances (Figure 4.12) and similar trends are seen in Table 4.3 for other sites. Alongshore migration rates at Castelldefels could reach up to 50 m/day (Figure 4.6e), but yearly averages were mostly around 5 m/day (Table 4.1). Migration rates were strongly related to the radiation stress S_{xy} (Figure 4.13). Comparable relationships were found previously (Ruessink et al., 2000; Holman et al., 2006), using the longshore component of wave energy flux or a mean alongshore current proxy, respectively. Similar to Holman et al. (2006), the relationship became more significant for longer time spans.

Several moments of fast offshore migration with rates of 20–70 m/day were observed at the study site in response to high-energetic waves (Figure 4.4d), two of which resulted in the formation of a new inner bar. This behaviour is very similar to the episodic Net Offshore Migration (NOM), first described by Ruessink et al. (2009) at the Gold Coast (cross-shore migration up to 30 m/day), and strongly resembles the observed offshore sandbar migration patterns at the low-energetic Italian beach of Terracina (Parlagreco et al., 2019; Melito et al., 2020). NOM patterns were also reported along the low-energetic French Mediterranean coast (Sète beach), both interannually (e.g., Aleman et al., 2017) and episodically (up to 50 m/day; Bouvier et al., 2017). At Castelldefels, fast offshore migration only occurred during storms, but there were also many storms without significant cross-shore migration.

This suggests that the underlying bathymetry also plays an important role in the occurrence of NOM patterns at Castelldefels. Previous studies suggested that NOM patterns also depend on bar steepness and bed slopes (Parlagreco et al., 2019; Melito et al., 2020) and on bar volumes (Ruessink et al., 2009). However, the lack of bathymetric data at Castelldefels makes it impossible to investigate this in detail.

4.4.3 Comparison with previous model studies

Crescentic bars were also the subject of many modelling studies. The first one reproducing the formation of a crescentic bar out of a shore-parallel bar was that of Deigaard et al. (1999). The key processes of the formation mechanism were later on unravelled by Falqués et al. (2000), who termed this feedback mechanism 'bed-surf interaction'. An incipient crescentic bar induces a certain breaking pattern, with more (less) breaking over shoals (channels) that forces an excess (shortness) of mean set-up behind the shoals (channels), so that the typical rip-current circulation is established. This circulation together with a wave-induced excess of sediment re-suspension over the initially shore-parallel bar (typically on its seaward flank) produces deposition (erosion) over the shoals (channels). More details can be found in Ribas et al. (2015). The initial highly-idealised modelling studies were followed by studies with more realistic models that qualitatively reproduced many of the observed characteristics of crescentic bars in single and double barred beaches (e.g., Damgaard et al., 2002; Calvete et al., 2005; Klein and Schuttelaars, 2006; Garnier et al., 2008). Subsequent studies became more sophisticated by including i) a more complex wave description with random frequencies and directional spreading (e.g., Reniers et al., 2004; Smit et al., 2008), ii) roller dynamics (e.g., Ribas et al., 2011), iii) cross-shore transport processes (e.g., Drønen and Deigaard, 2007; Dubarbier et al., 2017), and iv) time-variable offshore wave conditions (e.g., Castelle and Ruessink, 2011). Crescentic bar straightening due to oblique waves was already obtained by Drønen and Deigaard (2007) and Garnier et al. (2013) described in detail the underlying mechanism, related with a downstream shift and weakening of existing rip currents. Under slightly-oblique incident waves, the positive feedback due to the bed-surf interaction is retained but for more oblique waves the downstream shift ends up inducing a negative feedback between flow and morphology.

Some modelling studies investigated the importance of the initial bathymetry in crescentic bar formation. On single-bar profiles, models predict that wavelengths increase with bar-shoreline distance (Damgaard et al., 2002; Calvete et al., 2007). However, other bathymetric characteristics (such as bar trough/crest depths and the bed slope) also have a strong effect on the wavelength (Calvete et al., 2007), but they are generally unknown at Castelldefels. This is the most probable explanation for the large variation in inner bar wavelength as a function of bar-shoreline distance in Figure 4.12. The observed important role of bar-shoreline distance on crescentic bar presence in Castelldefels (minimum distance of 10–15 m) remains unexplained by existing modelling studies. In particular, Calvete et al. (2007) found that growth times were not significantly correlated to bar-shoreline distance (Figure 4 of that article) but the range in their study ($65 < D_y < 90$ m) did not include the small bar-shoreline distances in the present data. Moreover, growth times of crescentic bars in terraced beaches strongly increased compared with barred beaches (Calvete et al., 2007), whilst crescentic bars are likely present when an inner terrace exists at Castelldefels beach. In contrast to single-bar profiles, modelling studies using double barred profiles systematically predict larger wavelengths in

the outer bar compared to the inner bar (Klein and Schuttelaars, 2006; Smit et al., 2008; Thiébot et al., 2012), similar to the observations at Castelldefels.

The role of wave conditions on crescentic bars was also the subject of many modelling studies. Table 4.4 provides an overview of such studies in different settings that used wave conditions that roughly resemble those at Castelldefels (significant wave height $H_s \leq 2$ m, peak period $T_p \leq 6$ s, wave angle $\theta > 3°$ at 10-m depth). In the absence of any specific study for Castelldefels beach, the results of the studies in Table 4.4 will be compared to the Castelldefels observations. However, the comparison can only be done qualitatively, as the bathymetries and wave conditions in the models were most of the time different from Castelldefels. The inner bar along the Dutch coast and at Duck (USA) is located farther from shore and the wave heights and periods in all model studies are larger compared to the averages (0.6 m and 4 s) at Castelldefels. As shown in Table 4.4, reported growth times in modelling studies are either the *e*-folding growth time, T_g (time needed to multiply the bar height by a factor e) or the saturation time, T_s (time needed for the bar to reach a relatively constant bar height). The observations in Castelldefels, with crescentic foam patterns appearing after 1–2 d, are only comparable to model results with $T_s < 5$ d or $T_g < 1$ d (several amplification cycles are needed before the crescentic bar affects the foam pattern).

The role of wave conditions in modelling studies is in qualitative agreement with observations at Castelldefels, with formation occurring for less oblique waves and straightening occurring for larger angles (wave height playing a minor role), but some details are not completely captured by models. Crescentic bars generally form in models for $\theta < 5°$ at 10-m depth, a value significantly smaller than the observations at Castelldefels. Larger incidence

Table 4.4 Overview of model results for crescentic bar formation for comparison with Castelldefels data. Wave conditions are given at 10-m depth and for double-bar studies only values at the inner bar are given. The *e*-folding growth time T_g, or saturation time T_s are provided in the model studies, together with the wavelength L_y and migration rate C_y. C_y^{obs} indicates the observed migration speeds that, according to the 2-day linear fit in Figure 4.13, correspond to the S_{xy} values of the model studies.

Profile	D_y [m]	D_{50} [μm]	T_p [s]	H_{mo} [m]	θ [deg]	S_{xy} [J/m^2]	T_g [days]	T_s [days]	L_y [m]	C_y [m/day]	C_y^{obs} [m/day]	Reference
Single bar (Duck, USA)	80	200	6.0	2.0 2.0 2.0 1.9	4.3 8.6 13 17	126 247 362 465	0.8 1.0 1.3 1.7	- - - -	300 450 550 700	36 60 84 108	27 51 73 94	Calvete et al. (2005)[3]
Inner bar[1] (Dutch coast)	130	250	6.0	1.0	8.6	66	0.4 -	- 2	600 1000	80 100	15	Klein and Schuttelaars (2006)
Single bar (Duck, USA)	80	250	7.5	1.3	4.2 5.6	59 79	2.8 4.2	- 30	200 220	22 28	14 18	Garnier et al. (2008)[4]
Inner bar[1] (Dutch coast)	145	150	6.0	1.0	10	75	-	5	600	-	-	Smit et al. (2008)
Inner bar[2]	50	200	6.5	2.1	5.3	189	2.9	-	200	43	39	Thiébot et al. (2012)
Single bar (Duck, USA)	80	250	6.0	1.4	5.3	74	-	30	250	20	17	Nnafie et al. (2020)[5]

[1] No formation on the outer bar
[2] Formation also on the outer bar (not shown)
[3] Similar results for $H_s = 1.3$ m
[4] Similar results for $T_p = 6$ s
[5] Results for constant θ case

angles either lead to excessively long evolution times, with growth time $T_g > 2$ d or saturation time $T_s > 10$ d, or wavelengths become much larger (> 500 m) than those observed at Castelldefels (references in Table 4.4; as well as Castelle and Coco, 2012; Price et al., 2013). More advanced models that include directional spreading in the wave forcing (Reniers et al., 2004; Smit et al., 2008) or use a time-variable wave angle (Castelle and Ruessink, 2011; Nnafie et al., 2020; Nnafie et al., 2021), cross-shore transport (Rutten et al., 2019) or algorithms to evaluate the cumulative effects of waves and their variations (Tiessen et al., 2010), predict formation for larger angles but still fail to reproduce the wide range of angles at which formation occurs at Castelldefels beach. The same applies to crescentic bar straightening, which is observed for angles much larger than those predicted by models (Garnier et al., 2013).

Once formed, crescentic bars experience both alongshore migration and changes in wavelength due to splitting and merging. In order to test the migration rates reported in existing modelling studies, Figure 4.13 has been used to compute the observed migration rate corresponding to the S_{xy} values implemented in the models (Table 4.4). Most models (Calvete et al., 2005; Garnier et al., 2008; Thiébot et al., 2012; Nnafie et al., 2020) report migration rates 50% larger than the observed ones and growth times are also too large ($T_g \sim 1$–2 d). In the only modelling study with $\theta > 5^\circ$ and $T_g < 1$ d (Klein and Schuttelaars, 2006), the migration speed is overpredicted by a factor 6. The discrepancy between observed and modelled migration rates was also pointed out by Castelle et al. (2012). Including time-variable wave angles does not affect migration rates (Nnafie et al., 2020), but they decrease for larger grain sizes (Dong et al., 2015) or when including roller dynamics (Ribas et al., 2011). Finally, merging and splitting (as observed at Castelldefels) is clearly enhanced for variable offshore wave conditions (Castelle and Ruessink, 2011; Nnafie et al., 2020; Nnafie et al., 2021), due to the system adjusting to the new forcing.

4.5 Conclusions

Over 7.5 years of daily time exposure images and propagated directional wave conditions (to 10-m depth) were used to study the dynamics of crescentic bars at Castelldefels beach (northwestern Mediterranean sea). Formation and straightening moments of the crescentic bars were detected in detail, allowing an accurate assessment of the wave conditions during these moments. Throughout the study period, the beach was very dynamic and a total of 98 crescentic bar events were observed lasting 1389 days (48% of the time). Crescentic bar events occurred unevenly over the different years and their duration varied significantly during the study period (from days to months).

Crescentic bars were only observed when the sandbar was located at least 10 m from shore, indicating that crescentic bar formation depends strongly on the initial bathymetric configuration. The bar should not be located too far from shore either, as the low-energetic waves at the study site typically do not induce morphological changes at deeper water. As a result, the outer bar remained arrested during most of the study period. The sandbars experienced significant cross-shore movement during the study period and several moments of fast offshore migration occurred (up to 70 m in one day). Fast offshore migration was only observed during storms, but there were also many storms without major cross-shore movement. The observed fast offshore migration patterns are similar to episodic NOM, which has been described and observed in various previous studies.

A large variability (100–700 m) in crescentic bar wavelength was observed (due to splitting and merging) and wavelengths increased with bar-shoreline distance. The variation in amplitude (5–20 m) was limited. Compared to previous studies, the mean wavelengths and amplitudes (~200 m and ~9 m, respectively) are relatively small, which is probably due to the smaller mean wave energy at the study site. Alongshore migration speeds were mostly small (< 5 m/day), although larger values (up to 50 m/day) were observed during crescentic bar events with larger wavelengths and amplitudes. A clear relationship was found between the migration speed and S_{xy} (the alongshore transport of cross-shore momentum). Using S_{xy} values to compare modelled and observed migration speeds confirmed that existing models generally overpredict migration rates or underpredict growth times.

Average wave conditions at the study site were typically low-medium energetic waves (mean H_{m0} ~0.6 m) with a large variety in wave angle (up to 50°). Crescentic bar formation was mostly observed during low-medium energetic waves (average H_{m0} ~0.6 m) with both shore-normal and limited oblique angles of incidence ($\theta_{mean} \lesssim 20°$ at 10-m depth), including angles for which existing models predict straightening. Crescentic bar straightening could occur every few days and happened both during medium and higher energetic waves (mean H_{m0} = 0.73 m). Wave angles were generally very oblique ($\theta_{mean} \gtrsim 15°$ at 10-m depth), which is a much larger threshold than obtained from model simulations. On the whole, the detailed wave conditions in the present study prove that existing crescentic bar modelling studies may be inaccurate during oblique waves, either underpredicting crescentic bar formation or overpredicting wavelengths and migration rates.

Chapter 5 | Observations of megacusp dynamics and their coupling with crescentic bars at an open, fetch-limited beach

Abstract

Alongshore changes in shorelines along sandy beaches are a result of variations in wave conditions and nearshore morphology, which can cause straight shorelines to develop large-scale (100–1000 m wavelength) undulations called megacusps that cause local shoreline accretion and erosion. Megacusps are often morphologically coupled to alongshore variability in the nearshore sandbar (crescentic bars). Sandbar rhythmicity has been studied extensively, whilst megacusp dynamics and their coupling with crescentic bars have received less attention. This study uses a long-term dataset of hourly time-exposure video images and detailed propagated wave conditions to investigate megacusp dynamics and the corresponding sandbar-shoreline coupling at the low-energetic, tideless beach of Castelldefels (northwestern Mediterranean Sea, Spain). The analysis shows that megacusps occurred during 24% of the study period and crescentic bars were present 91% of all days with megacusps. Conversely, megacusps were not observed during 50% of the days with crescentic bar presence. Megacusp wavelengths (100–700 m) were comparable to crescentic bars, whilst cross-shore amplitudes (3–8 m) and alongshore migration speeds (0–15 m/day) were smaller than those of crescentic bars. No clear relation was observed between wave conditions and megacusp dynamics. However, megacusp presence was strongly linked to crescentic bar presence as megacusps mostly developed some days after the formation of a crescentic bar. Coupling between shoreline and inner sandbar was significant during 74% of the time with simultaneous presence of megacusps and crescentic bars. No dominance of one particular coupling pattern was observed, although the pattern depended on the wave height and the wave angle. It is hypothesised that the wave height and angle determine the type of flow pattern over the inner crescentic bar (single or double rip cell circulations versus meandering currents) and thus control the type of coupling.

Submitted as:

De Swart, R. L., F. Ribas, D. Calvete, G. Simarro, and J. Guillén (2022). Observations of megacusp dynamics and their coupling with crescentic bars at an open, fetch-limited beach. Submitted to *Earth Surface Processes and Landforms*.

5.1 Introduction

Shorelines along sandy coasts can display a wide range of morphological patterns due to changes in hydrodynamics and sediment transport. One example of such patterns are megacusps, which are alongshore shoreline undulations consisting of horns (seaward shoreline protusions) and embayments (landward shoreline perturbations) that typically have wavelengths of hundreds of metres and cross-shore amplitudes (half the cross-shore distance between megacusp horns and bays) up to several tens of metres (e.g., Thornton et al., 2007; Castelle et al., 2015; Segura et al., 2018). Similar alongshore variability (consisting of shoreward horns and seaward bays) is often present in the nearshore sandbar in which case they are referred to as crescentic bars or rip-channel systems (e.g., Van Enckevort et al., 2004). Morphological coupling is often present between megacusps and crescentic bars (e.g., Sonu, 1973; Coco et al., 2005; Van de Lageweg et al., 2013) and the coupling pattern varies significantly between beaches. The coupling between crescentic bars and megacusps is important for coastal management as the evolution of megacusps can lead to fast changes in shoreline position (Thornton et al., 2007; Birrien et al., 2013). Megacusp formation during low-energetic waves is often linked to shoreline accretion (e.g., Van de Lageweg et al., 2013; Segura et al., 2018), whilst megacusp development during storms can induce significant beach and dune erosion at the megacusp embayments (Thornton et al., 2007; Castelle et al., 2019).

Shoreline and sandbar variability has been extensively studied in the past decades. Specifically the ability to track sandbar variation using video images (Lippmann and Holman, 1989) resulted in a large number of studies investigating crescentic bars (e.g., Van Enckevort et al., 2004; Price and Ruessink, 2011) and, to a lesser extent, megacusps (e.g., Orzech et al., 2011; Segura et al., 2018). Generally, formation of crescentic bars was observed during low-energetic wave conditions with limited obliquity (e.g., Van Enckevort et al., 2004) and bar straightening during more energetic waves or strong oblique angles of incidence (e.g., Contardo and Symonds, 2015). Some previous studies observed megacusps to form during lower energetic conditions and to disappear during storms (e.g., Birrien et al., 2013), although megacusps were also observed to persist during storms (e.g., Aagaard et al., 2005; Quartel, 2009) and to disappear during lower energetic wave conditions (Segura et al., 2018). Large erosive megacusps could also form during storms and cause strong dune erosion (Castelle et al., 2019). Reported megacusp characteristics show a large variety, with average wavelengths ranging from 100 m to 2 km and average cross-shore amplitudes from 3 to 15 m (Thornton et al., 2007; Castelle et al., 2015; Segura et al., 2018). Several studies also observed alongshore migration of megacusps (e.g., Thornton et al., 2007; Quartel, 2009) with reported rates sometimes exceeding 30 m/day (Galal and Takewaka, 2008). Finally, the coupling between crescentic bars and megacusps has been observed in phase (megacusp embayments in front of shoreward crescentic bar horns) and out of phase (shoreline embayments in front of seaward crescentic bars bays) on timescales up to years (e.g., Van de Lageweg et al., 2013; Castelle et al., 2019). However, comparing previous observations of coupling patterns should be done carefully, as earlier studies often defined in phase and out of phase coupling exactly the other way around (e.g., Sonu, 1973; Balouin et al., 2013).

Although coupling between crescentic bars and megacusps has been observed regularly in the field and forms an important part of the beach state classification scheme of Wright and Short (1984), nearshore models often use a fixed shoreline (e.g., Garnier et al., 2008). Modelling studies in which the shoreline and sandbar are allowed to evolve generally show out of phase coupling (e.g., Castelle and Ruessink, 2011; Orzech et al., 2011), although these

studies mostly do not focus on sandbar-shoreline coupling. To date, there is no consensus regarding the relation between coupling patterns and the wave and tide conditions. Existing model studies (e.g., Calvete et al., 2005; Orzech et al., 2011; Coco et al., 2020) showed opposing results and observational studies (e.g., Orzech et al., 2011; Van de Lageweg et al., 2013) sometimes also contradicted each other.

Available observational studies on megacusps and sandbar-shoreline coupling are often limited in time (e.g., Quartel, 2009; Birrien et al., 2013) or temporal resolution (e.g., Sonu, 1973; Thornton et al., 2007). Additionally, they mostly studied beaches with considerable tidal range (> 1 m) and high-energetic (H_{mo} > 1 m) wave conditions (e.g., Van de Lageweg et al., 2013; Castelle et al., 2019) or long fetches (Segura et al., 2018). Only a limited number of studies focused on low-energetic areas (like the Mediterranean Sea) with insignificant tides and small fetches (e.g., Bowman and Goldsmith, 1983; Balouin et al., 2013) and they mostly used data with limited temporal resolution and/or short study periods. Additionally, they did not provide a detailed analysis of the megacusp dynamics and the coupling between megacusps and crescentic bars. Furthermore, most previous studies on sandbar-shoreline coupling generally only dealt with in phase versus out of phase coupling and overlooked intermediate coupling patterns. As a result, more observations that quantify the various coupling patterns and megacusp formation/disappearance moments are needed for validating model results.

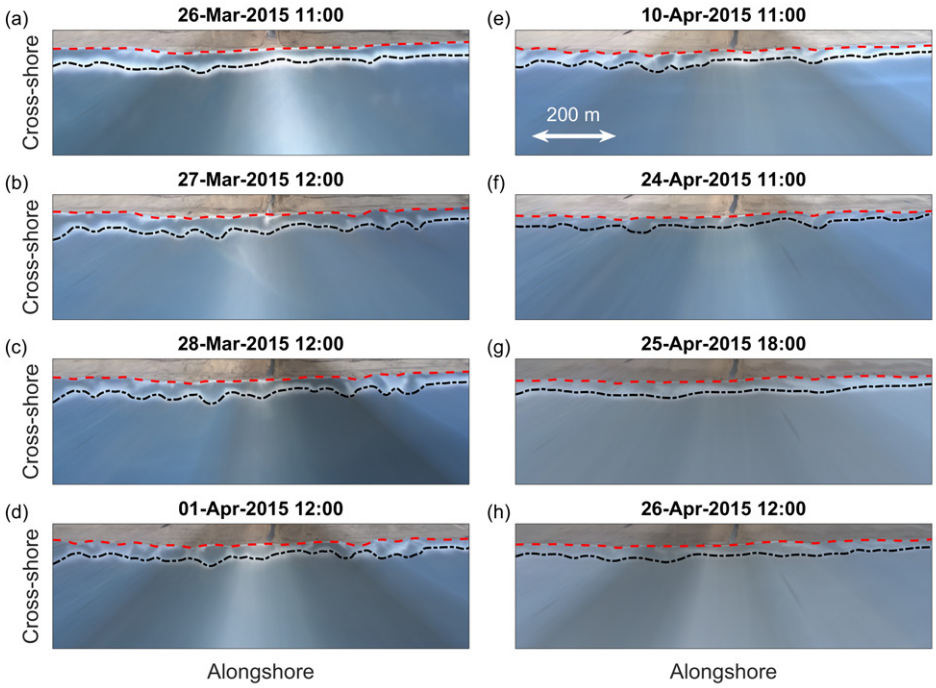

Figure 5.1 Planview images of Castelldefels beach (1000 m alongshore and 300 m cross-shore) showing examples of formation (a-c), development (d,e) and disappearance (f-h) of a megacusp event. The tracked barlines $B(y)$ and shorelines $S(y)$ are plotted in all planviews. The planviews correspond to the same event shown in Figure 5.8.

The objective of the present study is to characterise megacusp events and the coupling between megacusps and crescentic bars and link them to the prevailing wave conditions. This is done for the open, fetch-limited, tideless beach of Castelldefels (northwestern Mediterranean Sea, Spain) using a nearly 8-years dataset of hourly video images and hourly propagated wave conditions. Special attention is given to quantify the role of directional wave conditions and the bathymetric configuration on megacusp formation/disappearance and the emergence of different coupling patterns (in phase, out of phase and intermediate). The field site and the available datasets have already been extensively described in Chapters 2.The methods used to collect and characterise the data are described (Section 5.2). Subsequently, the results of the analysis are presented (Section 5.3) and contextualised and compared with previous studies (Section 5.4). Finally, the most important findings are summarised in the conclusions (Section 5.5).

5.2 Methods

5.2.1 Visual analysis and data collection

This study also uses the dataset of nearly 8-years (5 October 2010 to 31 August 2018) of time-exposure planview images that was already used in Chapter 4 to track the sandbars during the entire study period by detecting the dominant wave breaking areas in the time-exposure images (from now on called barlines; Figure 5.1). As outlined in Chapter 4, these barlines were obtained for 2279 images spanning 2208 days. An extensive description of the dataset with planview images can be found in Section 2.3 of Chapter 2, whereas Section 4.2.1 of Chapter 4 provides more information about the dataset with barlines.

The analysis of the planview dataset for megacusp events started with an initial visual analysis of daily images (at 12:00 midday) by two experienced researchers to reduce subjectivity. The occurrence of megacusp events in the shoreline was tracked, including the dates of formation and disappearance. Subsequently, the two separate analyses were compared and the disagreements in megacusp presence (10% of the total time) were cross-checked to increase reliability and obtain the final visual analysis. A megacusp event was defined when three or more shoreline undulations with a certain rhythmicity were present in at least half of the planview domain for a minimum of two days. Shorelines with two undulations were also included when the wavelength was such that more undulations did not fit in the planview domain. Megacusp events lasting one day were included when a clear rhythmic pattern was present in the entire planview domain. During an image gap, a megacusp event was assumed to continue when the megacusp pattern in the first image after the gap resembled the pattern in the last image before the gap. Specific attention was paid to detecting the moments of megacusp formation and megacusp disappearance (Figure 5.1). A formation moment (Figure 5.1b) was defined as the first day when megacusps were observed in the planview images, following a period without such features. Planview images in which the alongshore variability of the shoreline increased (e.g., a clear increase in megacusp amplitude) were categorised as reinforcement moments and added to the dataset of formation moments. A disappearance moment (Figure 5.1h) was defined as the first day in which megacusps were no longer observed following a period with megacusps. Planview images in which the alongshore variability of the shoreline decreased (e.g., a clear reduction in amplitude) but the undulations persisted (same horn/bay locations, identical wavelengths) were categorised as partial disappearance moments and added to the dataset with disappearance moments. All these criteria

are coherent with those used in Section 4.2.1 for the detection of crescentic bars. The megacusp events were further separated in events with and without crescentic bars by checking whether a crescentic bar was present at some point during each event. Similarly, crescentic bar events were separated in events with and without megacusps.

The uShore software (Ribas et al., 2020) was used to automatically extract the shorelines from all planview images, using the same settings as described in Section 4.2.1. The acquired shorelines were visually analysed to select the best shoreline for each day. For the 145 days without a shoreline of sufficient quality, the shorelines were manually digitised using the best-quality planview image. Finally, all the final shorelines were subjected to one final visual check to verify that the megacusp undulations were correctly captured. Shorelines that did not meet this requirement were modified to better follow the real shoreline. In total, one shoreline was obtained for each day with camera images (2664 images in total). More info about the shoreline extraction procedure can be found in Section 4.2.1 and Ribas et al. (2020).

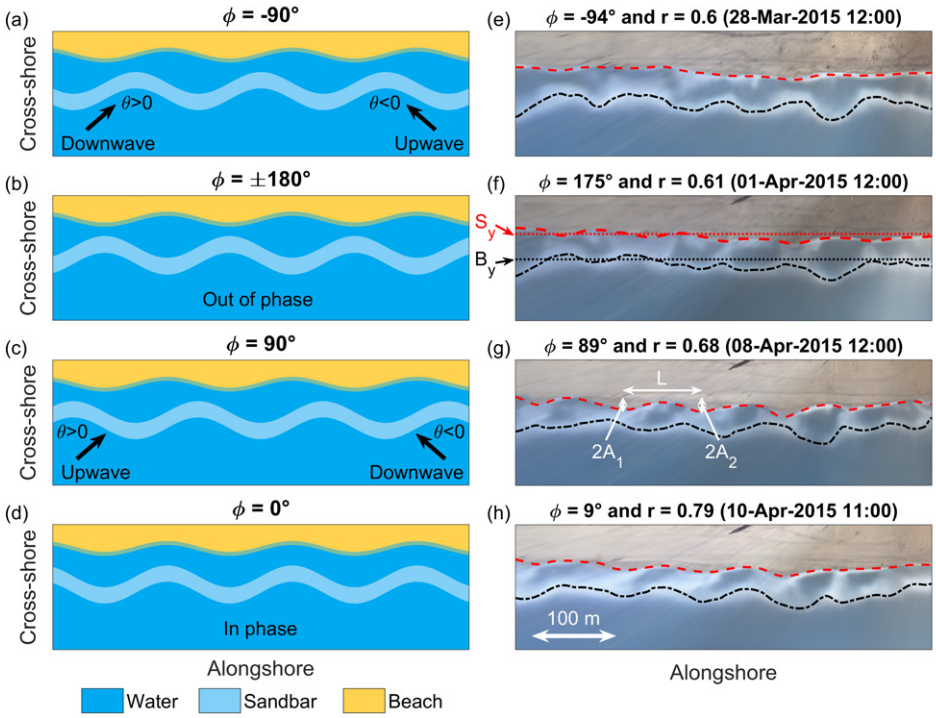

Figure 5.2 Definitions of the different coupling patterns. The left panels show idealised sketches of the four distinguished coupling patterns based on the phase ϕ: (a) $\phi = -90^\circ$ (upwave for easterly waves; downwave for westerly waves), (b) $\phi = \pm 180^\circ$ (out of phase; crescentic bar bays located inside the shoreline embayments), (c) $\phi = +90^\circ$ (upwave for westerly waves; downwave for easterly waves) and (d) $\phi = 0^\circ$ (in phase; crescentic bar horns located inside the shoreline embayments). Zoomed planviews (500 m alongshore, 150 m cross-shore) showing examples of the different coupling patterns are shown in panels (e)-(h) including the computed values for r and ϕ. The tracked bar (black) and shorelines (red) are plotted in all images. Furthermore, (f) shows the alongshore-averaged bar- and shoreline positions B_y and S_y, whereas (g) shows examples of shoreline wavelength L and the double partial amplitudes $2A_1$ and $2A_2$ (the amplitude A is defined as $A = \frac{A_1+A_2}{2}$).

5.2.2 Bar and shoreline characterization

For every shoreline, the cross-shore shoreline positions $S(y)$ were obtained for all alongshore positions y. Time series of the alongshore-averaged shoreline positions $S_y(t)$ were also computed (Figure 5.2f) as were time series of the sinuosity of the shoreline positions $Sin_S(t)$ (Ojeda et al., 2011). The dataset of barlines obtained in Chapter 4 was used to obtain the cross-shore barline positions $B(y)$ and the time series of the alongshore-averaged barline positions $B_y(t)$ and the sinuosity of the barline positions $Sin_B(t)$. Finally, time series of the alongshore-averaged sandbar-shoreline distances were obtained ($D_y(t) = B_y(t) - S_y(t)$).

In all shorelines with megacusps, the bay and horns were detected under the conditions that a minimum cross-shore distance of 3 m and a maximum alongshore distance of 500 m existed between a successive bay and horn. These limitations were set to avoid the detection of small (typically short-lived) undulations as megacusps and to make sure that at least one full undulation (two horns and one bay) occurred in the planview domain. For each megacusp (MC) undulation (Figure 5.2g), the wavelength L_{MC} was computed as the alongshore distance between the horns and the amplitude A_{MC} was computed as half the average cross-shore distance between the bay and the two adjacent horns. Typically, the variation in A_{MC} within the same shoreline was small (average standard deviation of 1 m), whereas the variation in L_{MC} was much larger (average standard deviation of 58 m). Only shorelines in which megacusps were present in at least 40% of the planview domain (combined wavelength of all undulations exceeding 400 m) were used for analysing megacusp characteristics. For each shoreline, the alongshore-averaged wavelengths and amplitudes $L_{y,MC}$ and $A_{y,MC}$ were obtained by averaging L_{MC} and A_{MC}. The alongshore-averaged crescentic bar (CB) wavelengths $L_{y,CB}$ and cross-shore amplitudes $A_{y,CB}$ were obtained analogously (see Section 4.2.2).

Lastly, alongshore megacusp migration rates were computed by cross-correlating detrended shorelines. Each shoreline that was part of a megacusp event was cross-correlated to shorelines dating between 2 and 4 days after the original shoreline (only if they belonged to the same megacusp event). The alongshore displacement of the megacusps $s_{y,MC}$ is given by the lag belonging to the positive peak located closest to the origin of the cross-correlogram. The direction of migration is indicated by the sign of the lag (positive for eastward migration). A minimum normalized correlation of 0.7 was enforced. To obtain the migration rate $C_{y,MC}$, the displacement $s_{y,MC}$ is divided by the time lag between the two correlated shorelines. Migration speeds of crescentic bars $C_{y,CB}$ were obtained analogously (see Section 4.2.2).

5.2.3 Bar and shoreline coupling

At the study site, only the inner bar was relevant for quantifying the sandbar-shoreline coupling as the outer bar was located too far seaward and mostly inactive due to insufficient wave energy. Whether the inner sandbar and shoreline were morphologically coupled was evaluated by cross-correlating the detrended barline $\hat{B}(y)$ with the detrended shoreline $\hat{S}(y)$ of the same day (e.g., Price and Ruessink, 2013; Rutten et al., 2018). The cross-correlation ρ between $\hat{B}(y)$ and $\hat{S}(y)$ was computed as

$$\rho(\Delta y) = \frac{R_{\hat{B}\hat{S}}(\Delta y)}{\sqrt{R_{\hat{B}\hat{B}}(0) R_{\hat{S}\hat{S}}(0)}}, \tag{5.1}$$

where $R_{\hat{B}\hat{S}}(\Delta y)$ is the covariance function of $\hat{B}(y)$ shifted over a spatial lag Δy ($\hat{B}(y + \Delta y)$) and $\hat{S}(y)$ at time t along the whole domain (Ruessink et al., 2007). The lag Δy corresponding

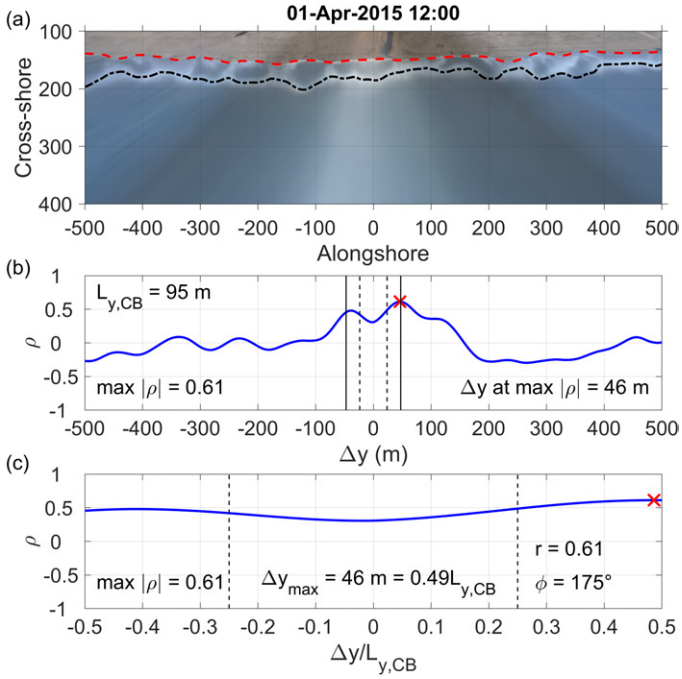

Figure 5.3 Example of a situation where the coupling pattern cannot be deduced solely from the cross-correlation ρ. Panel (a) shows the planview of 1 April 2015 and the tracked inner barline and shoreline, displaying a clear out of phase coupling pattern. Panel (b) shows the cross-correlation ρ versus lag Δy obtained by cross-correlating the inner barline and shoreline. The red cross indicates the largest $|\rho|$ value and the other visible numbers correspond to the crescentic bar wavelength $L_{y,CB}$ and the lag Δy corresponding to the largest $|\rho|$ value. The two solid (dashed) vertical lines indicate $\pm 0.5 L_{y,CB}$ ($\pm 0.25 L_{y,CB}$). Panel (c) shows panel (b) for the interval $[-0.5 L_{y,CB} \leq \Delta y \leq +0.5 L_{y,CB}]$. The lags have been normalised by dividing them by $L_{y,CB}$ and the dashed lines indicate $\pm 0.25 L_{y,CB}$. The largest $|\rho|$ value (red cross) and corresponding lag Δy_{max} in the current domain are also shown, as are the absolute largest correlation r ($r = |\rho(\Delta y_{max})|$) and obtained phase ϕ.

to the largest $|\rho|$ value indicates the alongshore displacement of the inner sandbar undulations with respect to those in the shoreline, where positive (negative) lags indicate eastward (westward) displacements. The ρ value can vary between -1 (maximum negative correlation) and $+1$ (maximum positive correlation). The 98% confidence interval of significant cross-correlation was computed using a reduced number of effective points (Garrett and Toulany, 1981), following Price and Ruessink (2013).

In previous studies (e.g., Rutten et al., 2018), $\rho < 0$ was assumed to correspond to out of phase coupling (crescentic bar bays located inside the shoreline embayments; Figure 5.2b) and $\rho > 0$ to in phase coupling (crescentic bar horns located inside the shoreline embayments; Figure 5.2d). However, this only applies when $|\Delta y|$ belonging to the largest $|\rho|$ value does not exceed a quarter of the wavelength of the coupled pattern. This was not always true in the current dataset, as the example in Figure 5.3 clearly shows. This meant that additional analysis was required to identify the coupling types and to characterise the phase between the two signals. First, the lag corresponding to the largest $|\rho|$, called Δy_{max}, was detected in

the interval $[-0.5L_{y,CB} \leq \Delta y \leq 0.5L_{y,CB}]$, where $L_{y,CB}$ are the crescentic bar wavelengths. The corresponding absolute largest correlation value, called r, was also obtained ($r = |\rho(\Delta y_{max})|$). When $|\Delta y_{max}| > 0.25L_{y,CB}$, the coupling type is opposite to that suggested by the sign of $\rho(\Delta y_{max})$. This was taken into account by computing the phase ϕ (wrapped to the interval $[-180°, 180°]$) following

$$\phi = 360° \frac{\Delta y_{max}}{L_{y,CB}} \quad \text{when} \quad \rho(\Delta y_{max}) \geq 0, \tag{5.2}$$

$$\phi = 360° \frac{\Delta y_{max}}{L_{y,CB}} - 180° \quad \text{when} \quad \rho(\Delta y_{max}) < 0. \tag{5.3}$$

Using this methodology, $\phi = 0°$ always corresponds to in phase coupling (Figure 5.2d) and $\phi = \pm 180°$ always corresponds to out of phase coupling (Figure 5.2b). Taking out of phase coupling as reference, the intermediate cases of $\phi = -90°$ and $\phi = +90°$ were classified as upwave or downwave (depending on the angle of incidence θ; Figure 5.2a,c). Downwave (upwave) coupling indicates that the crescentic bar horn has migrated downdrift (updrift) with respect to the megacusp horn in the out of phase reference case. The lags were nondimensionalised using the crescentic bar wavelengths because, compared to megacusps, crescentic bars were generally more pronounced in the planviews.

When following previous studies, the coupling pattern in Figure 5.3 would have been classified as in phase, since $\rho(\Delta y_{max})$ is positive. This is true if $|\Delta y_{max}|$ does not exceed $0.25L_{y,CB}$. However, when looking at Figure 5.3c, Δy_{max} is close to $0.5L_{y,CB}$. As a result, the coupling type is opposite to that suggested by the sign of $\rho(\Delta y_{max})$, which becomes evident when computing the phase ϕ. The obtained value for ϕ (175°) indicates out of phase coupling, which corresponds with the visible pattern in Figure 5.3a.

Since barlines and shorelines were normalised during cross-correlation, numerous cases of significant sandbar-shoreline coupling were obtained during periods with a straight barline and shoreline. Therefore, this paper only analyses sandbar-shoreline coupling during days on which both a crescentic bar and megacusps were present at the study site.

5.2.4 Waves

The wave conditions used in this study are identical to those used in Chapter 4. Hourly wave conditions (2D frequency-direction spectra and integrated wave parameters) were provided by the Barcelona wave buoy and propagated to 10 m depth in front of the study site using SWAN (see Chapter 3). As explained in Chapter 3, propagating 2D spectra (available 94% of the time) provides the optimal results at the location of interest (particularly regarding θ_{mean}), which is why the propagation of integrated wave parameters is only used for illustrative purposes (grey data in Figures 5.4a-c and 5.7i-j) and not included in the analysis of the shorelines and barlines. The analysis thus only uses the SWAN simulations forced by 2D spectra.

Following Section 4.2.3, the wave conditions assigned to each shoreline and barline were those that occurred in the 24 hours before midday on the day of each shoreline/barline. Shorelines and barlines for which wave conditions were unavailable or $H_{m0} < 0.2$ m more than 75% of the 24 hours were excluded from the analysis. Wave angles with respect to the shore-normal were obtained using a coastline orientation of 89° with respect to North. To distinguish between easterly and westerly waves, a boundary of −5° with respect to shore-normal was set (negative angle indicates east). The reason for this modification was the

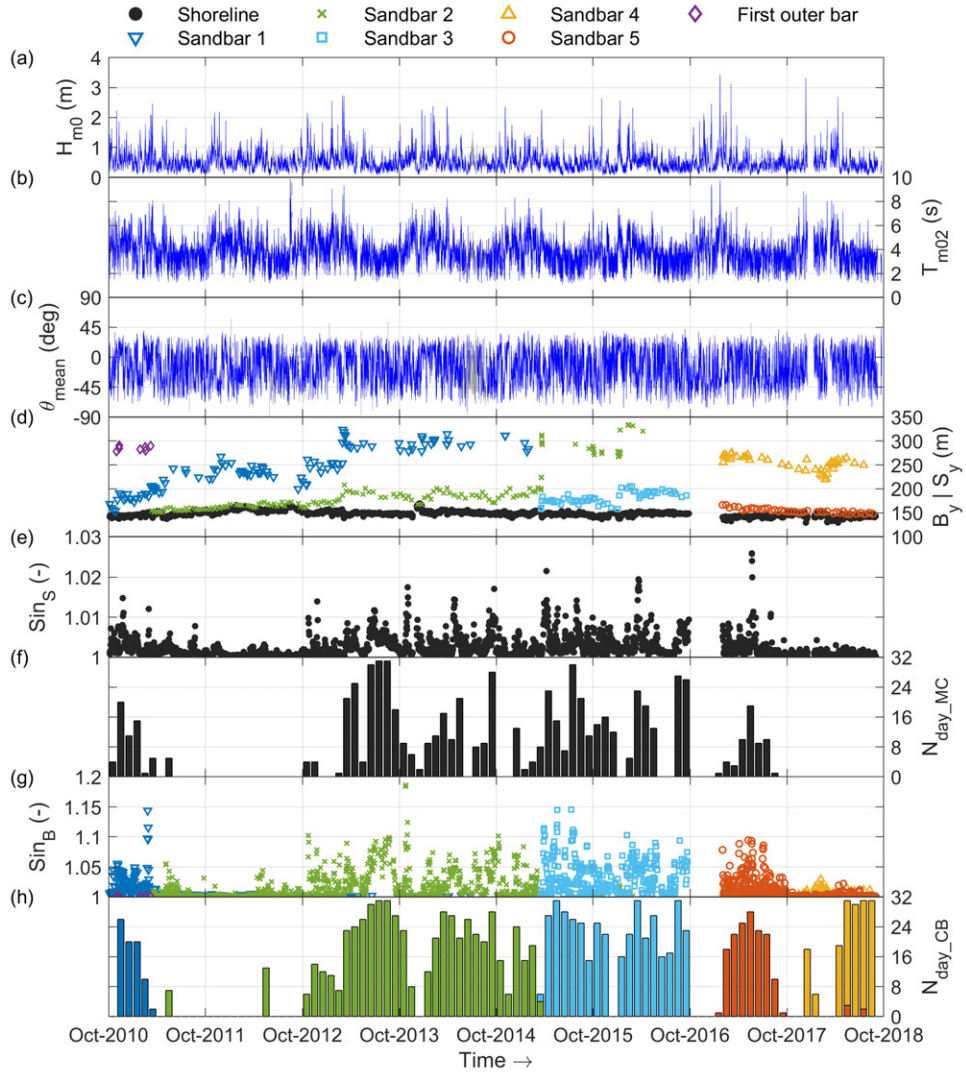

Figure 5.4 The (a) significant wave height H_{m0}, (b) mean period T_{m02}, (c) mean wave direction θ_{mean} from shore normal (positive for westerly waves), (d) alongshore-averaged bar crest and shoreline positions B_y and S_y, (e) sinuosity of the shoreline Sin_S, (f) number of days per month with megacusps $N_{day,MC}$, (g) sinuosity of the barlines Sin_B and (h) number of days per month with crescentic bars $N_{day,CB}$ versus time at Castelldefels beach. Panels (a), (b) and (c) display all hourly wave conditions at 10 m depth in front of the study site (no threshold in H_{m0}) and the colours denote the SWAN boundary conditions: 2D spectra (blue) or integrated wave parameters (grey). To increase readability, only a selection of data points of sandbars 1-5 are shown in panel (d). In case crescentic bars occurred in two different sandbars during the same month (e.g., May and July 2018), the bar with the least amount of days with crescentic bars is shown at the front in panel (h).

bias in propagated wave direction (−7.5° for easterly and 2.3° for westerly waves; see Chapter 3). The radiation stress S_{xy} was computed using the wave conditions following Holthuijsen (2007).

5.3 Results

5.3.1 Shoreline dynamics and megacusp presence

During the study period, the alongshore-averaged shoreline position S_y (with respect to the camera tower) varied between 130 and 170 m, although S_y was mostly close to 150 m (Figure 5.4d) and typically only showed limited short-term variation. A long-term erosional trend in S_y of approximately 8 m was observed during the study period. In contrast to S_y, the alongshore-averaged sandbar positions B_y showed a lot of variability. Six sandbars were tracked during the study period (always two simultaneously), which displayed fast offshore migration (up to 70 m/day) during significant storms and gradual onshore migration during calmer conditions (Figure 5.4a,d). Fast offshore migration of the inner sandbar sometimes resulted in the formation of a new sandbar at the shoreline (Section 4.3.1). Furthermore, the alongshore variability of the sandbars B was generally much larger compared to that of the shorelines S (compare the sinuosity values in Figure 5.4e,g).

As shown in Chapter 4, the inner bar or terrace at Castelldefels often became crescentic and was generally located between 0 and 50 m from shore (100–200 m for the outer bar). Crescentic bar formation strongly depended on the initial bathymetry as they only formed when the bar-shoreline distance exceeded 10 m. A large variability in wavelengths (100–700 m), cross-shore amplitudes (5–20 m) and alongshore migration speeds (0–50 m/day) was observed. Furthermore, the wavelengths increased for larger bar-shoreline distances and alongshore migration was strongly related to the radiation stress S_{xy}. The sandbar typically became crescentic during lower energetic waves with limited obliquity ($\theta \lesssim 20°$ at 10-m depth), whilst higher energetic waves with strong oblique angles ($\theta \gtrsim 15°$) dominated during bar straightening.

A total of 67 megacusp events were detected during the study period spanning 706 days (Table 5.1), meaning that megacusps were present during 24% of the time. No clear seasonal signal exists in the occurrence of megacusps, but they occurred unequally over the study period (Figure 5.4f). Megacusps were frequently observed during 2013–2017, whilst in 2011–2012 and 2018 there were long periods in which they were not present. Megacusp

Table 5.1 Statistics of all megacusp (MC) and crescentic bar (CB) events (inner bar only) during the entire study period and the corresponding mean bar and shoreline characteristics (mean absolute values for C_y). Crescentic bar events are separated in events with megacusp presence and events without megacusp presence. Megacusp events are separated in events with crescentic bar presence and events without crescentic bar presence.

Event type	Number of events	Mean duration [days]	Total duration [days]	S_y [m]	B_y [m]	D_y [m]	L_y [m]	A_y [m]	C_y [m/day]
CB events with MC	55	18	1005	–	180	33	195	9	4.7
CB events without MC	41	5	218	–	178	29	201	6	3.8
MC events with CB	62	11	684	147	–	32	230	4	1.1
MC events without CB	5	4	22	151	–	8	238	4	1.8

events also varied significantly in duration during the study period (from days to months). These longer lasting events are often related to extended periods with low-energetic wave conditions. This leads to the sandbar and shoreline morphology being mostly frozen (arrested; Ojeda et al., 2011) and only diffusion can cause small morphological changes until the wave energy increases.

Generally, megacusps were present together with crescentic bars (Figure 5.4f,h). There were only five megacusp events (lasting in total 22 days) during which no crescentic bars occurred (Table 5.1) and crescentic bars were only absent during 9% of all days with megacusps. Note that during megacusp events without crescentic bars the bar is typically only detached from shore in half of the planview, which explains the small value for the bar-shoreline distance D_y. Conversely, crescentic bars could occur more frequently without the presence of megacusps (Figure 5.4f,h) and megacusps were not present during 50% of the days with crescentic bars. In total, 41 crescentic bar events (lasting 218 days) were observed during which no megacusps occurred (Table 5.1). This indicates that megacusp occurrence strongly depends on crescentic bar presence, whilst the reverse is not true.

5.3.2 Megacusp formation/disappearance

The long study period allowed for a detailed analysis of the conditions leading to megacusp events, including instances of megacusp formation and disappearance. Histograms of the wave height and wave direction for the entire dataset are shown in Figure 5.5 for six categories: (a) all days with shorelines, (b) days with megacusp presence, (c) megacusp formation moments, (d) days without megacusps, (e) days with megacusps but without crescentic bars and (f) megacusp disappearance moments. A comparison of the wave direction distribution during presence, formation and disappearance of megacusps and crescentic bars is shown in Figure 5.6. Time series showing an overview of all megacusp and crescentic bar data during

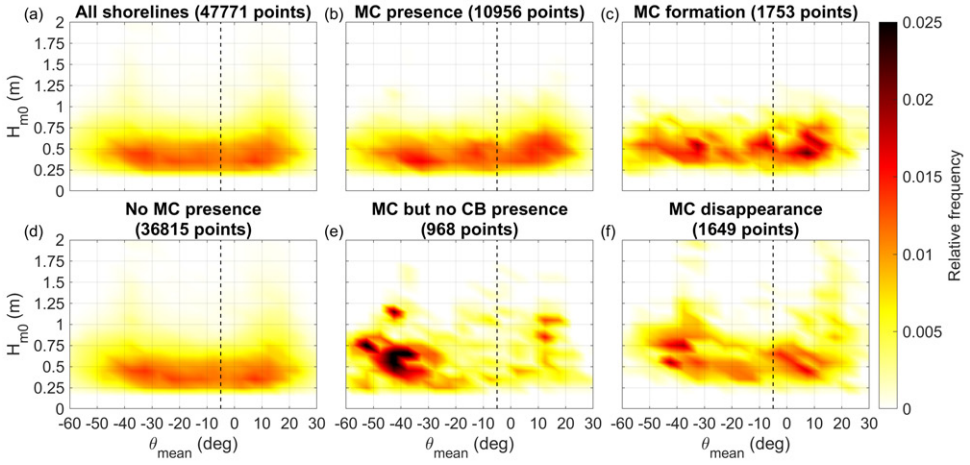

Figure 5.5 2D histograms of hourly significant wave height H_{m0} versus hourly mean wave direction θ_{mean} from shore normal (positive for westerly waves) at 10-m depth for different categories (MC denotes megacusp and CB denotes crescentic bar). Only data from the SWAN simulation forced with 2D spectra is shown and waves with H_{m0} < 0.2 m are excluded. The dashed vertical line is the separation between easterly and westerly waves.

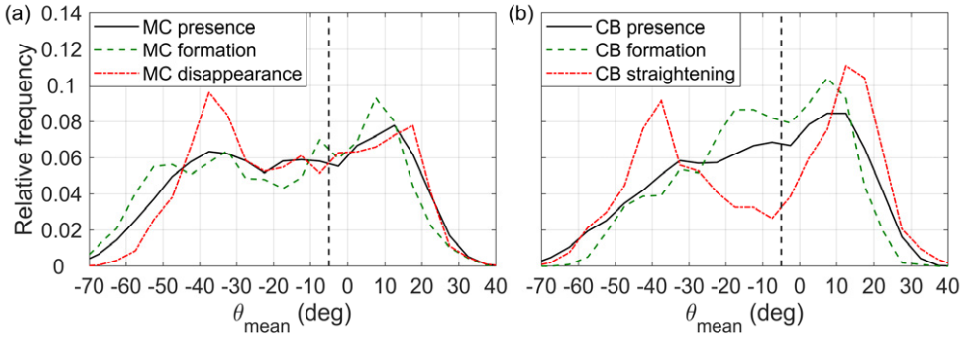

Figure 5.6 Distributions of θ_{mean} at 10-m depth during (a) megacusp presence, formation and disappearance and (b) crescentic bar presence, formation and straightening (taken from Figure 4.16). Only data from the simulation forced with 2D spectra is shown and waves with $H_{mo} < 0.2$ m are excluded. The dashed vertical line is the separation between easterly and westerly waves.

the entire study period are shown in Figure 5.7, whilst a representative nearly 2-months period with both megacusp events and crescentic bar events is shown in Figure 5.8. A selection of planviews corresponding to this period is shown in Figures 5.2e-h and 5.1.

Figure 5.5a highlights that the entire study period was characterised by mostly calm wave conditions with a large variety in wave angles. The range in wave angles is similar for all categories in Figure 5.5, whilst some differences in wave height exist between the different categories. Similar wave conditions prevailed when no megacusps were present (Figure 5.5d), but also during megacusp presence (Figure 5.5b) and during megacusp formation (Figure 5.5c). The main difference is that high-energetic waves were completely absent during megacusp presence and megacusp formation. In fact, megacusps typically developed at the study site during periods with relatively low-energetic wave conditions and a large range of incidence angles following a short period with higher energetic wave conditions (e.g., Figure 5.8 on 21 and 27 March 2015). Higher energetic waves were present during megacusp disappearance (Figure 5.5f), although the wave angles were less oblique compared to megacusp formation. Furthermore, both low and high-energetic waves with strong oblique angles (showing a clear dominance of easterly waves) were observed when megacusps were present but crescentic bars were absent (Figure 5.5e), although this only occurred sporadically. Generally, no clear

Table 5.2 Overview for all megacusp events of the differences between (1) the day of megacusp (MC) formation and the closest day of crescentic bar (CB) formation; (2) the day of megacusp disappearance and the closest day of crescentic bar disappearance; and (3) the days with megacusp presence and the closest day of crescentic bar presence. Results were grouped into bins according to the number of days difference (positive value indicates CB preceded MC) that were subsequently converted to percentages.

Category	Number of days difference						
	MC prior to CB					CB prior to MC	
	≤ -3	-2	-1	0	1	2	≥ 3
Formation	5	0	2.5	5	12.5	11.3	63.7
Disappearance	18.3	4.9	8.5	32.9	15.9	7.3	12.2
Presence	1.5	0.3	0.5	91.2	2.1	1.5	2.9

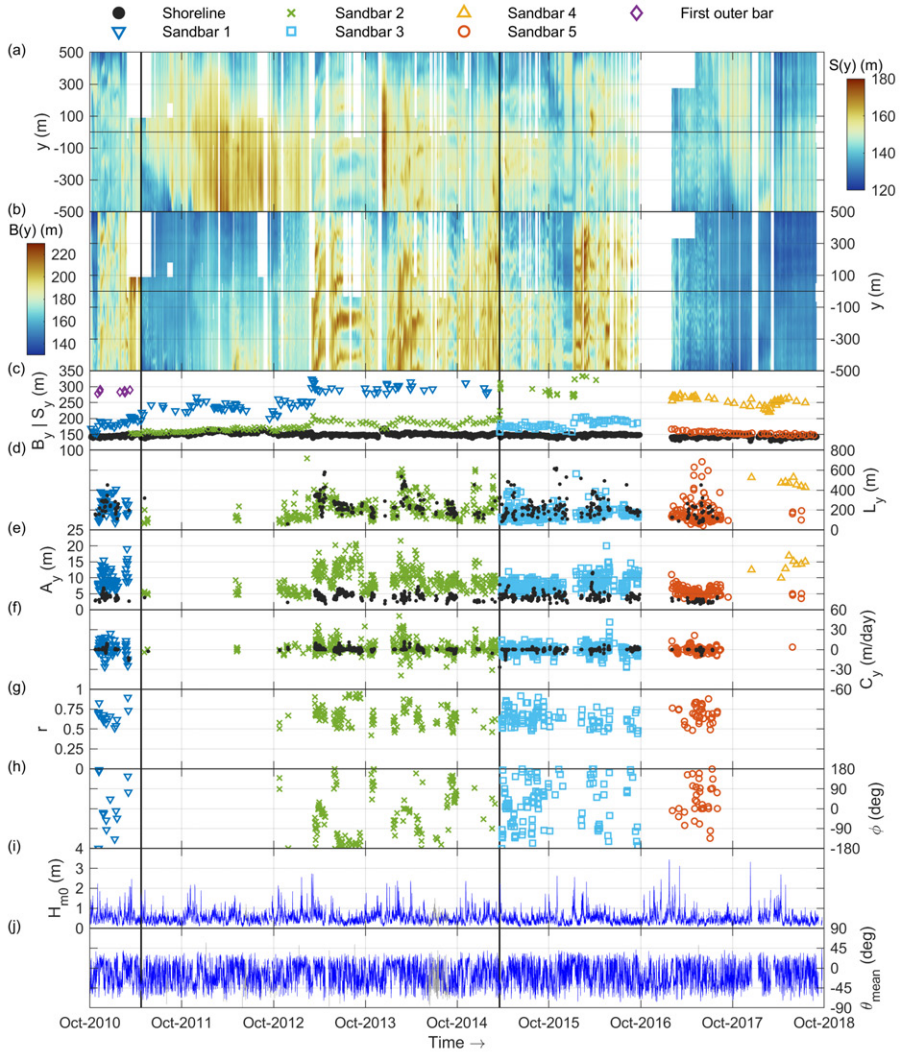

Figure 5.7 The (a) cross-shore shoreline positions (with respect to the camera tower) S at alongshore position y (timestack), (b) cross-shore bar crest positions (with respect to the camera tower) B at alongshore position y of the bar closest to shore (timestack), (c) alongshore-averaged bar crest and shoreline positions B_y and S_y, (d) alongshore-averaged wavelength L_y, (e) alongshore-averaged amplitude A_y, (f) average migration speed C_y (positive for eastward migration), (g) max correlation r for all moments with significant correlation (98% confidence level) between crescentic bars (inner bar) and megacusps, (h) phase ϕ between crescentic bars (inner bar) and megacusps corresponding to r, (i) significant wave height H_{mo} and (j) mean wave direction θ_{mean} from shore normal (positive for westerly waves) versus time at Castelldefels beach. Different sandbars in panel (b) are separated by black vertical lines. To increase readability, only a selection of data points of sandbars 1-5 are shown in panel (e). Panels (i) and (j) display all hourly wave conditions (at 10 m depth without threshold in H_{mo}) and the colours denote the SWAN boundary conditions: 2D spectra (blue) or integrated wave parameters (grey).

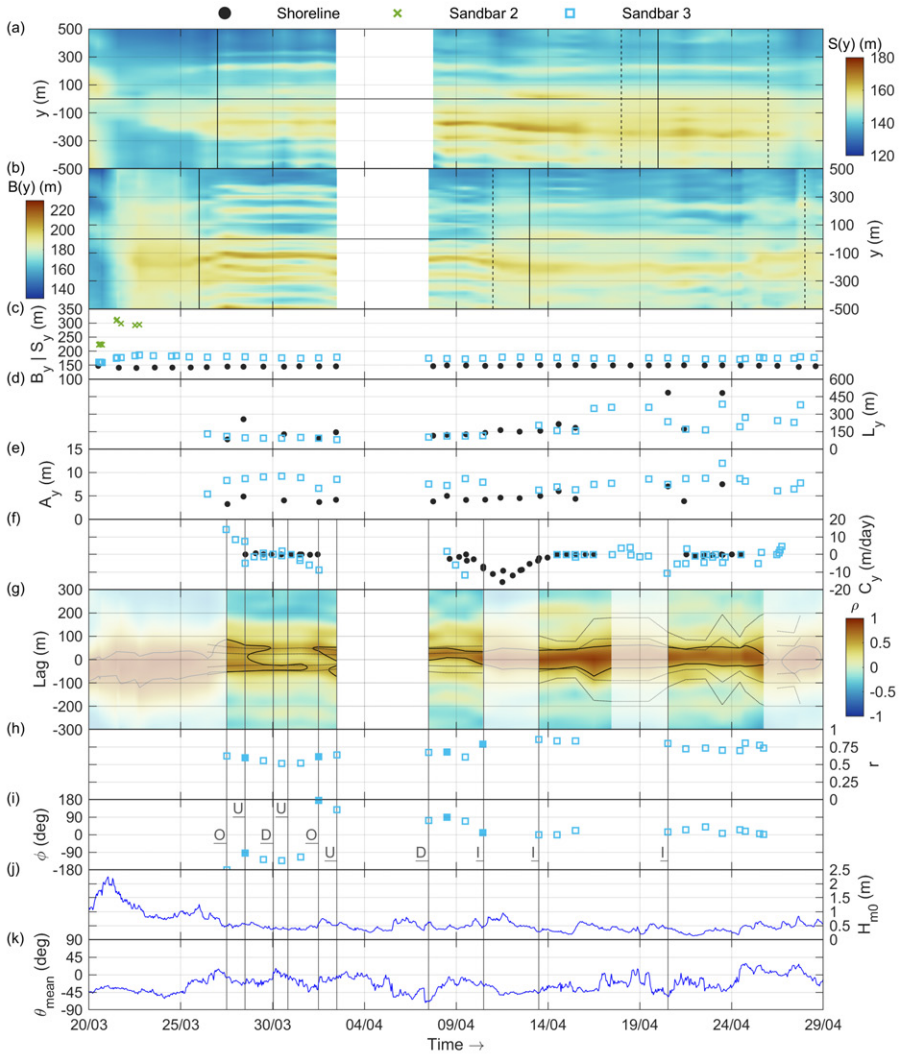

Figure 5.8 Nearly identical to Figure 5.7, but now for a period with sandbar-shoreline coupling in March-April 2015. Panels (a)-(f) are identical to Figure 5.7, whereas panels (h)-(k) correspond to panels (g)-(j) in Figure 5.7. Panel (g) shows a timestack of cross-correlation ρ between the inner sandbar and shoreline for different lags (transparent parts indicate periods without crescentic bars and/or megacusps). The black contours in panel (g) indicate the 98% confidence level for statistically significant coupling and the dashed lines indicate $\pm 0.25 L_{y,CB}$ and $\pm 0.5 L_{y,CB}$ ($L_{y,CB}$ being the crescentic bar wavelengths). The solid (dashed) vertical lines in panels (a) and (b) indicate the start (end) of a megacusp/crescentic bar event. Furthermore, the grey vertical lines in panels (f)-(k) denote changes in the observed coupling pattern, with the letters in panel (i) denoting the coupling type (O for out of phase coupling, U for upwave coupling, D for downwave coupling and I for in phase coupling). Finally, the filled squares in panels (h) and (i) correspond to the days of the planviews shown in Figure 5.2.

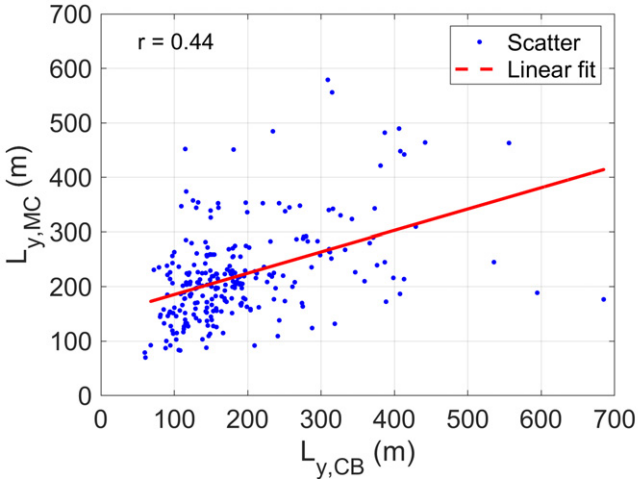

Figure 5.9 Megacusp wavelengths $L_{y,MC}$ plotted versus the crescentic bar wavelengths $L_{y,CB}$ including linear fit and Pearson correlation coefficient. Only moments with significant sandbar-shoreline coupling (98% confidence interval) are shown.

relation between megacusp dynamics and wave conditions can be deduced from Figure 5.5. Conversely, crescentic bar dynamics depended strongly on the wave conditions, such as the wave height and especially the wave angle (Chapter 4). A clear dominance of shore-normal waves was observed during crescentic bar formation, whilst oblique waves were dominant during crescentic bar straightening (Figure 5.6b). In contrast, the wave angles during megacusp formation and disappearance were not that different (Figure 5.6a).

The analysis in Section 5.3.1 already indicates that crescentic bar presence played a major role in megacusp formation. This is further supported by Table 5.2, which describes the number of days between megacusp and crescentic bar formation (positive numbers indicate a crescentic bar existed before a megacusp formed), and similarly for disappearance and presence. As shown in the first row of Table 5.2, megacusps mostly formed some days after the formation of a crescentic bar (e.g., Figure 5.8a,b on 26 and 27 March 2015), although megacusps sometimes developed halfway through a long-lasting crescentic bar event (e.g., Figure 5.8a,b on 19 April 2015). Generally, the megacusps persisted during calm wave conditions for as long as the crescentic bars remained (bottom row of Table 5.2). Megacusp disappearance often occurred simultaneously with crescentic bar straightening (particularly during high-energetic storms), although megacusps often also disappeared a few days before or after straightening of a crescentic bar during lower-energetic wave conditions (middle row of Table 5.2). Very low-energetic wave conditions led to bar arrestment (no morphological changes in the sandbars), during which only diffusion caused some small-scale morphological changes at the shoreline. One such period occurred in summer 2013 (Figure 5.7a,b).

5.3.3 Megacusp shape and migration

Throughout the study period, megacusp characteristics were very variable (Figure 5.7d-f) and could also fluctuate substantially within the same event (Figure 5.8d-f). Megacusp wave-

lengths were generally quite similar to the crescentic bar wavelengths (Figure 5.7d and Table 5.1), although substantial deviations could sometimes occur. In the first days of megacusp events, the wavelengths often deviated from the crescentic bar wavelengths (Figure 5.8d on 28 March 2015 and 20 and 23 April 2015). Observed megacusps wavelengths can sometimes be larger than those of the crescentic bars because megacusps are generally much more subtle and thus more difficult to detect (especially at the start and end of megacusp events). As a result, megacusp wavelengths were sometimes even unavailable during megacusp events (e.g., Figure 5.8d on 29 March 2015, 16 and 22 April 2015). In longer lasting (more than 1 week) events, the wavelengths typically became more similar to the crescentic bar wavelengths as additional megacusps developed (Figure 5.8d between 7 and 15 April 2015). At the end of megacusp events, the megacusp wavelengths often increased as smaller megacusps disappeared easier than larger megacusps. All this variability explains the scatter in Figure 5.9, although the relation is highly significant at the 99% confidence level.

The cross-shore amplitudes of the megacusps were much less variable (Figure 5.7e). At the start of megacusp events, the amplitudes were generally small (below 5 m; Figure 5.8e on 27 March 2015) and they generally slightly increased during longer-lasting events (compare the amplitudes on 30 March and 14 February 2015; Figure 5.8e). Megacusp amplitudes hardly exceeded 7 m, being much smaller than the amplitudes of crescentic bars (10–20 m; Figure 5.7e and Table 5.1).

The alongshore migration rates of the megacusps were much smaller compared to the crescentic bar migration rates (Figure 5.7f and Table 5.1). Megacusps generally migrated with a

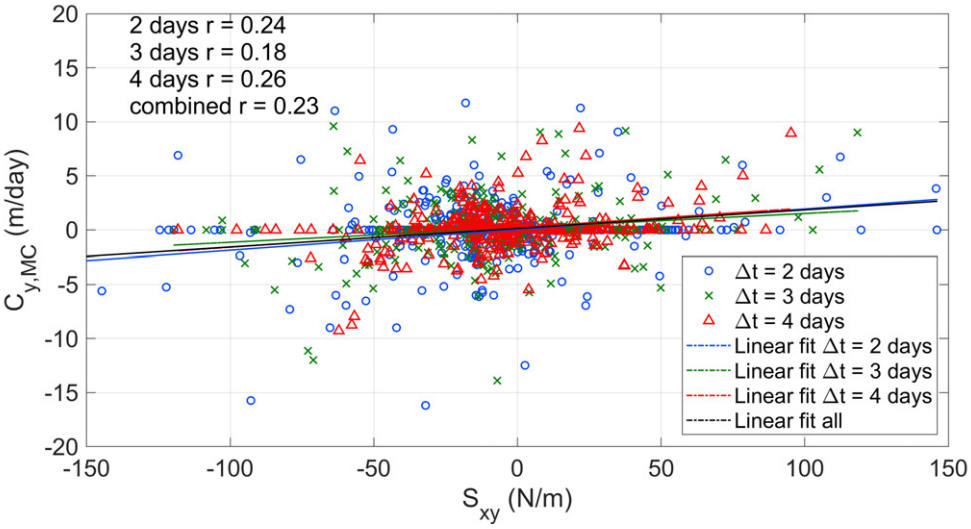

Figure 5.10 Average megacusp migration rate $C_{y,MC}$ (positive for eastward migration) versus radiation stress S_{xy} (positive for waves coming from the west). Linear fits and the corresponding Pearson correlation coefficients are also included. The different colours indicate the time period over which the migration speed was computed. For each migration speed, S_{xy} was averaged over the corresponding time period. When computing S_{xy}, the bias in wave direction was compensated by adding 5° to the wave angles (see Section 5.2.4).

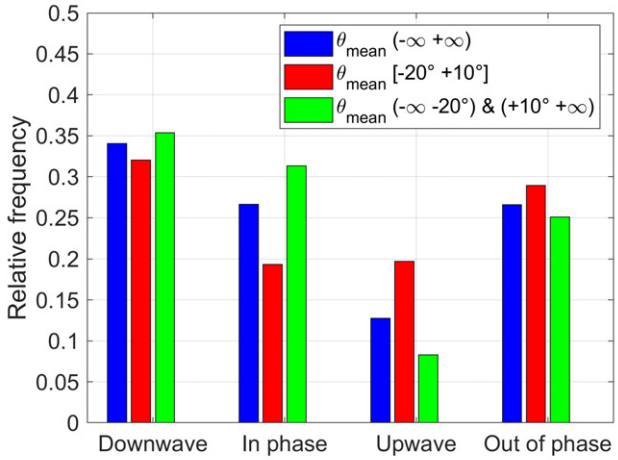

Figure 5.11 Distribution of the different coupling patterns (see Figure 5.2 and Section 5.2.3) during the entire study period for different intervals in mean wave direction θ_{mean}.

certain time lag in response to crescentic bar migration (Figure 5.8f between 9 and 14 April 2015), with migration rates of mostly only a few metres per day that rarely reached more than 10 m/day. No clear relation exists between the megacusp migration rates and the radiation stress S_{xy} (Figure 5.10). Often, no migration was observed for large S_{xy} values resulting in small correlation coefficients. This trend is independent of the time period that was used to compute the migration rates (see Section 5.2.2).

5.3.4 Crescentic bars and megacusps coupling

Two findings that indicate that the inner crescentic bar and the observed megacusps were morphologically coupled are the observed link between megacusp development and crescentic bar presence (Section 5.3.2), along with the relation between megacusp and crescentic bar wavelengths (Section 5.3.3). More evidence was obtained by computing the cross-correlation

Table 5.3 Mean values of significant wave height H_{mo} and alongshore-averaged bar-shoreline distance D_y for the 4 distinguished coupling patterns. Values are given for 3 ranges in mean wave direction θ_{mean}: all angles ($-\infty \leq \theta_{mean} \leq +\infty$) , shore-normal angles ($-20^\circ \leq \theta_{mean} \leq +10^\circ$) and oblique angles ($\theta_{mean} < -20^\circ$ & $\theta_{mean} > +10^\circ$). Statistics are computed using the simulation forced with 2D spectra and excluding waves with $H_{mo} < 0.2$ m.

Parameter	θ_{mean} range	Coupling patterns Downwave	In phase	Upwave	Out of phase
H_{mo}	$(-\infty, +\infty)$	0.49	0.57	0.52	0.47
	$[-20^\circ, +10^\circ]$	0.54	0.58	0.54	0.48
	$(-\infty, -20^\circ)$ & $(+10^\circ, +\infty)$	0.48	0.57	0.53	0.47
D_y	$(-\infty, +\infty)$	31	33	32	34
	$[-20^\circ, +10^\circ]$	36	38	35	34
	$(-\infty, -20^\circ)$ & $(+10^\circ, +\infty)$	30	32	33	35

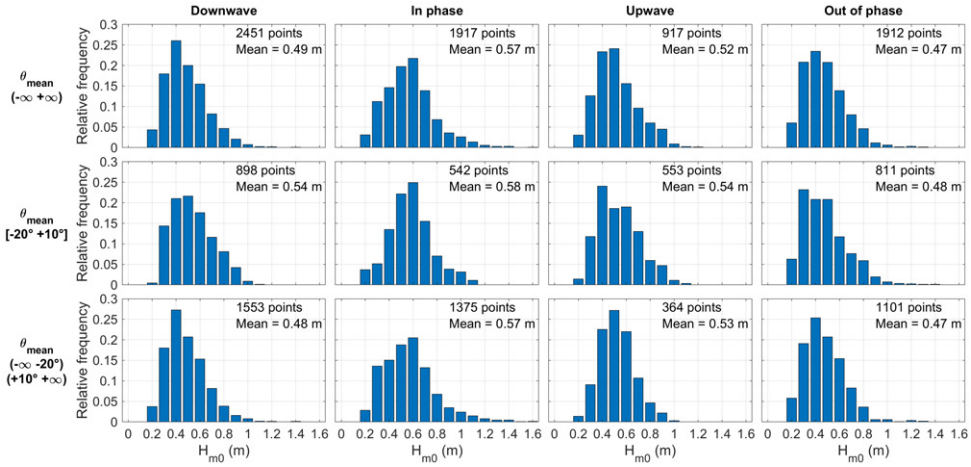

Figure 5.12 Histograms of the significant wave height H_{mo} for the 4 different coupling patterns and the 3 ranges in wave angle θ_{mean}. Only data from the simulation forced with 2D spectra is used and low-energetic wave conditions (H_{mo} < 0.2 m) are excluded.

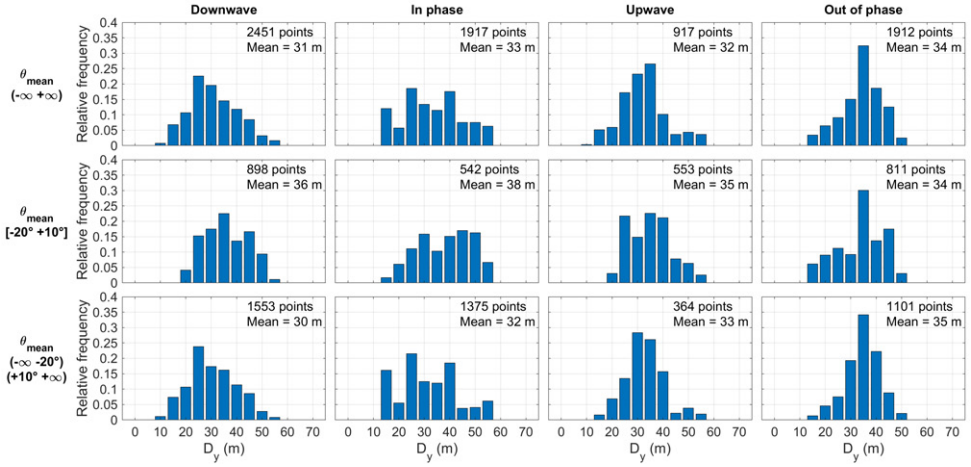

Figure 5.13 Identical to Figure 5.12, but now showing histograms of bar-shoreline distance D_y.

coefficient ρ (section 5.2.3). Throughout the days with simultaneous presence of megacusps and crescentic bars (22% of the study period), the coupling was significant at the 98% confidence level during 74% of the time. Altering the confidence level to 95% or 90% did not cause notable changes to the results.

At Castelldefels, a broad range of coupling patterns was observed during the days with significant coupling (blue bars in Figure 5.11). The coupling type also partially depended on the wave height and angle. Taking into account all wave directions (blue bars in Figure 5.11), downwave coupling was most prominent (34% of the time), followed closely by in phase and out of phase coupling (both 27% of the time), whilst upwave coupling was observed less

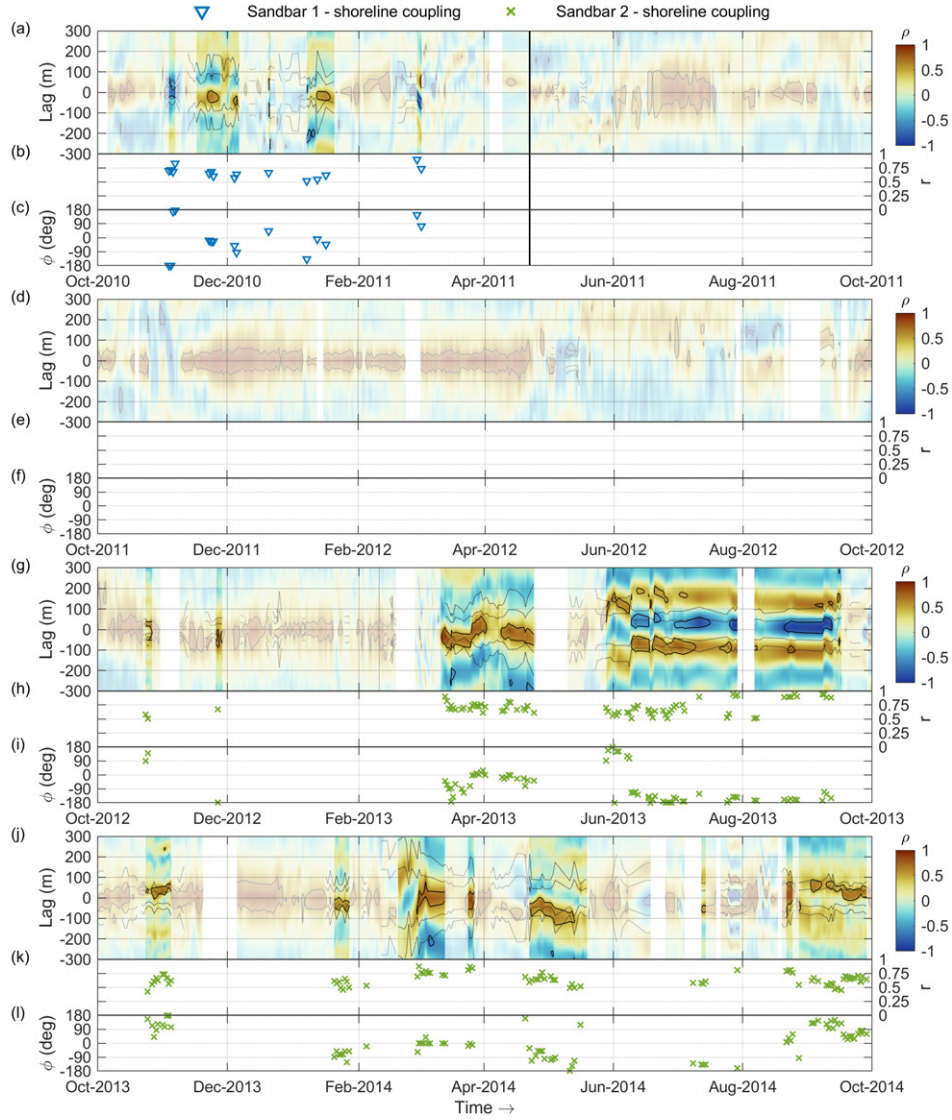

Figure 5.14 Overview of the morphological coupling between the inner sandbar and shoreline for the first 4 years of the study period (October 2010–October 2014). Panels (a), (d), (g) and (j) show the timestacks of the cross-correlation ρ between the inner sandbar and shoreline versus lags for the different years (transparent parts indicate periods without crescentic bars or megacusps), whereas the black contours indicate the 98% confidence level for statistically significant coupling and the dashed lines indicate $\pm 0.25 L_{y,cb}$ and $\pm 0.5 L_{y,cb}$ ($L_{y,cb}$ being the crescentic bar wavelength). Panels (b), (e), (h) and (k) show the max correlation r for all moments with significant correlation (98% confidence level) between crescentic bars (inner bar only) and megacusps for the different years and panels (c), (f), (i) and (l) show phase ϕ corresponding to r. Black vertical lines indicate moments where a new inner sandbar has formed.

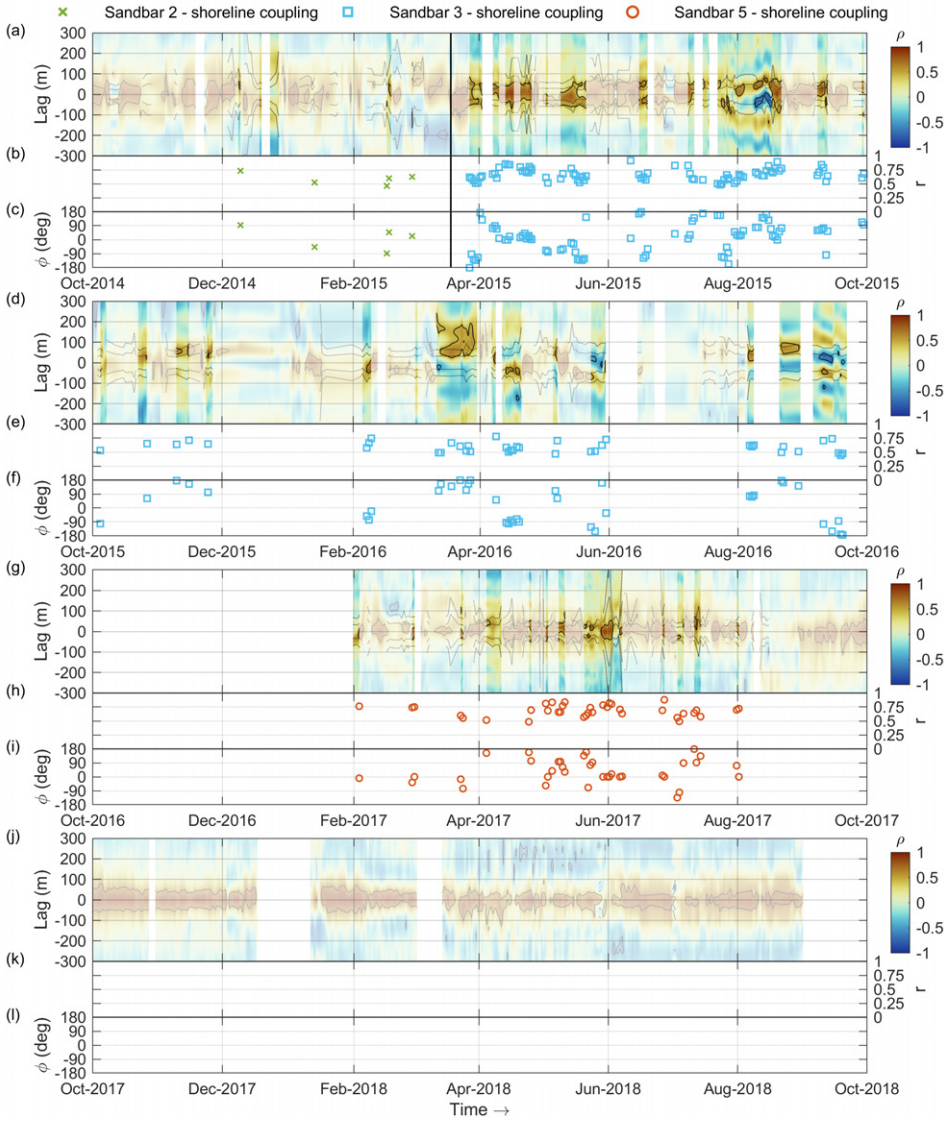

Figure 5.15 Identical to Figure 5.14, but now for the period October 2014–October 2018.

frequently (13% of the time). A similar distribution in coupling patterns was observed for oblique waves (green bars in Figure 5.11). Conversely, upwave coupling occurred as frequently as in phase coupling during shore-normal waves (20% of the time; red bars in Figure 5.11), although downwave and out of phase coupling (both about 29% of the time) were still the most common. In phase coupling was mostly observed for higher-energetic waves, whilst out of phase coupling occurred mostly during lower-energetic waves (Table 5.3 and Figure 5.12). Intermediate wave conditions were dominant during upwave and downwave coupling.

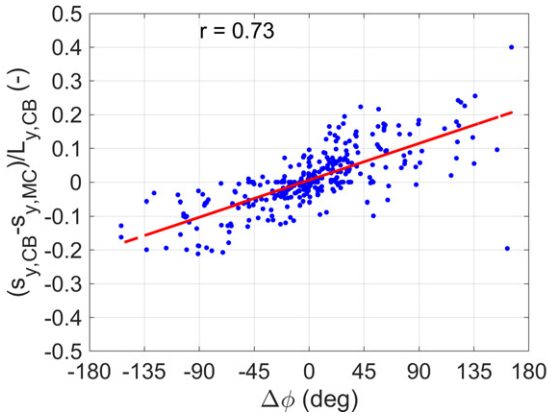

Figure 5.16 Scatterplot of difference between crescentic bar and megacusp displacements (normalised using crescentic bar wavelengths $L_{y,CB}$) versus difference in phase ϕ. Linear fit and the corresponding Pearson correlation coefficient are also included.

No clear relation was observed between the different coupling patterns and the bar-shoreline distance (Table 5.3 and Figure 5.13).

An example of a cross-correlogram showing clear sandbar-shoreline coupling is shown in Figure 5.8g for the period March-April 2015 (the cross-correlograms of the entire study period are shown in Figures 5.14 and 5.15). Coupling periods during the study period were often characterised by substantial changes in phase ϕ (Figures 5.8i, 5.14 and 5.15). Changes in phase were linked to a displacement of the crescentic bar with respect to the megacusps (Figure 5.16). This is clear for the time period shown in Figure 5.8. Particularly during the first and second coupling period (27 March-2 April 2015 and 7-10 April 2015), migration of the crescentic bar caused several changes in the coupling pattern (Figure 5.8f,i). The last two coupling periods showed very little migration of the crescentic bars and megacusps (probably due to the prevailing low-energetic wave conditions; Figure 5.8f,j on 13-17 and 20-25 April 2015), which resulted in continuous in phase coupling during both periods (Figure 5.8i).

5.4 Discussion

5.4.1 Accuracy of megacusp detection

Analogous to the detection of crescentic bar events in Chapter 4, the megacusp events in this study were detected visually by two experienced researchers to avoid prejudice and increase accuracy. However, previous studies often used the standard deviation (σ; e.g., Rutten et al., 2018) or sinuosity (*Sin*; Ojeda et al., 2011) to detect alongshore variability in the barline or shoreline. In order to check whether these parameters could be used in the present study for the detection of megacusps, the standard deviations and sinuosities of the shoreline (σ_S and Sin_S, respectively) were obtained for all days with and without visually detected megacusps (Figure 5.17). Comparing the two parameters shows that Sin_S is a better proxy for megacusp presence compared to σ_S, but there is a range in Sin_S (1.002–1.003) where this parameter

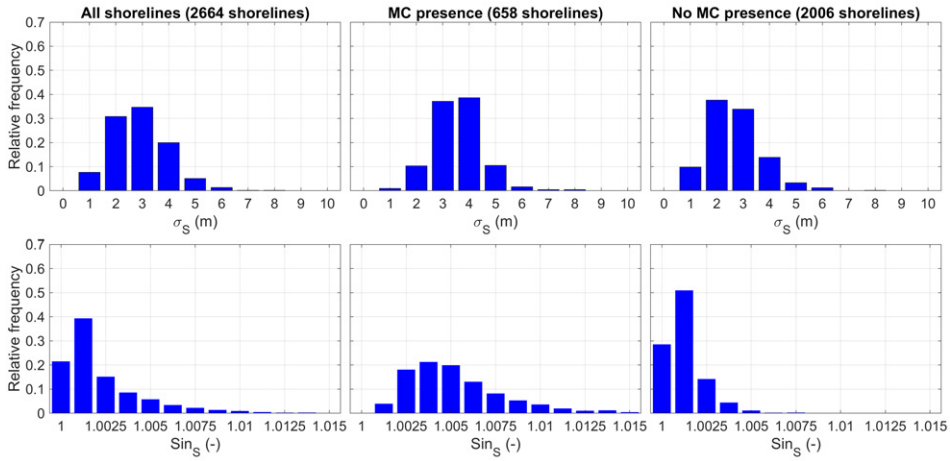

Figure 5.17 Histograms of the standard deviation of the shoreline σ_S (top) and the sinuosity of the shoreline Sin_S (bottom) for all shorelines (left), all shorelines with visually detected megacusps (middle) and without visually detected megacusps (right).

is indecisive. To obtain maximum accuracy, it was decided to use the visual analysis in the present study.

Compared to crescentic bars, shoreline undulations were generally less pronounced (particularly in cross-shore amplitude). Megacusp formation moments were not easy to detect as they often took more than one day, but the subtlety of the shoreline undulations made detection even more challenging. Conversely, detecting megacusp disappearance moments was generally easy when they were a result of wave activity as they usually occurred within one day. However, diffusion of megacusps during prolonged periods with low-energetic waves was more challenging because this generally occurred over several days. The small amplitude of the megacusps could also partly explain why the sign of the cross-correlation did not always correctly discriminate between in phase and out of phase coupling (Section 5.2.3).

5.4.2 Megacusp characteristics and dynamics

At Castelldefels, no clear relation was observed between megacusp dynamics and wave conditions. Low-energetic waves with a large variety in wave angles prevailed during megacusp presence/formation/absence (Figure 5.5b,c,d), whilst megacusp disappearance occurred both during high and low-energetic waves with a similar variation in wave direction (Figure 5.5f). In agreement with the Castelldefels observations, several previous studies observed megacusp formation during lower-energetic conditions (e.g., Segura et al., 2018). Similarly, Segura et al. (2018) also observed megacusp disappearance during storms as well as during extended periods of low energy waves, whilst other studies (e.g., Birrien et al., 2013; Castelle et al., 2019) mainly observed accretive megacusps (located at the shoreline and similar to the Castelldefels megacusps) to disappear during storms. Conversely, some other studies at higher energetic coasts observed megacusps to persist during storm conditions (Aagaard et al., 2005; Quartel, 2009) and Castelle et al. (2019) even observed that large erosive megacusps (located at the dune foot and causing local dune erosion) formed during storms.

Megacusps at the study site displayed a wide variety in wavelengths (between 100 and 700 m; Figure 5.7d), whilst the amplitudes were less variable (generally between 3 and 7 m; Figure 5.7e). Compared to most previous megacusp observations (Table 5.4), the Castelldefels megacusps displayed relatively small wavelengths. As will be discussed in the next section, megacusp wavelengths are strongly related to those of crescentic bars, which in turn are smaller, probably due to the mostly low-energetic waves at the study site. However, Table 5.4 also shows examples of small megacusp wavelengths in higher energetic environments (e.g., Short, 1979; Thornton et al., 2007; Van de Lageweg et al., 2013) and larger wavelengths in low-energetic environments (Balouin et al., 2013). These variations in crescentic bar and

Table 5.4 Overview of previous observations of megacusps coupled to crescentic bars. Site and megacusp characteristics are shown, as well as the dominant coupling pattern. Mean values are shown except tides (spring tidal range), C_y (absolute mean value and range) and coupling pattern (++ for in phase coupling, −− for out of phase coupling and +− for a mix of in phase and out of phase coupling).

Site	Tide [m]	H_{mo} [m]	$L_{y,MC}$ [m]	$A_{y,MC}$ [m]	$C_{y,MC}$ [m/day]	Coupling pattern	Study period	Reference
Cape Hatteras, USA[1]	1.1	1.3	550	10	5 (0–7)	−−	3 years[d]	Dolan (1971)
Various, USA[1]	-	-	-	-	-	−−	Variable[d]	Sonu (1973)
Various, USA[2]	-	-	-	-	-	++	Variable[d]	Sonu (1973)
White Park Bay, Northern Ireland[1]	1.8	1.4	-	-	-	−−	≈5 years[b,d]	Carter and Kitcher (1979)
Various, Australia[1]	≈1.6	≈1.8	≈200	-	-	−−	>2 years[b,d]	Short (1979)
HaHoterim, Israel[1]	0.6	1.2	-	-	-	−−	8 months[d]	Goldsmith et al. (1982)
HaHoterim, Israel[2]	0.6	1.2	-	-	-	++	8 months[d]	Goldsmith et al. (1982)
Various, Israel[1]	0.6	1.1	-	-	-	−−	32 years[d]	Bowman and Goldsmith (1983)
Hald, Denmark[1]	0.4	0.7	120	-	-	−−	5.5 months[b]	Aagaard (1988)
Various, Egypt[1]	≈0.3	≈1.1	125	-	-	−−	unknown[b,d]	Nafaa and Frihy (1993)
Monterey Bay, USA[1]	1.6	≈2.0	200	-	- (0–3.4)	−−	>2 years[b,d]	Thornton et al. (2007)
Hasaki, Japan[1]	1.4	1.35	550	-	- (0–18)	−−	2 years[a]	Galal and Takewaka (2008)
Noordwijk, Netherlands[1]	1.8	≈1.0	243	-	≈3.5 (0–36)	+−	15 months[a]	Quartel (2009)
Monterey Bay, USA[1]	1.6	≈2.0	≈300	-	- (-)	+−	1–3 years[a]	Orzech et al. (2011)
Sète, France[1]	0.3	0.7	400	-	- (-)	−−	8 months[a,b]	Balouin et al. (2013)
Anglet, France[1]	3.9	1.6	450	≈15	- (-)	−−	18 months[a]	Birrien et al. (2013)
Tairua, New Zealand[1]	2.0	1.1	≈300	-	- (-)	+−	7 years[a]	Van de Lageweg et al., (2013)
Truc Vert, France[1]	5.0	1.8	400	10	2 (-)	++	12.5 years[b,c]	Castelle et al. (2015) and Castelle et al. (2019)
Truc Vert, France[3]	5.0	1.8	800	10	- (-)	−−	12.5 years[b,c]	Castelle et al. (2015) and Castelle et al. (2019)
Anmok, South Korea[1]	0.3	1.1	-	15	- (-)	+−	3 years[c]	Athanasiou et al. (2018)
Zandmotor, Netherlands[1]	1.7	1.0	-	-	- (-)	−−	2.4 years[a,b]	Rutten et al. (2018)
Secret Harbour, Australia[1]	<0.5	≈0.8	150	3	- (0–20)	−−	2 years[a,b]	Segura et al. (2018)
Sylt, Germany[1]	2.0	≈0.9	2240	-	- (-)	−−	40 years[b]	Gijsman et al. (2021)
Castelldefels, Spain[1]	0.2	0.6	230	4	1.1 (0–15)	+−	≈8 years[a]	This study

Coupling detail: [1]Shoreline-inner bar; [2]Shoreline-outer bar; [3]Dunefoot-outer bar
Main dataset: [a]Video data; [b]Bathymetric data; [c]Satellite data; [d]Aerial photos

megacusp wavelengths could also be related to variations in the bar-shoreline distance (see Chapter 4). Megacusp migration rates at Castelldefels could reach 15 m/day, but were generally small (often even zero; Figure 5.7f). Previous studies observed fairly similar migration rates (Table 5.4) and megacusps were often also reported to be stationary (e.g., Galal and Takewaka, 2008; Segura et al., 2018). Megacusp migration at Castelldefels was not clearly linked to the radiation stress S_{xy} (Figure 5.10), which is another indication that waves are not the main driver of megacusp dynamics. This result might be site-dependent since Galal and Takewaka (2008) found a strong relation between alongshore currents and megacusp migration at their study site.

5.4.3 Megacusp-crescentic bar coupling

At the study site, megacusp development was strongly linked to crescentic bar presence. Megacusps generally developed a few days after the formation of a crescentic bar (first row of Table 5.2) and crescentic bars were present during most megacusp events (Table 5.1). This important role of sandbar geometry on shoreline dynamics and the resulting morphological coupling between megacusps and crescentic bars were observed by several previous studies (Table 5.4). Megacusps were typically coupled to the inner bar geometry, although some studies observed that the outer bar also affected the shoreline geometry (Table 5.4). Please note that the coupling patterns mentioned in Table 5.4 use the definitions of Figure 5.2. In phase, out of phase and downwave coupling occurred frequently at Castelldefels for all ranges in wave angle (Figure 5.11), whereas upwave coupling was only common for wave angles close to shore-normal. Previous studies mostly only distinguished between in phase and out of phase coupling, where out of phase coupling between the inner crescentic bars and megacusps was observed most frequently (Table 5.4) and is also the dominant coupling pattern in the beach classification scheme of Wright and Short (1984). Conversely, coupling between outer crescentic bars and megacusps was mostly reported to be in phase (e.g., Sonu, 1973).

During periods with significant sandbar-shoreline coupling at Castelldefels, the phases were often highly variable (Figures 5.8i, 5.14 and 5.15). This was linked to differential alongshore displacements of the crescentic bar with respect to the megacusps (Figure 5.16), since megacusps generally migrated much slower than crescentic bars (Figure 5.7f). Previous studies also reported that changes in phase were mainly related to different migration rates of the bar and shoreline (e.g., Quartel, 2009) and migration rates of crescentic bars were larger compared to those of megacusps (e.g., Balouin et al., 2013). Birrien et al. (2013) also observed that megacups were not able to swiftly adapt to quick alongshore migration of a crescentic bar.

5.4.4 Interpretation of coupling patterns

Not many studies investigated what physical processes caused different coupling patterns between megacusps and inner crescentic bars, although there are a few modelling studies that obtained enlightening results. Calvete et al. (2005) obtained megacups-like bedforms in the inner surf zone that were out of phase with the crescentic bars, which they attributed to the presence of a double rip cell circulation pattern (consisting of rip cells and counter-rotating cells near the shoreline) that was most evident during low-energetic waves and disappeared for higher energetic waves. Coco et al. (2020) obtained both in phase and out of phase coupling between megacusps and the inner crescentic bar (last column in their Figure 6), where out of phase coupling was accompanied by a double circulation pattern (Figure 5.18a) and a

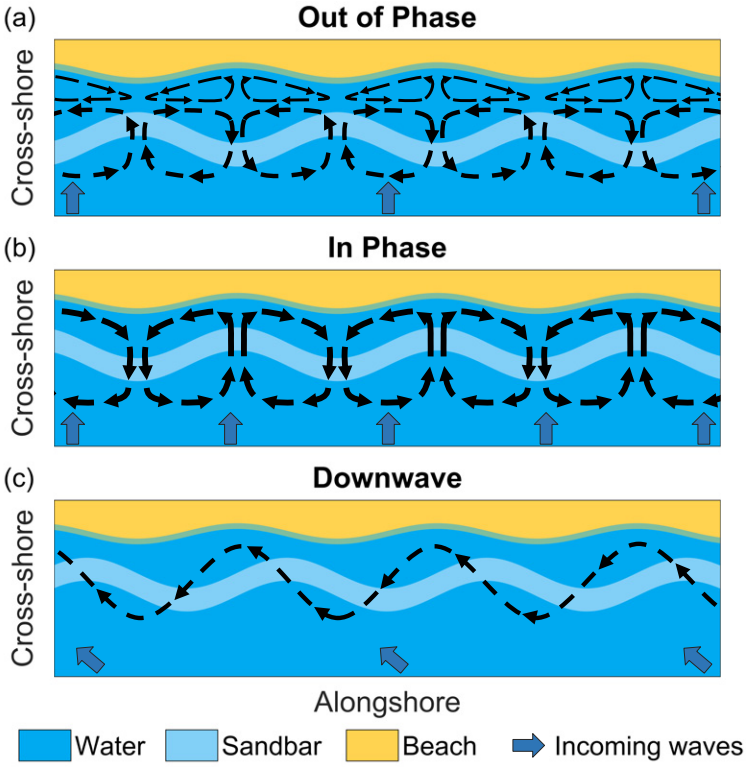

Figure 5.18 Idealised sketches of the current patterns during (a) out of phase, (b) in phase and (c) downwave coupling. For low-energetic and shore-normal waves, a double rip cell circulation is present (leading to out of phase coupling), whilst for higher-energetic shore-normal waves a single rip cell develops (generating in phase coupling). For low-medium energetic waves with strong oblique angles of incidence, a meandering alongshore current develops leading to downwave coupling. Panels (a) and (b) are inspired by the studies of Calvete et al. (2005) and Coco et al. (2020) and panel (c) is inspired by Sonu (1972).

single circulation cell was present during in phase coupling (Figure 5.18b). Finally, Orzech et al. (2011) reported that in their model results in phase coupling was obtained during larger waves and higher tides, whilst out of phase coupling was generally obtained for smaller tides and both smaller and larger waves. Generally, the above studies suggested that out of phase coupling develops during lower waves (favouring a double cell circulation), whilst in phase coupling develops during larger waves (favouring a single cell circulation).

At Castelldefels, out of phase (in phase) coupling was indeed observed for lower (higher) energetic waves (Table 5.3 and Figure 5.12) and similar trends were reported by other observational studies (Balouin et al., 2013; Van de Lageweg et al., 2013). However, Orzech et al. (2011) observed (contrary to their modelling results) that in phase coupling was mostly present during small waves and higher tides, whilst out of phase coupling occurred during larger waves and smaller tides. According to Van de Lageweg et al. (2013), the type of coupling pattern might also be affected by the bar-shoreline distance. Their results are coherent

with the discussion in the previous paragraph as a double (single) cell circulation can intuitively develop more easily when the bar is located far from (close to) shore, which leads to out of phase (in phase) coupling. However, this was not evident in our observations at Castelldefels (Table 5.3 and Figure 5.13) because the average distances were much smaller (30–40 m) and more constant.

The most interesting result from Figure 5.11 is the abundance of downwave and the absence of upwave coupling (particularly during oblique waves). Since previous studies mostly only discriminated between in phase and out of phase coupling, it is generally unknown if a similar tendency also occurred at other beaches. A possible explanation for the development of downwave coupling is that the alongshore current generated by sufficiently oblique waves overwhelms the rip cell circulation patterns (Sonu, 1972; MacMahan et al., 2010), leading to a meandering alongshore current across the crescentic inner bar that is directed shoreward (seaward) at the inner bar horns (bays). At the location where this meandering current reaches a position closest to shore it may erode part of the shoreline and form a megacusp embayment downdrift of the crescentic bar horn resulting in downwave coupling (Figure 5.18c; see also Figure 1 of Sonu, 1972). Consistent with this explanation are the often strong oblique wave angles at Castelldefels that might drive such a meandering current, leading to very frequent downwave coupling. Furthermore, similar downdrift coupling patterns were already observed between the outer and inner crescentic sandbar at the Gold Coast (horn of inner bar located downdrift of horn outer bar; Ruessink et al., 2007; Price and Ruessink, 2013), that were also linked to meandering currents as a result of dominant oblique wave angles. A subsequent modelling study (Price et al., 2013) confirmed that meandering alongshore currents indeed resulted in this downwave coupling pattern. Even though the Gold Coast studies concerned coupling between outer and inner crescentic bars, there is no reason why the above described mechanism cannot occur in situations with coupling between inner crescentic bars and megacusps.

5.5 Conclusions

Megacusp dynamics and their coupling with crescentic bars were studied at the open, fetch-limited beach of Castelldefels (northwestern Mediterranean Sea) using nearly 8 years of daily video images and propagated directional wave conditions (at 10 m depth). Megacusp formation and straightening moments were detected and the environmental conditions during these moments were analysed in detail. During the study period, the alongshore-averaged shoreline retreated by about 8 m and 67 megacusp events were identified that lasted 706 days (24% of the time). Megacusp events varied in duration from days to months and occurred irregularly over the different years. Crescentic bars were present during 91% of the days with megacusps whilst megacusps were only present during 50% of the days with crescentic bars, indicating that megacusps require the presence of a crescentic bar.

No clear relation between wave conditions and megacusp dynamics was observed, as similar wave conditions (low-energetic waves with a wide variety in direction) prevailed during megacusp formation, megacusp presence and megacusp absence. Higher energetic waves were more common during megacusp disappearance, although megacusps could also diffuse during very low-energetic wave conditions. Megacusp generally formed several days after the formation of a crescentic bar and they usually disappeared simultaneously with

crescentic bar straightening (especially during storms), although they also disappeared a few days before or after crescentic bar straightening.

A large variation in megacusp shapes was observed during the study period. Megacusp and crescentic bar wavelengths were often similar (range 100–700 m), although considerable variations could occur. The cross-shore amplitudes of the megacusps were much smaller (3–8 m) than the crescentic bar amplitudes (5–20 m) and also less variable. Compared to previous observations, the megacusps at the study site (mean wavelengths of ~230 m and mean amplitudes of ~4 m) were relatively small, which could be related to the prevailing low-energetic waves. Megacusps migrated less frequently and much slower (up to 15 m/day) compared to crescentic bars (up to 50 m/day) and megacusps mostly migrated in response to crescentic bar migration. Megacusp migration was not clearly related to the radiation stress S_{xy}.

The coupling between megacusps and crescentic bars was significant at the 98% confidence level during 74% of the time with simultaneous presence of megacusps and crescentic bars (22% of the study period). Periods with significant coupling often showed large changes in phase, which were linked to a displacement of the crescentic bar with respect to the megacusps. No dominant coupling pattern was observed at the study site, as in phase, out of phase and downwave (shoreline embayment downdrift of crescentic bar horn) coupling were regularly observed (irrespective of the wave angle), whilst upwave (shoreline embayment updrift of crescentic bar horn) coupling was only common during waves with limited obliquity. Motivated by existing modelling studies, it is hypothesised that out of phase coupling develops in the presence of a double rip cell circulation pattern, whilst in phase coupling develops when a single rip cell circulation is present. The prominence of downwave coupling and absence of upwave coupling is hypothesised to be related to obliquely incident waves driving a meandering alongshore current over the inner crescentic bar. This current causes shoreline erosion downdrift of the inner crescentic bar horn, forming a megacusp embayment and leading to downwave coupling.

Chapter 6 | Synthesis

Nearshore morphodynamic patterns have fascinated nearshore scientists for decades. As a result, many studies investigated the cross-shore and alongshore dynamics of sandbars using long-term bathymetric or video datasets, which resulted in a comparatively good understanding of the processes driving cross-shore sandbar migration and the development of alongshore sandbar rhythmicity, but the formation/straightening moments were typically not analysed in detail. Furthermore, the dynamics of megacusps and their coupling to crescentic bars only received relatively little attention.

The main aim of this thesis was to provide more insight in the development and interactions between crescentic bars and megacusps. Nearly 8 years of observational data were used to study the morphological evolution of the open, low-energetic, tideless beach of Castelldefels (20 km southwest of Barcelona, northwestern Mediterranean Sea). Daily time-exposure planview images with good time and space resolution of the beach and nearshore at Castelldefels (complemented by several irregular topobathymetric surveys) allowed to study changes in the coastal morphology at large time and spatial scales. Additionally, several available datasets of measured and modelled offshore wave conditions were assessed to obtain a well-validated dataset of hourly nearshore wave conditions. These datasets were subsequently used to investigate the role of the bathymetric configuration and directional wave conditions on the dynamics of crescentic bars and megacusps. Crescentic bar and megacusp events were located by detecting the formation and straightening moments, which allowed a detailed analysis of the environmental conditions during formation, evolution and straightening of crescentic bars and megacusps. Additionally, this allowed to study the importance of cross-shore dynamics on the development of crescentic bars and megacusps. Finally, the morphological coupling between crescentic bars and megacusps was studied, in particular the processes causing the emergence of different coupling patterns. Below, the main findings of this study are summarised by answering the research questions that were formulated in the Introduction (Section 1.4). Finally, some suggestions for future research are given.

6.1 Main findings

6.1.1 Which method provides optimal directional wave conditions for nearshore field studies?

Accurate nearshore directional wave conditions are critical for studying the evolution of coastal morphology and as boundary conditions for morphodynamic models. In Chapter 3, the accuracy of two large-scale global hindcast models and propagating measured offshore wave conditions using linear wave theory or the SWAN spectral wave model (forced by integrated wave parameters or 2D spectra) was evaluated for Castelldefels beach. Propagating measured wave conditions yielded the best results, although substantial differences

were observed between the different propagation methods. The largest accuracy for all wave parameters (wave height, mean wave period and mean wave direction) during all wave climates (shore-normal, shore-oblique and bimodal) was obtained by propagating measured 2D spectra with SWAN. In particular, the errors in mean wave direction were below 10° for all wave climates, which is essential when studying the evolution of nearshore morphodynamic patterns like sandbars and shoreline sand waves. Forcing SWAN with measured integrated wave parameters led to similar results for wave height and period, but errors in wave direction increased to over 20° during shore-oblique and bimodal wave climates. The reason is that a lot of valuable information is lost when transforming a full 2D spectrum into a single set of integrated wave parameters, so that the 2D spectrum reconstructed by SWAN out of the integrated wave parameters did not resemble the actual directional spectrum. This was particularly problematic during easterly and bimodal wave climates, where the 2D spectrum reconstructed by SWAN was either too wide in direction or only contained one directional peak due to limitations of the spectral function used by SWAN. Propagating the measured wave conditions with a simple wave propagation model based on ray approximation (linear wave theory) provided good results for wave height and period. However, this model assumes monochromatic waves and alongshore-uniform bathymetry, meaning that refraction of oblique waves over the alongshore-variable bathymetry was underestimated. As a result, large errors in mean wave direction (above 60°) were present for shore-oblique waves and bimodal wave climates. Furthermore, this method was not able to include all waves due to significant changes in the orientation of the shoreline between the offshore wave buoy and Castelldefels beach. Finally, global hindcast models correctly predicted the trends in wave height and mean wave period, but mean wave direction was only accurately predicted during shore-normal waves, whereas large errors (above 60°) were observed during shore-oblique waves. As a result, large-scale hindcast models are not suited for studies of nearshore morphodynamic processes in which the wave angle plays an important role.

6.1.2 What are the geomorphological characteristics of the nearshore sandbars and the shoreline at Castelldefels beach?

As described in Chapter 4, the various sandbars that were tracked during the 8-year study period were often dynamic in the cross-shore position. Both the inner and outer sandbar experienced substantial cross-shore migration (up to 70 m in one day) during several storms and subsequent slow onshore migration during post-storm conditions. Offshore migration during storms sometimes caused major changes in the sandbar configuration, such as the formation of a new inner bar and offshore migration of the original inner bar so that it became the new outer bar (causing the original outer bar to disappear from the analysis). Similar episodic net offshore migration patterns (episodic NOM) were reported by various previous studies (e.g., Ruessink et al., 2009; Melito et al., 2020). The crescentic bar characteristics during the study period were also analysed in Chapter 4 and a large variation in wavelengths (100–700 m), cross-shore amplitudes (5–20 m) and alongshore migration rates (0–50 m/day) was observed. Wavelengths varied considerably due to splitting and merging of individual crescents, but they also increased when the bar was located further from shore. The mean wavelengths and amplitudes (~200 m and ~9 m, respectively) were fairly small compared to previous studies (e.g., Van Enckevort et al., 2004), which could be a result of the generally low-energetic wave conditions (mean H_{mo} ~0.6 m) at the study site. Alongshore migration rates were usually less than 10 m/day and larger migration rates generally corresponded to well-developed crescentic bar events with large wavelengths and amplitudes.

As described in Chapter 5, a long-term cross-shore retreat of the shoreline of about 8 m was observed during the study period and the short-term variation in the alongshore-averaged shoreline position was mostly small. However, the megacusps that occurred throughout the study period displayed considerable variability in their characteristics. The megacusp wavelengths showed a range similar to those of crescentic bars (100–700 m), although substantial variations could also occur between them. In contrast, the cross-shore megacusp amplitudes (3–8 m) were much smaller and less variable compared to those of crescentic bars. Analogous to crescentic bars, the mean megacusp wavelengths and amplitudes at the study site (~230 m and ~4 m, respectively) were fairly small compared to previous studies (e.g., Balouin et al., 2013). Megacusp migration occurred less frequently and was slower compared to crescentic bars. Megacusps generally migrated only a few metres per day and typically in response to migration of a crescentic bar.

6.1.3 What is the role of directional wave conditions on the formation, development and straightening of crescentic bars and megacusps?

The effect of directional wave conditions on the dynamics of crescentic bar events at the study site was analysed in detail in Chapter 4. Crescentic bars were present at Castelldefels beach during nearly half of the 8-year study period and a clear relation was observed between their dynamics and the prevailing wave conditions. Consistent with previous observations (e.g., Rutten et al., 2018), formation of crescentic bars at Castelldefels typically occurred during low-medium energetic waves (mean $H_{mo} < 0.6$ m) with angles that varied from shore-normal to limited obliquity ($\theta_{mean} \lesssim 20°$ at 10-m depth). This also comprises angles for which current morphodynamic models (Garnier et al., 2013) predict crescentic bar straightening. At the study site, crescentic bar straightening was mainly observed during higher energetic waves (mean $H_{mo} = 0.73$ m) with strong oblique angles of incidence ($\theta_{mean} \gtrsim 15°$ at 10-m depth). This threshold in wave angle is much larger than typically reported in existing model studies (e.g., Calvete et al., 2005), but consistent with recent observational studies (e.g., Contardo and Symonds, 2015). The wave conditions also influenced the alongshore migration of crescentic bars as a clear relation was observed between the alongshore crescentic bar migration rates and the radiation stress S_{xy} (the alongshore transport of cross-shore momentum). Comparing modelled and observed migration rates using S_{xy} values showed that morphodynamic models often overpredicted migration rates.

As described in detail in Chapter 5, megacusps were observed during a quarter of the study period and their dynamics were not clearly linked to the prevailing wave conditions. Low-energetic waves with a large range in wave angles were dominant during megacusp formation and megacusp presence, but also when no megacusps were present. Megacusps generally disappeared during higher energetic waves, but they also diffused during very low-energetic wave conditions. Additionally, no clear relation was observed between the alongshore migration of megacusps and the radiation stress S_{xy}. To conclude, the prevailing wave conditions strongly affect the dynamics of crescentic bars but they have less direct influence on the dynamics of megacusps.

6.1.4 How important is the shape of the cross-shore beach profile on the evolution of crescentic bars and megacusps?

The shape of the cross-shore beach profile affects the cross-shore transport, which is responsible for redistributing sediment between the surf zone and the shoreline and thus plays an

important role in the feedback between nearshore morphological patterns and the nearshore waves. As described in Chapter 4, the shape of the cross-shore profile was particularly important in the development of crescentic bars at Castelldefels. Crescentic bar events were irregularly distributed over the different years, even though the wave conditions showed no substantial differences between the various years. A closer analysis revealed that crescentic bars were only observed when the sandbar was located at least 10 m from shore. However, the sandbar should also not be located too far from shore, because the generally low-energetic waves at Castelldefels cannot induce morphological changes if the sandbar is located too deep. This also explains why the outer sandbar was inactive during most of the study period and typically only the inner sandbar was active. Furthermore, the shape of the cross-shore beach profile also affected the crescentic bar wavelengths, which generally increased with the bar-shoreline distance.

As described in Chapter 5, no direct relation was observed between megacusp evolution and the cross-shore beach profile. However, megacusps generally developed in the presence of a crescentic bar. As a result, megacusp events showed a similar irregular distribution over the study period as the crescentic bar events. Since crescentic bar development was strongly related to the shape of the cross-shore beach profile, an indirect relation between megacusp development and the cross-shore beach profile was observed. In particular, megacusps were generally not present when the inner sandbar was located less than 10 m from shore, because crescentic bars did not develop in this situation.

6.1.5 How important is the morphological coupling between crescentic bars and megacusps and what are the underlying mechanisms?

The morphological coupling at the study site between crescentic bars and megacusps was investigated in Chapter 5. A strong indication for the existence of morphological coupling was that crescentic bars were observed during 91% of all days with megacusps, whereas only 50% of all days with crescentic bars also featured megacusps. This indicates that crescentic bar presence is a strong prerequisite for megacusp development, whilst the reverse is not true. Formation of megacusps typically occurred several days after the formation of a crescentic bar and they often disappeared together with crescentic bar straightening (particularly during storms). Nevertheless, megacusps were also observed to disappear several days before or after straightening of a crescentic bar. Furthermore, megacusps mostly migrated alongshore in response to alongshore migration of a crescentic bar, which is another indication that the dynamics of megacusps are coupled to the dynamics of crescentic bars. Finally, significant morphological coupling (98% confidence level) was observed at the study site during 74% of the period with simultaneous presence of megacusps and crescentic bars. The observed coupling patterns showed a large variation in phase, which was mostly a result of differential displacement of the crescentic bar with respect to the megacusps. In phase, out of phase and downwave (shoreline embayment downdrift of crescentic bar horn) coupling occurred frequently for all wave angles, whereas upwave (shoreline embayment updrift of crescentic bar horn) coupling was only regularly observed for near shore-normal waves. A detailed analysis of existing morphodynamic modelling studies (Calvete et al., 2005; Coco et al., 2020) showed that out of phase coupling seems to be related to the presence of a double rip cell circulation during low-energetic wave conditions, whilst in phase coupling occurs due to the presence of a single rip cell circulation during higher energetic waves. Consistent with this theory, out of phase (in phase) coupling occurred at Castelldefels during lower (higher) energetic waves.

However, the relation between the bar-shoreline distance and the type of coupling pattern that was reported by a few previous observational studies (e.g., Van de Lageweg et al., 2013) was not evident at our study site. The abundance of downwave coupling is hypothesised to be related to a meandering alongshore current over the inner crescentic bar that is driven by strong oblique waves. Such a current can erode part of the shoreline downdrift of the inner crescentic bar horn and form a megacusp embayment, resulting in downwave coupling. The frequently occurring strong oblique wave angles at the study site mean that conditions are often ideal for the formation of this type of current. Furthermore, the same mechanism was linked to downdrift coupling patterns between outer and inner crescentic bars (see Price and Ruessink, 2013; Price et al., 2013). Further research using morphodynamic models is needed to confirm the physical mechanisms that result in the formation of the various coupling patterns.

6.2 Suggestions for future research

A variety of observational data is needed to validate scientific theories and the results of modelling studies regarding the evolution of crescentic bars and megacusps. Most existing observations are less suited for such comparisons as they are often limited in duration or temporal resolution, but the observations presented in this thesis do not have these drawbacks. Additionally, crescentic bars and megacusps are found globally in widely varying environmental conditions, but most existing observational studies focused on studying these patterns in medium-high energy beaches with significant tides (e.g., Van Enckevort et al., 2004). Therefore, more studies with the same level of detail in a variety of environments (including some comparable to Castelldefels) are required to generalise the findings presented in this thesis.

The results of this thesis regarding the dynamics of crescentic bars and megacusps, as well as megacusp-crescentic bar coupling were also compared to various existing morphodynamic modelling studies. Generally speaking, existing morphodynamic models underpredicted the angle for which crescentic bars develop, whilst they often overpredicted wavelengths and migration rates. Furthermore, the important result that crescentic bars were only observed when the bar-shoreline distance exceeded 10–15 m is not explained by existing modelling studies. One of the reason is that most existing modelling studies used cross-shore profiles in which the inner bar was much further from shore (> 50 m), whilst they typically also used wave conditions that were more energetic (H_{m0} > 1.0 m) compared to those generally present at the study site (H_{m0} ~0.5 m). As a result, there is a need for modelling studies that study the dynamics of crescentic bars in low-energetic environments using settings that are comparable to those encountered at Castelldefels beach. The models used should include the effect of wave rollers (foamy area of circulating water that moves onshore due to the breaking waves), as previous modelling studies showed that these were important in the dynamics of crescentic bars (e.g., Ribas et al., 2011). In particular, new modelling studies should focus on the development of crescentic bars for different cross-shore profiles, such as terraced versus barred beaches and investigate the effect of variations in bar-shoreline distance, bar trough/crest depth and bed slope. Furthermore, the development of crescentic bars for oblique angles of incidence and the relation between crescentic bar wavelengths and the bar-shoreline distance need to be clarified. Finally, modelling the alongshore migration of crescentic bars and crescentic bar straightening during low-medium energetic oblique waves deserve more attention.

Such modelling studies require detailed information on the wave conditions during crescentic bar formation/straightening (as presented in this thesis), but also frequent detailed measurements of the bathymetry to get accurate information on the shape of the cross-shore profile (e.g., presence of an inner bar or inner terrace). Unfortunately, bathymetry is usually measured sporadically due to the involved costs, meaning that such information is often not available during crescentic bar formation/straightening. It is expected that the ongoing developments to extract bathymetry from video images will be extremely helpful to tackle this problem and advance this area of research.

Most existing morphodynamic modelling studies use a fixed shoreline, which means that they are not suited to analyse the evolution of the shoreline. As a result, not many modelling studies investigated the interaction between crescentic bars and megacusps whilst there is a clear need to unravel the mechanisms driving these interactions. These future works should focus on the important role of crescentic bar presence in megacusp development and what processes are responsible for the emergence of the various coupling patterns. In particular, the type of flow pattern over the inner bar should be studied in detail (single or double rip cell circulations versus meandering alongshore currents) and how these depend on the offshore wave conditions and the bar-shoreline distance. Furthermore, the differences between alongshore migration rates of crescentic bars and megacusps and how these in turn affect the coupling patterns should also be studied.

Finally, morphodynamic models are typically forced by a single set of integrated wave parameters. However, as explained in Chapter 3, a single set of integrated wave parameters is a very coarse representation of the full 2D wave spectrum and cannot adequately describe complex sea states with multiple wave fields (like bimodal wave climates). As a result, the wave action included in morphodynamic models is often very basic and has little in common with the real world. Therefore, it would be interesting to develop morphodynamic models that can be forced using multiple sets of integrated wave parameters or the full 2D spectrum. In that way, it would be possible to study the evolution of the nearshore morphology due to irregular wave fields, bringing modelling studies one more step closer to reality.

Appendix A | Measuring directional wave parameters

In this thesis, directional spectra and related directional wave parameters like mean wave direction and directional spreading are used to quantify the evolution of nearshore morphological patterns. However, the definition of these parameters and how they are measured by instruments is not straightforward. This appendix provides some additional details regarding these topics and is complementary to Chapter 3.

A.1 Obtaining directional spectra from measurements

Directional characteristics of surface water waves are typically measured by systems that record a number of time-series, which are subsequently processed using spectral analysis techniques in order to obtain 2D frequency-direction spectra (Longuet-Higgins et al., 1963; Mitsuyasu et al., 1975; Kuik et al., 1988). The different parameters are typically measured at the same location or the same parameter is measured at multiple locations, which allows for an estimation of the spectrum and the associated wave parameters (Young, 1994). This means that the real 2D frequency-direction spectrum is not known. From the obtained spectra, various wave parameters can be computed (see Table 3.1 of Chapter 3).

Directional wave parameters are defined using the 2D frequency-direction spectrum, $E(f,\theta)$, which is often written as

$$E(f,\theta) = E(f)D(f,\theta) \quad , \tag{A.1}$$

where $D(f,\theta)$ is called the directional distribution function that has units of 1/deg. It is defined in such a way that $\int_0^{2\pi} D(f,\theta)d\theta = 1$. A lot of different methods have been developed to obtain $D(f,\theta)$ out of wave buoy measurements. The most common method starts by decomposing $D(f,\theta)$ conceptually into a Fourier series using (Longuet-Higgins et al., 1963)

$$D(f,\theta) = \frac{1}{\pi}\left\{\frac{1}{2} + \sum_{n=1}^{\infty}[a_n^* \cos(n\theta) + b_n^* \sin(n\theta)]\right\} \quad , \tag{A.2}$$

where $a_n^*(f)$ and $b_n^*(f)$ are the standard Fourier coefficient that are defined as

$$\begin{aligned} a_n^*(f) &= \int_0^{2\pi} D(f,\theta)\cos(n\theta)d\theta \quad \text{and} \\ b_n^*(f) &= \int_0^{2\pi} D(f,\theta)\sin(n\theta)d\theta \quad . \end{aligned} \tag{A.3}$$

However, the number of available time series in wave buoys (e.g., heave, pitch and roll or accelerations in x, y, z) limits the number of Fourier terms that can be inferred, so that only the first four coefficients $(a_1^*, b_1^*, a_2^*, b_2^*)$ of $D(f,\theta)$ can be obtained from wave buoy measurements (Young, 1994). This means that $D(f,\theta)$ is only resolved well if the unmeasured

higher-order coefficients are small, which is normally not the case (Rogers and Wang, 2007). Consequently, this method generally overestimates directional spreading, whereas $D(f,\theta)$ is mostly too broad and can even become negative (Young, 1994). To overcome this problem, parametric models like the $\cos^{2s}$ method (s being the spreading parameter; see Longuet-Higgins et al., 1963; Mitsuyasu et al., 1975) and data-adaptive methods like the Maximum Likelihood Method (MLM; Krogstad et al., 1988) and Maximum Entropy Method (MEM; Lygre and Krogstad, 1986) approximate the complete Fourier series to give a full estimate of $D(f,\theta)$. However, the drawback of these models is that they give details of $D(f,\theta)$ that are not determinable from buoy measurements and sometimes even generate spurious data (Benoit et al., 1997; Rogers and Wang, 2007).

A.2 Definitions of directional wave parameters

The problems described in Section A.1 regarding measuring directional wave spectra mean that directional wave parameters have to be defined carefully so that they do not depend on parametric or data-adaptive methods. Consequently, Kuik et al. (1988) defined mean wave direction, $\theta^*_{mean}(f)$, and directional spreading, $\sigma^*_\theta(f)$, per frequency, as a function of the first two determinable Fourier coefficients. Their expression for $\theta^*_{mean}(f)$ reads

$$\theta^*_{mean}(f) = \tan^{-1}\left[\frac{b_1^*(f)}{a_1^*(f)}\right] \quad . \tag{A.4}$$

However, the frequency range is always finite so the way to compute the overall mean direction averaged over the f_{low}-f_{high} frequency band is

$$\theta_{mean} = \tan^{-1}\left[\frac{b_1}{a_1}\right] \quad , \tag{A.5}$$

and the peak wave direction θ_{peak} is computed by taking the mean direction at the frequency peak ($\theta_{peak} = \theta^*_{mean}(f_p)$). Furthermore, the directional spreading averaged over the frequency range can be computed using

$$\sigma_\theta = \sqrt{2\left[1 - r_1\right]} \quad , \quad \text{where} \quad r_1 = \sqrt{a_1^2 + b_1^2} \quad , \tag{A.6}$$

in which a_1 and b_1 are the first 2 Fourier coefficients that are defined as

$$a_1 = \frac{\int_{f_{low}}^{f_{high}} a_1^*(f)E(f)df}{\int_{f_{low}}^{f_{high}} E(f)df} \quad \text{and}$$
$$b_1 = \frac{\int_{f_{low}}^{f_{high}} b_1^*(f)E(f)df}{\int_{f_{low}}^{f_{high}} E(f)df} \quad . \tag{A.7}$$

Wave buoys normally obtain the Fourier coefficients from measurements as described by Hoekstra et al. (1994).

Bibliography

Aagaard, T. (1988). Nearshore Bar Morphology on the Low-Energy Coast of Northern Zealand, Denmark. *Geografiska Annaler: Series A, Physical Geography* 70.1-2, pp. 59–67. DOI:10.1080/04353676.1988.11880239.

Aagaard, T., A. Kroon, S. Andersen, R. Møller Sørensen, S. Quartel, and N. Vinther (2005). Intertidal beach change during storm conditions; Egmond, The Netherlands. *Marine Geology* 218.1-4, pp. 65–80. DOI:10.1016/J.MARGEO.2005.04.001.

Aleman, N., N. Robin, R. Certain, E. J. Anthony, and J. P. Barusseau (2015). Longshore variability of beach states and bar types in a microtidal, storm-influenced, low-energy environment. *Geomorphology* 241, pp. 175–191. DOI:10.1016/J.GEOMORPH.2015.03.029.

Aleman, N., R. Certain, N. Robin, and J. P. Barusseau (2017). Morphodynamics of slightly oblique nearshore bars and their relationship with the cycle of net offshore migration. *Marine Geology* 392.August, pp. 41–52. DOI:10.1016/J.MARGEO.2017.08.014.

Allender, J, T Audunson, S. Barstow, S. Bjerken, H. Krogstad, P. Steinbakke, L. Vartdal, L. Borgman, and C. Graham (1989). The wadic project: A comprehensive field evaluation of directional wave instrumentation. *Ocean Engineering* 16.5-6, pp. 505–536. DOI:10.1016/0029-8018(89)90050-4.

Almar, R., B. Castelle, B. G. Ruessink, N. Sénéchal, P. Bonneton, and V. Marieu (2010). Two- and three-dimensional double-sandbar system behaviour under intense wave forcing and a meso-macro tidal range. *Continental Shelf Research* 30.7, pp. 781–792. DOI:10.1016/J.CSR.2010.02.001.

Alomar, M., A. Sánchez-Arcilla, R. Bolaños, and A. Sairouni (2014). Wave growth and forecasting in variable, semi-enclosed domains. *Continental Shelf Research* 87, pp. 28–40. DOI:10.1016/J.CSR.2014.05.008.

Amoudry, L. O. and A. J. Souza (2011). Deterministic Coastal Morphological and Sediment Transport Modeling: a Review and Discussion. *Reviews of Geophysics* 49.2, RG2002. DOI:10.1029/2010RG000341.

Amrutha, M. M., V. S. Kumar, K. G. Sandhya, T. M. Nair, and J. L. Rathod (2016). Wave hindcast studies using SWAN nested in WAVEWATCH III - Comparison with measured nearshore buoy data off Karwar, eastern Arabian Sea. *Ocean Engineering* 119, pp. 114–124. DOI:10.1016/J.OCEANENG.2016.04.032.

Ardhuin, F., L. Bertotti, J. R. Bidlot, L. Cavaleri, V. Filipetto, J. M. Lefevre, and P. Wittmann (2007). Comparison of wind and wave measurements and models in the Western Mediterranean Sea. *Ocean Engineering* 34.3-4, pp. 526–541. DOI:10.1016/J.OCEANENG.2006.02.008.

Arifin, R. R. and A. B. Kennedy (2011). The evolution of large scale crescentic bars on the northern Gulf of Mexico coast. *Marine Geology* 285.1-4, pp. 46–58. DOI:10.1016/J.MARGEO.2011.04.003.

Armaroli, C. and P. Ciavola (2011). Dynamics of a nearshore bar system in the northern Adriatic: A video-based morphological classification. *Geomorphology* 126.1-2, pp. 201–216. DOI:10.1016/J.GEOMORPH.2010.11.004.

Arriaga, J., J. Rutten, F. Ribas, A. Falqués, and G. Ruessink (2017). Modeling the long-term diffusion and feeding capability of a mega-nourishment. *Coastal Engineering* 121.November 2016, pp. 1–13. DOI:10.1016/J.COASTALENG.2016.11.011.

Arriaga, J., A. Falqués, F. Ribas, and E. Crews (2018). Formation events of shoreline sand waves on a gravel beach. *Ocean Dynamics* 68.6, pp. 735–748. DOI:10.1007/S10236-018-1157-5.

Ashton, A., A. B. Murray, and O. Arnoult (2001). Formation of coastline features by large-scale instabilities induced by high-angle waves. *Nature* 414.6861, pp. 296–300. DOI:10.1038/35104541.

Athanasiou, P., W. De Boer, J. Yoo, R. Ranasinghe, and A. Reniers (2018). Analysing decadal-scale crescentic bar dynamics using satellite imagery: A case study at Anmok beach, South Korea. *Marine Geology* 405.August, pp. 1–11. DOI:10.1016/J.MARGEO.2018.07.013.

Balouin, Y., J. Tesson, and M. Gervais (2013). Cuspate shoreline relationship with nearshore bar dynamics during storm events – field observations at Sete beach, France. *Journal of Coastal Research* 65.65, pp. 440–445. DOI:10.2112/SI65-075.1.

Battjes, J. A. (1994). Shallow water wave modelling. In: *Proceedings of the International Symposium: Waves - Physical and Numerical Modelling*. Vancouver: University of British Columbia, pp. 1–23.

Benoit, M., P. Frigaard, and H. A. Schaffer (1997). Analyzing multidirectional wave spectra: a tentative classification of available methods. *Proceedings of the 1997 IAHR conference* January 1997, pp. 131–158.

Bertotti, L., L. Cavaleri, A. Soret, and R. Tolosana-Delgado (2014). Performance of global and regional nested meteorological models. *Continental Shelf Research* 87, pp. 17–27. DOI:10.1016/J.CSR.2013.12.013.

Birrien, F., B. Castelle, D. Dailloux, V. Marieu, D. Rihouey, and T. Price (2013). Video observation of megacusp evolution along a high-energy engineered sandy beach: Anglet, SW France. *Journal of Coastal Research* 165.January, pp. 1727–1732. DOI:10.2112/SI65-292.1.

Blondeaux, P. (2001). Mechanics of Coastal Forms. *Annual Review of Fluid Mechanics* 33.1, pp. 339–370. DOI:10.1146/ANNUREV.FLUID.33.1.339.

Bolaños, R., G. Jorda, J. Cateura, J. Lopez, J. Puigdefabregas, J. Gomez, and M. Espino (2009). The XIOM: 20 years of a regional coastal observatory in the Spanish Catalan coast. *Journal of Marine Systems* 77.3, pp. 237–260. DOI:10.1016/J.JMARSYS.2007.12.018.

Bolaños-Sanchez, R., A. Sanchez-Arcilla, and J. Cateura (2007). Evaluation of two atmospheric models for wind-wave modelling in the NW Mediterranean. *Journal of Marine Systems* 65.1-4 SPEC. ISS. Pp. 336–353. DOI:10.1016/J.JMARSYS.2005.09.014.

Booij, N., R. C. Ris, and L. H. Holthuijsen (1999). A third-generation wave model for coastal regions: 1. Model description and validation. *Journal of Geophysical Research* 104.C4, pp. 7649–7666. DOI:10.1029/98JC02622.

Bouvier, C., Y. Balouin, and B. Castelle (2017). Video monitoring of sandbar-shoreline response to an offshore submerged structure at a microtidal beach. *Geomorphology* 295.January, pp. 297–305. DOI:10.1016/J.GEOMORPH.2017.07.017.

Bowen, A. J. and D. L. Inman (1971). Edge waves and crescentic bars. *Journal of Geophysical Research* 76.36, pp. 8662–8671. DOI:10.1029/JC076I036P08662.

Bowman, D. and V. Goldsmith (1983). Bar morphology of dissipative beaches: An empirical model. *Marine Geology* 51.1-2, pp. 15–33. DOI:10.1016/0025-3227(83)90086-5.

Calvete, D., N. Dodd, A. Falqués, and S. M. van Leeuwen (2005). Morphological development of rip channel systems: Normal and near-normal wave incidence. *Journal of Geophysical Research C: Oceans* 110.10, pp. 1–18. DOI:10.1029/2004JC002803.

Calvete, D., G. Coco, A. Falqués, and N. Dodd (2007). (Un)predictability in rip channel systems. *Geophysical Research Letters* 34.5, p. L05605. DOI:10.1029/2006GL028162.

Carter, R. W. G. and K. J. Kitcher (1979). The Geomorphology of Offshore Sand Bars on the North Coast of Ireland. *Proceedings of the Royal Irish Academy. Section B: Biological, Geological, and Chemical Science* 79, pp. 43–61.

Castelle, B. and B. G. Ruessink (2011). Modeling formation and subsequent nonlinear evolution of rip channels: Time-varying versus time-invariant wave forcing. *Journal of Geophysical Research* 116.F4, F04008. DOI:10.1029/2011JF001997.

Castelle, B., V. Marieu, G. Coco, P. Bonneton, N. Bruneau, and B. G. Ruessink (2012). On the impact of an offshore bathymetric anomaly on surf zone rip channels. *Journal of Geophysical Research: Earth Surface* 117.1, pp. 1–20. DOI:10.1029/2011JF002141.

Castelle, B., T. Scott, R. W. Brander, and R. J. McCarroll (2016). Rip current types, circulation and hazard. *Earth-Science Reviews* 163, pp. 1–21. DOI:10.1016/J.EARSCIREV.2016.09.008.
Castelle, B. and G. Coco (2012). The morphodynamics of rip channels on embayed beaches. *Continental Shelf Research* 43, pp. 10–23. DOI:10.1016/J.CSR.2012.04.010.
Castelle, B. and G. Coco (2013). Surf zone flushing on embayed beaches. *Geophysical Research Letters* 40.10, pp. 2206–2210. DOI:10.1002/GRL.50485.
Castelle, B., P. Bonneton, H. Dupuis, and N. Sénéchal (2007). Double bar beach dynamics on the high-energy meso-macrotidal French Aquitanian Coast: A review. *Marine Geology* 245.1-4, pp. 141–159. DOI:10.1016/J.MARGEO.2007.06.001.
Castelle, B., B. G. Ruessink, P. Bonneton, V. Marieu, N. Bruneau, and T. D. Price (2010). Coupling mechanisms in double sandbar systems. Part 1: Patterns and physical explanation. *Earth Surface Processes and Landforms* 35.4, pp. 476–486. DOI:10.1002/ESP.1929.
Castelle, B., V. Marieu, S. Bujan, K. D. Splinter, A. Robinet, N. Sénéchal, and S. Ferreira (2015). Impact of the winter 2013-2014 series of severe Western Europe storms on a double-barred sandy coast: Beach and dune erosion and megacusp embayments. *Geomorphology* 238, pp. 135–148. DOI:10.1016/J.GEOMORPH.2015.03.006.
Castelle, B., V. Marieu, and S. Bujan (2019). Alongshore-Variable Beach and Dune Changes on the Timescales from Days (Storms) to Decades Along the Rip-dominated Beaches of the Gironde Coast, SW France. *Journal of Coastal Research* 88.sp1, p. 157. DOI:10.2112/SI88-012.1.
Cavaleri, L. et al. (2018). Wave modelling in coastal and inner seas. *Progress in Oceanography* 167.March, pp. 164–233. DOI:10.1016/J.POCEAN.2018.03.010.
Certain, R. (2002). Morphodynamique d'une cote sableuse microtidale à barres: le Golfe du Lion (Languedoc-Roussillon). PhD Thesis. Universite de Perpignan, Perpignan, France, pp. 1–233.
Coco, G. and A. B. Murray (2007). Patterns in the sand: From forcing templates to self-organization. *Geomorphology* 91.3-4, pp. 271–290. DOI:10.1016/J.GEOMORPH.2007.04.023.
Coco, G., K. R. Bryan, M. O. Geen, B. G. Ruessink, I. L. Turner, and I. M. J. Van Enckevort (2005). Video Observations of Shoreline and Sandbar Coupled Dynamics. *Proceedings of Coasts and Ports*, pp. 471–476.
Coco, G., D. Calvete, F. Ribas, H. E. De Swart, and A. Falqués (2020). Emerging crescentic patterns in modelled double sandbar systems under normally incident waves. *Earth Surface Dynamics* 8.2, pp. 323–334. DOI:10.5194/ESURF-8-323-2020.
Contardo, S. and G. Symonds (2015). Sandbar straightening under wind-sea and swell forcing. *Marine Geology* 368, pp. 25–41. DOI:10.1016/J.MARGEO.2015.06.010.
Cooper, J. A. G. et al. (2020). Sandy beaches can survive sea-level rise. *Nature Climate Change* 10.11, pp. 993–995. DOI:10.1038/S41558-020-00934-2.
Dalrymple, R. A., J. H. MacMahan, A. J. H. M. Reniers, and V. Nelko (2011). Rip Currents. *Annual Review of Fluid Mechanics* 43.1, pp. 551–581. DOI:10.1146/ANNUREV-FLUID-122109-160733.
Damgaard, J., N. Dodd, L. Hall, and T. Chesher (2002). Morphodynamic modelling of rip channel growth. *Coastal Engineering* 45.3-4, pp. 199–221. DOI:10.1016/S0378-3839(02)00034-0.
De la Hoz, C. F., E. Ramos, A. Puente, F. Méndez, M. Menéndez, J. A. Juanes, and Í. J. Losada (2018). Ecological typologies of large areas. An application in the Mediterranean Sea. *Journal of Environmental Management* 205, pp. 59–72. DOI:10.1016/J.JENVMAN.2017.09.058.
Deigaard, R., N. Drønen, J. Fredsøe, J. H. Jensen, and M. P. Jørgensen (1999). A morphological stability analysis for a long straight barred coast. *Coastal Engineering* 36.3, pp. 171–195. DOI:10.1016/S0378-3839(99)00005-8.
Dodd, N., A. M. Stoker, D. Calvete, and A. Sriariyawat (2008). On beach cusp formation. *Journal of Fluid Mechanics* 597, pp. 145–169. DOI:10.1017/S002211200700972X.
Dolan, R. (1971). Coastal landforms: Crescentic and rhythmic. *Bulletin of the Geological Society of America* 82.1, pp. 177–180. DOI:10.1130/0016-7606(1971)82[177:CLCAR]2.0.CO;2.
Dong, P., Y. Chen, and S. Chen (2015). Sediment size effects on rip channel dynamics. *Coastal Engineering* 99, pp. 124–135. DOI:10.1016/J.COASTALENG.2015.03.001.

Drønen, N. and R. Deigaard (2007). Quasi-three-dimensional modelling of the morphology of longshore bars. *Coastal Engineering* 54.3, pp. 197–215. DOI:10.1016/J.COASTALENG.2006.08.011.

Dubarbier, B., B. Castelle, G. Ruessink, and V. Marieu (2017). Mechanisms controlling the complete accretionary beach state sequence. *Geophysical Research Letters* 44.11, pp. 5645–5654. DOI:10.1002/2017GL073094.

Falqués, A., A. Montoto, and V. Iranzo (1996). Bed-flow instability of the longshore current. *Continental Shelf Research* 16.15, pp. 1927–1964. DOI:10.1016/0278-4343(96)00031-3.

Falqués, A., G. Coco, and D. A. Huntley (2000). A mechanism for the generation of wave-driven rhythmic patterns in the surf zone. *Journal of Geophysical Research: Oceans* 105.C10, pp. 24071–24087. DOI:10.1029/2000JC900100.

Galal, E. M. and S. Takewaka (2008). Longshore Migration of Shoreline Mega-Cusps Observed with X-Band Radar. *Coastal Engineering Journal* 50.3, pp. 247–276. DOI:10.1142/S0578563408001818.

Gallagher, E. L., S. Elgar, and R. T. Guza (1998). Observations of sand bar evolution on a natural beach. *Journal of Geophysical Research: Oceans* 103.C2, pp. 3203–3215. DOI:10.1029/97JC02765.

Garnier, R. (2006). Nonlinear modelling of surf zone morphodynamical instabilities. PhD thesis. Universitat Politècnica de Catalunya, pp. 1–215.

Garnier, R., A. Falqués, D. Calvete, J. Thiébot, and F. Ribas (2013). A mechanism for sandbar straightening by oblique wave incidence. *Geophysical Research Letters* 40.11, pp. 2726–2730. DOI:10.1002/GRL.50464.

Garnier, R., D. Calvete, A. Falqués, and N. Dodd (2008). Modelling the formation and the long-term behavior of rip channel systems from the deformation of a longshore bar. *Journal of Geophysical Research: Oceans* 113.7, pp. 1–18. DOI:10.1029/2007JC004632.

Garrett, C. and B. Toulany (1981). Variability of the flow through the Strait of Belle Isle. *Journal of Marine Research* 39, pp. 163–189.

Gervais, M., Y. Balouin, J. Thiebot, R. Certain, R. Bélon, R. Pedreros, N. Robin, and S. Berne (2011). Morphodynamic evolution of nearshore bars in response to winter storms (Lido de Sète, NW Mediterranean). *Journal of Coastal Research* SPEC. ISSUE 64, pp. 1855–1860.

Gervais, M., Y. Balouin, and R. Belon (2012). Morphological response and coastal dynamics associated with major storm events along the Gulf of Lions Coastline, France. *Geomorphology* 143-144, pp. 69–80. DOI:10.1016/J.GEOMORPH.2011.07.035.

Gijsman, R., B. Ruessink, J. Visscher, and T. Schlurmann (2021). Observations on decadal sandbar behaviour along a large‐scale curved shoreline. *Earth Surface Processes and Landforms* 46.2, pp. 490–503. DOI:10.1002/ESP.5041.

Goldsmith, V., D. Bowman, and K. Kiley (1982). Sequential Stage Development of Crescentic Bars: Hahoterim Beach, Southeastern Mediterranean. *SEPM Journal of Sedimentary Research* Vol. 52.1, pp. 233–249. DOI:10.1306/212F7F22-2B24-11D7-8648000102C1865D.

Gómez Lahoz, M. and J. C. Carretero Albiach (2005). Wave forecasting at the Spanish coasts. *Journal of Atmospheric & Ocean Science* 10.4, pp. 389–405. DOI:10.1080/17417530601127522.

Gómez-Pujol, L., A. Orfila, B. Cañellas, A. Alvarez-Ellacuria, F. J. Méndez, R. Medina, and J. Tintoré (2007). Morphodynamic classification of sandy beaches in low energetic marine environment. *Marine Geology* 242.4, pp. 235–246. DOI:10.1016/J.MARGEO.2007.03.008.

Gorrell, L., B. Raubenheimer, S. Elgar, and R. Guza (2011). SWAN predictions of waves observed in shallow water onshore of complex bathymetry. *Coastal Engineering* 58.6, pp. 510–516. DOI:10.1016/J.COASTALENG.2011.01.013.

Guza, R. T. and D. L. Inman (1975). Edge waves and beach cusps. *Journal of Geophysical Research* 80.21, pp. 2997–3012. DOI:10.1029/JC080I021P02997.

Harley, M. D., I. L. Turner, and A. D. Short (2015). New insights into embayed beach rotation: The importance of wave exposure and cross-shore processes. *Journal of Geophysical Research F: Earth Surface* 120.8, pp. 1470–1484. DOI:10.1002/2014JF003390.

Hasselmann, K. et al. (1973). Measurements of wind-wave growth and swell decay during the Joint North Sea Wave Project (JONSWAP). *Ergänzungsheft zur Deutschen Hydrographischen Zeitschrift* 12.A8, pp. 1–95.

Hino, M. (1974). Theory on Formation of Rip-Current and Cuspidal Coast. *Coastal Engineering in Japan* 17.1, pp. 23–37. DOI:10.1080/05785634.1974.11924180.

Hoekstra, G. W., L. Boeré, A. J. M. Van der Vlugt, and T. van Rijn (1994). *Mathematical description of the Standard Wave Analysis Package*. Tech. rep. Rijkswaterstaat: Ministry of Transport, Public Works and Water Management, pp. 1–32.

Holman, R. A. and A. J. Bowen (1982). Bars, bumps, and holes: Models for the generation of complex beach topography. *Journal of Geophysical Research* 87.C1, p. 457. DOI:10.1029/JC087iC01p00457.

Holman, R. A. and J. Stanley (2007). The history and technical capabilities of Argus. *Coastal Engineering* 54.6-7, pp. 477–491. DOI:10.1016/J.COASTALENG.2007.01.003.

Holman, R. A., G. Symonds, E. B. Thornton, and R. Ranasinghe (2006). Rip spacing and persistence on an embayed beach. *Journal of Geophysical Research* 111.C1, p. C01006. DOI:10.1029/2005JC002965.

Holthuijsen, L. H. (2007). *Waves in Oceanic and Coastal Waters*. Cambridge: Cambridge University Press, pp. 1–387. DOI:10.1017/CBO9780511618536.

Kaergaard, K. and J. Fredsoe (2013). Numerical modeling of shoreline undulations part 1: Constant wave climate. *Coastal Engineering* 75, pp. 64–76. DOI:10.1016/J.COASTALENG.2012.11.006.

King, C. A. M. and W. W. Williams (1949). The Formation and Movement of Sand Bars by Wave Action. *The Geographical Journal* 113, p. 70. DOI:10.2307/1788907.

Klein, M. D. and H. M. Schuttelaars (2006). Morphodynamic evolution of double-barred beaches. *Journal of Geophysical Research* 111.C6, p. C06017. DOI:10.1029/2005JC003155.

Komen, G. J., S. Hasselmann, and K. Hasselmann (1984). On the Existence of a Fully Developed Wind-Sea Spectrum. *Journal of Physical Oceanography* 14.8, pp. 1271–1285. DOI:10.1175/1520-0485(1984)014<1271:OTEOAF>2.0.CO;2.

Komen, G. J., L. Cavaleri, M. Donelan, K. Hasselmann, S. Hasselmann, and P. A. E. M. Janssen (1994). *Dynamics and Modelling of Ocean Waves*. Cambridge: Cambridge University Press, pp. 1–554. DOI:10.1017/CBO9780511628955.

Krogstad, H. E., R. L. Gordon, and M. C. Miller (1988). High-Resolution Directional Wave Spectra from Horizontally Mounted Acoustic Doppler Current Meters. *Journal of Atmospheric and Oceanic Technology* 5.2, pp. 340–352. DOI:10.1175/1520-0426(1988)005<0340:HRDWSF>2.0.CO;2.

Kuik, A. J., G. P. Van Vledder, and L. H. Holthuijsen (1988). A Method for the Routine Analysis of Pitch-and-Roll Buoy Wave Data. *Journal of Physical Oceanography* 18.7, pp. 1020–1034. DOI:10.1175/1520-0485(1988)018<1020:AMFTRA>2.0.CO;2.

Lippmann, T. C. and R. A. Holman (1989). Quantification of sand bar morphology: a video technique based on wave dissipation. *Journal of Geophysical Research* 94.C1, pp. 995–1011. DOI:10.1029/JC094iC01p00995.

Lippmann, T. C. and R. A. Holman (1990). The spatial and temporal variability of sand bar morphology. *Journal of Geophysical Research* 95.C7, p. 11575. DOI:10.1029/JC095iC07p11575.

Longuet-Higgins, M. S. (1970). Longshore currents generated by obliquely incident sea waves: 1. *Journal of Geophysical Research* 75.33, pp. 6778–6789. DOI:10.1029/JC075i033p06778.

Longuet-Higgins, M. S. and R. W. Stewart (1962). Radiation stress and mass transport in gravity waves, with application to 'surf beats'. *Journal of Fluid Mechanics* 13.4, pp. 481–504. DOI:10.1017/S0022112062000877.

Longuet-Higgins, M. S. and R. W. Stewart (1964). Radiation stresses in water waves; a physical discussion, with applications. *Deep Sea Research and Oceanographic Abstracts* 11.4, pp. 529–562. DOI:10.1016/0011-7471(64)90001-4.

Longuet-Higgins, M. S., D. E. Cartwright, and N. D. Smith (1963). Observations of the directional spectrum of sea waves using the motions of a floating buoy. In: *Ocean Wave Spectra*. New York: Prentice-Hall, pp. 111–136.

Luijendijk, A., G. Hagenaars, R. Ranasinghe, F. Baart, G. Donchyts, and S. Aarninkhof (2018). The State of the World's Beaches. *Scientific Reports* 8.1, p. 6641. DOI:10.1038/s41598-018-24630-6.

Lygre, A. and H. E. Krogstad (1986). Maximum Entropy Estimation of the Directional Distribution in Ocean Wave Spectra. *Journal of Physical Oceanography* 16.12, pp. 2052–2060. DOI:10.1175/1520-0485(1986)016<2052:MEEOTD>2.0.CO;2.

MacMahan, J. (2001). Hydrographic Surveying from Personal Watercraft. *Journal of Surveying Engineering* 127.1, pp. 12–24. DOI:10.1061/(ASCE)0733-9453(2001)127:1(12).

MacMahan, J. et al. (2010). Mean Lagrangian flow behavior on an open coast rip-channeled beach: A new perspective. *Marine Geology* 268.1-4, pp. 1–15. DOI:10.1016/J.MARGEO.2009.09.011.

Melito, L., L. Parlagreco, E. Perugini, M. Postacchini, S. Devoti, L. Soldini, G. Zitti, L. Liberti, and M. Brocchini (2020). Sandbar dynamics in microtidal environments: Migration patterns in unprotected and bounded beaches. *Coastal Engineering* 161.October, p. 103768. DOI:10.1016/J.COASTALENG.2020.103768.

Mentaschi, L., G. Besio, F. Cassola, and A. Mazzino (2015). Performance evaluation of Wavewatch III in the Mediterranean Sea. *Ocean Modelling* 90, pp. 82–94. DOI:10.1016/J.OCEMOD.2015.04.003.

Michallet, H., B. Castelle, E. Barthélemy, C. Berni, and P. Bonneton (2013). Physical modeling of three-dimensional intermediate beach morphodynamics. *Journal of Geophysical Research: Earth Surface* 118.2, pp. 1045–1059. DOI:10.1002/JGRF.20078.

Miles, M. D., E. Mansard, T. Vandall, and R. Phillips (2003). TRIAXYS Directional Wave Buoy. *Canadian Coastal Conference*, pp. 1–15.

Mitsuyasu, H., F. Tasai, T. Suhara, S. Mizuno, M. Ohkusu, T. Honda, and K. Rikiishi (1975). Observations of the Directional Spectrum of Ocean Waves Using a Cloverleaf Buoy. *Journal of Physical Oceanography* 5.4, pp. 750–760. DOI:10.1175/1520-0485(1975)005<0750:OOTDSO>2.0.CO;2.

Nafaa, M. G. and O. E. Frihy (1993). Beach and nearshore features along the dissipative coastline of the Nile Delta, Egypt. *Journal of Coastal Research* 9.2, pp. 423–433.

Nicholls, R. J. and A. Cazenave (2010). Sea-Level Rise and Its Impact on Coastal Zones. *Science* 328.5985, pp. 1517–1520. DOI:10.1126/SCIENCE.1185782.

Nieto, M. A. et al. (2010). An open source, low cost video-based coastal monitoring system. *Earth Surface Processes and Landforms* 35.14, pp. 1712–1719. DOI:10.1002/ESP.2025.

Nnafie, A., A. S. Driessen, H. E. De Swart, and T. D. Price (2021). Modelling the response of a double-barred sandy beach system to time-varying wave angles. *Earth Surface Processes and Landforms*, esp.5107. DOI:10.1002/ESP.5107.

Nnafie, A., N. Van Andel, and H. E. De Swart (2020). Modelling the impact of a time-varying wave angle on the nonlinear evolution of sand bars in the surf zone. *Earth Surface Processes and Landforms* 45.11, pp. 2603–2612. DOI:10.1002/ESP.4916.

Ojeda, E. and J. Guillén (2008). Shoreline dynamics and beach rotation of artificial embayed beaches. *Marine Geology* 253.1-2, pp. 51–62. DOI:10.1016/J.MARGEO.2008.03.010.

Ojeda, E., J. Guillén, and F. Ribas (2011). Dynamics of single-barred embayed beaches. *Marine Geology* 280.1-4, pp. 76–90. DOI:10.1016/J.MARGEO.2010.12.002.

Oppenheimer, M. et al. (2019). Sea Level Rise and Implications for Low-Lying Islands, Coasts and Communities. In: *IPCC Special Report on the Ocean and Cryosphere in a Changing Climate*, pp. 321–445.

O'Reilly, W. C., T. H. C. Herbers, R. J. Seymour, and R. T. Guza (1996). A Comparison of Directional Buoy and Fixed Platform Measurements Of Pacific Swell. *Journal of Atmospheric and Oceanic Technology* 13.1, pp. 231–238. DOI:10.1175/1520-0426(1996)013<0231:ACODBA>2.0.CO;2.

Orzech, M. D., E. B. Thornton, J. H. MacMahan, W. C. O'Reilly, and T. P. Stanton (2010). Alongshore rip channel migration and sediment transport. *Marine Geology* 271.3-4, pp. 278–291. DOI:10.1016/J.MARGEO.2010.02.022.

Orzech, M. D., A. J. H. M. Reniers, E. B. Thornton, and J. H. MacMahan (2011). Megacusps on rip channel bathymetry: Observations and modeling. *Coastal Engineering* 58.9, pp. 890–907. DOI:10.1016/J.COASTALENG.2011.05.001.

Pallares, E., A. Sánchez-Arcilla, and M. Espino (2014). Wave energy balance in wave models (SWAN) for semi-enclosed domains-Application to the Catalan coast. *Continental Shelf Research* 87, pp. 41–53. DOI:10.1016/J.CSR.2014.03.008.

Pape, L. (2008). *BLIM Toolbox Manual*. Tech. rep. November. IMAU Report R08-02, p. 43.

Parlagreco, L., L. Melito, S. Devoti, E. Perugini, L. Soldini, G. Zitti, and M. Brocchini (2019). Monitoring for Coastal Resilience: Preliminary Data from Five Italian Sandy Beaches. *Sensors* 19.8, p. 1854. DOI:10.3390/S19081854.

Perez, J., M. Menendez, and I. J. Losada (2017). GOW2: A global wave hindcast for coastal applications. *Coastal Engineering* 124.January, pp. 1–11. DOI:10.1016/J.COASTALENG.2017.03.005.

Pettersson, H., H. C. Graber, D. Hauser, C. Quentin, K. K. Kahma, W. M. Drennan, and M. A. Donelan (2003). Directional wave measurements from three wave sensors during the FETCH experiment. *Journal of Geophysical Research* 108.C3, p. 8061. DOI:10.1029/2001JC001164.

Pierson, W. J. and L. Moskowitz (1964). A proposed spectral form for fully developed wind seas based on the similarity theory of S. A. Kitaigorodskii. *Journal of Geophysical Research* 69.24, pp. 5181–5190. DOI:10.1029/JZ069I024P05181.

Portilla-Yandún, J., L. Cavaleri, and G. P. Van Vledder (2015). Wave spectra partitioning and long term statistical distribution. *Ocean Modelling* 96, pp. 148–160. DOI:10.1016/J.OCEMOD.2015.06.008.

Price, T. D. and B. G. Ruessink (2011). State dynamics of a double sandbar system. *Continental Shelf Research* 31.6, pp. 659–674. DOI:10.1016/J.CSR.2010.12.018.

Price, T. D., B. Castelle, R. Ranasinghe, and B. G. Ruessink (2013). Coupled sandbar patterns and obliquely incident waves. *Journal of Geophysical Research: Earth Surface* 118.3, pp. 1677–1692. DOI:10.1002/JGRF.20103.

Price, T. D. and B. G. Ruessink (2013). Observations and conceptual modelling of morphological coupling in a double sandbar system. *Earth Surface Processes and Landforms* 38.5, pp. 477–489. DOI:10.1002/ESP.3293.

Puertos del Estado (1994). *Maritime Works Recommendations. ROM 0.3-91 Waves Annex 1: Wave Climate on the Spanish coast.* Tech. rep. Ministerio de Obras Publicas y Transporte, Centro de Publicaciones de Secretaría General Técnica, pp. 1–70.

Puertos del Estado (2015a). *Conjunto de datos: REDMAR*. Tech. rep. Madrid: Ministerio de Fomento, pp. 1–9.

Puertos del Estado (2015b). *Conjunto de datos SIMAR*. Tech. rep. Madrid: Ministerio de Fomento, pp. 1–5.

Quartel, S. (2009). Temporal and spatial behaviour of rip channels in a multiple-barred coastal system. *Earth Surface Processes and Landforms* 34.2, pp. 163–176. DOI:10.1002/ESP.1685.

Ranasinghe, R., G. Symonds, K. Black, and R. Holman (2004). Morphodynamics of intermediate beaches: a video imaging and numerical modelling study. *Coastal Engineering* 51.7, pp. 629–655. DOI:10.1016/J.COASTALENG.2004.07.018.

Reniers, A. J. H. M., J. A. Roelvink, and E. B. Thornton (2004). Morphodynamic modeling of an embayed beach under wave group forcing. *Journal of Geophysical Research* 109.C1, p. C01030. DOI:10.1029/2002JC001586.

Ribas, F. and A. Kroon (2007). Characteristics and dynamics of surfzone transverse finger bars. *Journal of Geophysical Research: Earth Surface* 112.3, pp. 1–13. DOI:10.1029/2006JF000685.

Ribas, F., H. E. De Swart, D. Calvete, and A. Falquès (2011). Modeling waves, currents and sandbars on natural beaches: The effect of surface rollers. *Journal of Marine Systems* 88.1, pp. 90–101. DOI:10.1016/J.JMARSYS.2011.02.016.

Ribas, F., H. E. De Swart, D. Calvete, and A. Falqués (2012). Modeling and analyzing observed transverse sand bars in the surf zone. *Journal of Geophysical Research: Earth Surface* 117.2, pp. 1–16. DOI:10.1029/2011JF002158.

Ribas, F., A. Falqués, H. E. De Swart, N. Dodd, R. Garnier, and D. Calvete (2015). Understanding coastal morphodynamic patterns from depth-averaged sediment concentration. *Reviews of Geophysics* 53.2, pp. 362–410. DOI:10.1002/2014RG000457.

Ribas, F., E. Ojeda, T. D. Price, and J. Guillén (2010). Assessing the Suitability of Video Imaging for Studying the Dynamics of Nearshore Sandbars in Tideless Beaches. *IEEE Transactions on Geoscience and Remote Sensing* 48.6, pp. 2482–2497. DOI:10.1109/TGRS.2009.2039576.

Ribas, F., A. Falqués, and R. Garnier (2017). Nearshore Sand Bars on Western Mediterranean Beaches. In: *Atlas of Bedforms in the Western Mediterranean*. Cham: Springer International Publishing, pp. 81–88. DOI:10.1007/978-3-319-33940-5_14.

Ribas, F., G. Simarro, J. Arriaga, and P. Luque (2020). Automatic Shoreline Detection from Video Images by Combining Information from Different Methods. *Remote Sensing* 12.22, p. 3717. DOI:10.3390/RS12223717.

Ris, R. C., L. H. Holthuijsen, and N. Booij (1999). A third-generation wave model for coastal regions: Verification. *Journal of Geophysical Research* 104, pp. 7667–7681. DOI:10.1029/1998JC900123.

Rodriguez-Delgado, C., R. J. Bergillos, M. Ortega-Sánchez, and G. Iglesias (2018). Wave farm effects on the coast: The alongshore position. *Science of the Total Environment* 640-641, pp. 1176–1186. DOI:10.1016/J.SCITOTENV.2018.05.281.

Rogers, W. E. and D. W. Wang (2007). Directional validation of wave predictions. *Journal of Atmospheric and Oceanic Technology* 24.3, pp. 504–520. DOI:10.1175/JTECH1990.1.

Ruessink, B. G. and A. Kroon (1994). The behaviour of a multiple bar system in the nearshore zone of Terschelling, the Netherlands: 1965–1993. *Marine Geology* 121.3-4, pp. 187–197. DOI:10.1016/0025-3227(94)90030-2.

Ruessink, B. G., I. M. J. Van Enckevort, K. S. Kingston, and M. A. Davidson (2000). Analysis of observed two- and three-dimensional nearshore bar behaviour. *Marine Geology* 169.1-2, pp. 161–183. DOI:10.1016/S0025-3227(00)00060-8.

Ruessink, B. G., G. Coco, R. Ranasinghe, and I. L. Turner (2007). Coupled and noncoupled behavior of three-dimensional morphological patterns in a double sandbar system. *Journal of Geophysical Research: Oceans* 112.7, pp. 1–11. DOI:10.1029/2006JC003799.

Ruessink, B. G., L. Pape, and I. L. Turner (2009). Daily to interannual cross-shore sandbar migration: Observations from a multiple sandbar system. *Continental Shelf Research* 29.14, pp. 1663–1677. DOI:10.1016/J.CSR.2009.05.011.

Rutten, J., B. G. Ruessink, and T. D. Price (2018). Observations on sandbar behaviour along a man-made curved coast. *Earth Surface Processes and Landforms* 43.1, pp. 134–149. DOI:10.1002/ESP.4158.

Rutten, J., B. Dubarbier, T. D. Price, B. G. Ruessink, and B. Castelle (2019). Alongshore Variability in Crescentic Sandbar Patterns at a Strongly Curved Coast. *Journal of Geophysical Research: Earth Surface* 100 m, 2019JF005041. DOI:10.1029/2019JF005041.

Saha, S. et al. (2010). The NCEP Climate Forecast System Reanalysis. *Bulletin of the American Meteorological Society* 91.8, pp. 1015–1058. DOI:10.1175/2010BAMS3001.1.

Saha, S. et al. (2014). The NCEP Climate Forecast System Version 2. *Journal of Climate* 27.6, pp. 2185–2208. DOI:10.1175/JCLI-D-12-00823.1.

Sánchez-Arcilla, A., D. González-Marco, and R. Bolaños (2008). A review of wave climate and prediction along the Spanish Mediterranean coast. *Natural Hazards and Earth System Science* 8.6, pp. 1217–1228. DOI:10.5194/NHESS-8-1217-2008.

Scott, T., G. Masselink, M. J. Austin, and P. Russell (2014). Controls on macrotidal rip current circulation and hazard. *Geomorphology* 214, pp. 198–215. DOI:10.1016/J.GEOMORPH.2014.02.005.

Segura, L. E., J. E. Hansen, R. J. Lowe, G. Symonds, and S. Contardo (2018). Shoreline variability at a low-energy beach: Contributions of storms, megacusps and sea-breeze cycles. *Marine Geology* 400.March, pp. 94–106. DOI:10.1016/J.MARGEO.2018.03.008.

Shand, R. D., D. G. Bailey, and M. J. Shepherd (1999). An inter-site comparison of net offshore bar migration characteristics and environmental conditions. *Journal of Coastal Research* 15.3, pp. 750–765.

Short, A. D. (1979). Three Dimensional Beach-Stage Model. *The Journal of Geology* 87.5, pp. 553–571. DOI:10.1086/628445.

Short, A. D. and T. Aagaard (1993). Single and multi-bar beach change models. *Journal of Coastal Research* 1993.SPEC. ISSUE 15, pp. 141–157.

Simarro, G., K. R. Bryan, R. M. C. Guedes, A. Sancho, J. Guillen, and G. Coco (2015). On the use of variance images for runup and shoreline detection. *Coastal Engineering* 99, pp. 136–147. DOI:10.1016/J.COASTALENG.2015.03.002.

Simarro, G., F. Ribas, A. Álvarez, J. Guillén, Ò. Chic, and A. Orfila (2017). ULISES: An Open Source Code for Extrinsic Calibrations and Planview Generations in Coastal Video Monitoring Systems. *Journal of Coastal Research* 335, pp. 1217–1227. DOI:10.2112/JCOASTRES-D-16-00022.1.

Smit, M. W. J., A. J. H. M. Reniers, B. G. Ruessink, and J. A. Roelvink (2008). The morphological response of a nearshore double sandbar system to constant wave forcing. *Coastal Engineering* 55.10, pp. 761–770. DOI:10.1016/J.COASTALENG.2008.02.010.

Smit, M. W. J., A. J. H. M. Reniers, and M. J. F. Stive (2012). Role of morphological variability in the evolution of nearshore sandbars. *Coastal Engineering* 69, pp. 19–28. DOI:10.1016/J.COASTALENG.2012.05.005.

Sonu, C. J. (1972). Field observation of nearshore circulation and meandering currents. *Journal of Geophysical Research* 77.18, pp. 3232–3247. DOI:10.1029/JC077I018P03232.

Sonu, C. J. (1973). Three-Dimensional Beach Changes. *The Journal of Geology* 81.1, pp. 42–64. DOI:10.1086/627806.

Soomere, T. and M. Viška (2014). Simulated wave-driven sediment transport along the eastern coast of the Baltic Sea. *Journal of Marine Systems* 129, pp. 96–105. DOI:10.1016/J.JMARSYS.2013.02.001.

Soulsby, R. (1998). *Dynamics of Marine Sands*. London: Thomas Telford Ltd, pp. 1–249. DOI:10.1680/DOMS.25844.

Splinter, K. D., R. A. Holman, and N. G. Plant (2011). A behavior-oriented dynamic model for sandbar migration and 2DH evolution. *Journal of Geophysical Research: Oceans* 116.1, pp. 1–21. DOI:10.1029/2010JC006382.

SWAN Team (2018a). *SWAN Scientific and Technical Documentation. SWAN Cycle III version 41.20A*. Tech. rep. Delft, The Netherlands: Delft University of Technology, pp. 1–147.

SWAN Team (2018b). *SWAN User Manual. SWAN Cycle III version 41.20A*. Tech. rep. Delft, The Netherlands: Delft University of Technology, pp. 1–141.

The WADMI Group (1988). The WAM Model - A Third Generation Ocean Wave Prediction Model. *Journal of Physical Oceanography* 18.12, pp. 1775–1810. DOI:10.1175/1520-0485(1988)018<1775:TWMTGO>2.0.CO;2.

Thiébot, J., D. Idier, R. Garnier, A. Falqués, and B. G. Ruessink (2012). The influence of wave direction on the morphological response of a double sandbar system. *Continental Shelf Research* 32, pp. 71–85. DOI:10.1016/J.CSR.2011.10.014.

Thornton, E. B., J. MacMahan, and A. H. Sallenger (2007). Rip currents, mega-cusps, and eroding dunes. *Marine Geology* 240.1-4, pp. 151–167. DOI:10.1016/J.MARGEO.2007.02.018.

Tiessen, M. C. H., S. M. Van Leeuwen, D. Calvete, and N. Dodd (2010). A field test of a linear stability model for crescentic bars. *Coastal Engineering* 57.1, pp. 41–51. DOI:10.1016/J.COASTALENG.2009.09.002.

Tiessen, M. C. H., N. Dodd, and R. Garnier (2011). Development of crescentic bars for a periodically perturbed initial bathymetry. *Journal of Geophysical Research: Earth Surface* 116.4, pp. 1–24. DOI:10.1029/2011JF002069.

Tolman, H. L. (2009). *User manual and system documentation of WAVEWATCH III version 3.14*. Tech. rep. NOAA/NWS/NCEP/MMAB, p. 194.

Undén, P. et al. (2002). *High Resolution Limited Area Model, HIRLAM-5 Scientific Documentation*. Tech. rep. Swedish Meteorological and Hydrological Institute, Norrköping, Sweden, pp. 1–144.

Van de Lageweg, W. I., K. R. Bryan, G. Coco, and B. G. Ruessink (2013). Observations of shoreline-sandbar coupling on an embayed beach. *Marine Geology* 344, pp. 101–114. DOI:10.1016/J.MARGEO.2013.07.018.

Van den Berg, N., A. Falqués, and F. Ribas (2012). Modeling large scale shoreline sand waves under oblique wave incidence. *Journal of Geophysical Research: Earth Surface* 117.F3, n/a–n/a. DOI:10.1029/2011JF002177.

Van Enckevort, I. M. J. and B. G. Ruessink (2001). Effect of hydrodynamics and bathymetry on video estimates of nearshore sandbar position. *Journal of Geophysical Research: Oceans* 106.C8, pp. 16969–16979. DOI:10.1029/1999JC000167.

Van Enckevort, I. M. J., B. G. Ruessink, G. Coco, K Suzuki, I. L. Turner, N. G. Plant, and R. A. Holman (2004). Observations of nearshore crescentic sandbars. *Journal of Geophysical Research* 109.C6, p. C06028. DOI:10.1029/2003JC002214.

Vitousek, S., P. L. Barnard, and P. Limber (2017). Can beaches survive climate change? *Journal of Geophysical Research: Earth Surface* 122.4, pp. 1060–1067. DOI:10.1002/2017JF004308.

Vousdoukas, M. I., R. Ranasinghe, L. Mentaschi, T. A. Plomaritis, P. Athanasiou, A. Luijendijk, and L. Feyen (2020). Sandy coastlines under threat of erosion. *Nature Climate Change* 10.3, pp. 260–263. DOI:10.1038/s41558-020-0697-0.

Whitham, G. B. (1974). *Linear and Nonlinear Waves*. Hoboken, NJ, USA: John Wiley & Sons, Inc., pp. 1–638. DOI:10.1002/9781118032954.

Wright, L. D. and A. D. Short (1984). Morphodynamic variability of surf zones and beaches: A synthesis. *Marine Geology* 56.1-4, pp. 93–118. DOI:10.1016/0025-3227(84)90008-2.

Young, I. R. (1994). On the measurement of directional wave spectra. *Applied Ocean Research* 16.5, pp. 283–294. DOI:10.1016/0141-1187(94)90017-5.

About the author

Rinse de Swart was born on the 24th of September 1992 in the city of Utrecht, the Netherlands and grew up in the village of Bunnik. Already at a very young age, he was fascinated by rivers and coasts which made him determined to study the processes that shape these environments. After attending the Christelijk Lyceum in Zeist between 2004 and 2010, he started studying Earth Sciences at Utrecht University with a focus on Physical Geography. After studying the cyclic behaviour of sandy shoals on the Wadden Island of Vlieland for his bachelor thesis, he continued studying at Utrecht University by enrolling in the master's programme Earth Surface and Water with as specialisation coastal morphodynamics and fluvial systems. For his master's thesis, he studied salinity intrusion and tidal propagation in estuarine channel networks with varying channel lengths using the Delft3D model. His interest in doing research was further triggered during his 6-months internship at the Coastal Morphodynamics group of the Universitat Politècnica de Catalunya (UPC), where he did a preliminary study on crescentic bar dynamics at Castelldefels beach. After obtaining the master's degree at the end of 2015, he started working at a consultancy company, but he returned to the Coastal Morphodynamics group of the UPC in 2017 to pursue a PhD. The results of his PhD research are presented in this thesis.

List of publications

Journal papers

De Swart, R.L., F. Ribas, D. Calvete, G. Simarro, and J. Guillén (under review). Observations of megacusp dynamics and their coupling with crescentic bars at an open, fetch-limited beach. Submitted to *Earth Surface Processes and Landforms*.

De Swart, R.L., F. Ribas, G. Simarro, J. Guillén, and D. Calvete (2021). The role of bathymetry and directional wave conditions on observed crescentic bar dynamics. *Earth Surface Processes and Landforms* 46.15, pp. 3252–3270. https://doi.org/10.1002/esp.5233.

De Swart, R.L., F. Ribas, D. Calvete, A. Kroon, and A. Orfila (2020). Optimal estimations of directional wave conditions for nearshore field studies. *Continental Shelf Research* 196.104071. https://doi.org/10.1016/j.csr.2020.104071.

Conference proceeding

De Swart, R.L., F. Ribas, G. Ruessink, G. Simarro, and J. Guillén (2017). Characteristics and dynamics of crescentic bar events in an open, tideless beach. *Proceedings of the Coastal Dynamics 2017* 192, pp. 555–566.

Conference abstracts

De Swart, R.L., F. Ribas, G. Simarro, J. Guillén, and D. Calvete (2021). Observed alongshore sandbar and shoreline variability at an open, fetch-limited beach.
IAHR Symposium on River, Coastal and Estuarine Morphodynamics 2021, online (online poster)

De Swart, R.L., F. Ribas, D. Calvete, G. Simarro, and J. Guillén (2021). Alongshore sandbar and shoreline rhythmicity at an open, Mediterranean beach.
International Conference on Coastal Dynamics 2021, Delft, The Netherlands (online presentation)

De Swart, R.L., F. Ribas, D. Calvete, G. Simarro, and J. Guillén (2020). Characteristics and dynamics of crescentic bar events at an open, Mediterranean beach.
EGU General Assembly 2020, online (online presentation)

De Swart, R.L., F. Ribas, G. Simarro, and J. Guillén (2019). Characteristics and dynamics of crescentic bar events at Castelldefels beach.
X Jornadas de Geomorfología Litoral, Castelldefels, Spain (poster presentation)

De Swart, R.L., F. Ribas, D. Calvete, A. Orfila, and A. Kroon (2019). Obtaining directional wave characteristics in front of nearshore field sites.
EGU General Assembly 2019, Vienna, Austria (oral presentation)

De Swart, R.L., F. Ribas, and D. Calvete (2017). The role of oblique wave incidence on crescentic bar dynamics.
IAHR Symposium on River, Coastal and Estuarine Morphodynamics 2017, Padova, Italy (poster presentation)

De Swart, R.L., F. Ribas, G. Ruessink, G. Simarro, and J. Guillén (2017). Crescentic bar dynamics at an open, Mediterranean beach.
International Conference on Coastal dynamics 2017, Helsingør, Denmark (oral presentation)

Acknowledgements

Doing a PhD is a solitary activity, especially in a foreign country in the midst of a global pandemic. Fortunately, there were a lot of people that helped and supported me during my PhD research. In this chapter, I would like to thank those who contributed either directly or indirectly to the realisation of this thesis.

First and foremost, I want to thank my supervisors Francesca Ribas and Daniel Calvete. Cesca, thank you for your guidance, for always being enthusiastic and optimistic, for your confidence in me, for keeping in mind the overall progress of me as a PhD student and for the many useful comments and suggestions on all my manuscripts. Daniel, thank you for the many discussions we had, for always looking at my results from a different (modelling) perspective, your stubbornness (no no no, espera espera) and your humour. Cesca and Daniel, thank you both for giving me the freedom to wander off into the field of nearshore wave modelling and for helping me to write my first paper about the results I obtained during this scientific detour, even though it was also a new field for both of you. Thank you also for inviting me to your home several times and treating me not just as a PhD student but as a colleague and friend. Ferran and Clara, I enjoyed getting to know you. Esther, Victor and Nil, it was always a pleasure to see you and listen to your stories.

Of course I can not forget about the other Morfos, Albert Falqués, Jaime Arriaga, Nabil Kakeh and Nil Carrion. Albert, as head of the group you were not directly involved in my research but you were always interested in my findings and your door was at all times open for having a good scientific discussion. I also wish to thank you and Isabel for inviting me several times to your home in the countryside. Isabel, siempre fue un placer verte, disfrutar de tu deliciosa cocina y practicar mi castellano contigo. Jaime and Nabil, thank you sharing the office with me during the first years of my PhD and the many discussions we had about each others results. Nil, it was very nice to see how quickly you have become a Morfo. I hope you will be able to continue your work of the past year and do a PhD with the Morfos in the near future. Thanks also to Toni, without whom I would still be fighting Linux instead of doing research and the rest of the group of fluids, Paco, Isabel, Alvaro, Oriol, Arantxa, Roger and Baoying for the necessary social interactions. I also want to thank the members of the PhD committee - Albert Falqués, Àngels Fernández Mora, Bruno Castelle, Ruth Duran and Giovanni Coco.

I could not have written this thesis without the data from the video station at Castelldefels beach, which is jointly maintained by the Coastal Morphodynamics Group (UPC) and the Institute of Marine Sciences (ICM-CSIC). I wish to thank the technical support from both institutions, in particular Oscar Chic (ICM-CSIC) and Toni Castillo (UPC). Furthermore, I thank the city council of Castelldefels for permitting the installation of the video cameras. The field campaign that formed the basis of Chapter 3 would not have been possible without Benjamín Casas of IMEDEA and the various technicians of SOCIB. Thank you for all your help and assistance. Additionally, this thesis also used a lot of data from external sources. I

want to thank Pilar Gil from Puertos del Estado for providing the SIMAR, tide and wave buoy data, IH Cantabria for providing the GOW2 data and the Spanish meteorological agency (Agencia Estatal de Meteorología) for providing the wind data of Barcelona airport.

As part of my PhD, I also extensively collaborated with various scientists from other institutions. Gonzalo, thank you very much for all your work on developing all kinds of software for extracting data from the video system, your assistance in using your codes and the general interest in my research. The comments you provided on the manuscripts of Chapters 4 and 5 were very helpful. Jorge, I greatly appreciate all your efforts that led to the installation of a video monitoring system at Castelldefels beach which made this research possible and that you were also part of the subsequent study of the evolution of Castelldefels beach. You always looked at my results from the perspective of a coastal geomorphologist and as such provided valuable comments and suggestions on the manuscripts of Chapters 4 and 5. Alejandro, thank you for your leading role in the field campaign and providing constructive feedback on various manuscripts of the resulting Chapter 3. Timothy, thank you the various discussions we had regarding morphological coupling, for sharing your Matlab codes and your general curiosity regarding my research. Aart, when I first met you many years ago you quickly infected me with your passion regarding the coastal system and this was fuelled more with every subsequent encounter. Your enthusiasm was one of the main reasons why I started studying Physical Geography, which ultimately resulted in me doing a PhD on coastal morphodynamics. Of course, I was really happy that the opportunity arose to collaborate with you during my PhD. Apart from your very valuable participation in the field campaign, you also provided lots of helpful comments and suggestions on numerous manuscripts of Chapter 3. Thank you for sharing your passion, your interest in my research and the fruitful collaboration.

Outside the scientific community, there were also many people who supported me during my PhD research. First of all my study friends from Oh Oh Geo - Florian, Fionna, Koos, Lars, Laura and Alexander, Peter, Renske, Willem - thank you for not forgetting about me, for coming over all the way to Barcelona (there are worse places to visit), for all the trips, dinners, game evenings, online and offline pub quizzes, and for providing the necessary laugh and distraction during my PhD. Laura, it was really nice that we were doing our PhD simultaneously and could support each other where necessary. Peter, you always made sure I was not out of touch for too long. It was always nice to talk with each other about anything, even though we were often separated by 1200 km. Machteld, thank you for your interest and for changing your busy agenda so that we could meet almost every time I was visiting the Netherlands. Amir, I really enjoyed getting to know you during the past few months and showing you Barcelona and its surroundings. Kimberley, Luitze, Marijke, Roelant and the other people at WaterProof B.V. - thank you for your interest in my work, the numerous online coffee meetings during the pandemic that made me feel part of the company again and for facilitating the various visits to the office in Lelystad that were always very enjoyable.

Last but not least, I want to thank my parents for always supporting me in my choices, for believing in me, for the numerous visits to Barcelona before the pandemic and for the many hours we spent on the telephone and Skype with which we managed to make the distance between Barcelona and Bunnik a little bit shorter.

Barcelona, May 2022